Swansea University
Prifysgol Abertawe

Advanced Clean Water Treatment at Tata Port Talbot: Silica removal in Water

Sedar Dogan

Swansea University

Submitted to Swansea University in fulfilment of the requirements for the

Degree of Engineering Doctorate

2024

Declarations

This work has not previously been accepted in substance for any degree and is not being concurrently submitted in candidature for any degree.

Signed

Date   23/12/2024

This thesis is the result of my own investigations, except where otherwise stated. Other sources are acknowledged by footnotes giving explicit references.   A bibliography is appended.

Signed

Date   23/12/2024

I hereby give consent for my thesis, if accepted, to be available for electronic sharing

Signed

Date   23/12/2024

The University's ethical procedures have been followed and, where appropriate, that ethical approval has been granted.

Signed

Date   23/12/2024

Acknowledgments

Abstract

With rising industry standards, the presence of silica in both colloidal and soluble forms presents significant operational challenges in boiler feedwater systems. Silica contributes to scaling, fouling, and corrosion within boilers and turbines, impacting safety, efficiency, and longevity. Effective silica removal is crucial to meet stringent water quality standards and protect equipment. This thesis examines the water treatment challenges at Tata Steel Port Talbot, specifically addressing silica-related issues, and evaluates advanced treatment technologies to enhance silica removal.

The existing water treatment system at Tata Steel Port Talbot involves surface water intake followed by chemical coagulation, clarification, filtration, and ion exchange. However, despite these measures, conventional methods often fail to adequately control colloidal silica levels. This research seeks to bridge this gap by exploring innovative approaches to silica management, with a focus on reducing silica in boiler feedwater.

One area of focus was the assessment of coagulants, comparing traditional coagulants like alum and ferric chloride with novel options, such as titanium and zirconium. Each coagulant's performance was measured in terms of zeta potential, floc size, and colloidal silica removal efficiency. Results demonstrated that titanium-based coagulants, in particular, formed larger flocs and achieved similar silica removal efficiency (over 72% at 0.93 mg Ti/L) as alum, which was most effective when tested with surface water samples.

The thesis also investigates membrane technologies by enhancing polyvinylidene fluoride (PVDF) membranes with multi-walled carbon nanotubes (CNTs) and graphene oxide (GO) fabricated through phase inversion. Hybrid membranes demonstrated significant improvements in both water permeability and flux recovery. Specifically, pure water permeability increased by 141% for GO and 174% for CNT, while flux recovery enhanced by 36% for GO and 42% for CNT, compared to unmodified membranes.

Further, an ion exchange resin impregnated with iron nanoparticles was tested for soluble silica removal. Batch and column experiments revealed moderate silica removal efficacy, though selectivity decreased in the presence of competing ions like phosphate. However, iron-impregnated resins demonstrated higher phosphate selectivity due to complexation with iron particles, which could be advantageous in multi-component systems.

Lastly, ozonation was explored for its impact on destabilizing and altering the surface chemistry of colloidal silica. Ozonation at 70 g/m³ for 30 minutes decreased zeta potential, enhancing subsequent coagulation and membrane filtration stages. A multi-stage treatment approach, combining ozonation and hybrid membrane technology, was found to be optimal for achieving required silica limits, with high silica removal, improved flux recovery, and increased fouling resistance. This hybrid approach offers a balanced and effective solution for silica management, meeting industry standards, and improving system longevity.

Table of Contents

List of Figures

List of Tables

1. Introduction

1.1. Background

The integrated steel industry is an important industrial sector and is considered a fundamental force that drives the nation's economic and technological progress. Tata steel Port Talbot is one of Tata steels main sites of producing steel, which covers an area of 100 km of roads. The site is an integrated steel plant where all the processes from providing raw materials to rolling of the steel are all done at one place. The site includes coke ovens, sinter plant, and blast furnaces. Water supply is an essential part for the integrated steel plant, as water is used for a variety of processes such as dust scrubbing, descaling, and cooling. It is estimated that the average water intake for an integrated steel plant is $28.6 m^3$ per tonne of steel produced (WorldsteelAssociation, 2020).

Given the nature of an integrated steel plant, they require large quantities of power to provide electricity and with the recent shift to electric arc furnace operation from blast furnace, demand for electricity will be even more important. Typically, integrated steel plants provide a portion of their power requirements through their own generating equipment, by utilizing by-product in the steelmaking process as fuel (Lenard, 2014). A crucial part of electricity production is the requirement for high purity water to feed the boiler. The prime purpose of high purity boiler feed water is to protect the boiler. Hence, treatment of the feed water is a crucial step in the process. The boiler feed water is typically made up from an intake of raw or mains water, which replaces water for the loss due to steam consumption/evaporation, and a condensate recycle system, which is a return of the condensate to the feed water purification system (Sparks & Chase, 2016).

The feed water treatment plant must remove residual suspended solids and as much as possible of the dissolved solids. This is to prevent boiler water carryover into the steam, prevention of deposits and/or scaling in the boiler and to prevent corrosion (Moran, 2018). Boiler carryover refers to the contamination of the steam by droplets of water from the boiler and is influenced by the

concentration of dissolved solids and suspended solids, boiler design, and boiler operation. Carryovers can cause deposits of contaminants on equipment such as steam turbines casing an imbalance and reducing efficiency and capacity (Haribhakti et al., 2018a; Shreir, 1994). Deposits, scaling, and corrosion in boilers can lead to a loss in efficiency of the boiler, as scales are poor conductors of heat which reduces the heat transfer across the walls of the boiler tubes. This can eventually lead to failure of the tubes due to overheating (Haribhakti et al., 2018b).

Quality standards and concentration limits for many parameters of the water have been recommended by various agencies, such as the American Society of Mechanical Engineers (ASME) and BSI (British Standards Institution). Limits are also set by the boiler and turbine manufacturers. Table 1 shows the recommended water characteristics for a fired water tube boiler given by the British Standard institution BS 2486:1997.

Table 1.1. Recommended water quality for boilers

Pressure at boiler outlet (bar)		0 to 20	21 to 40	41 to 60	61 to 80	81 to 100	101 to 120	Above 121
Feed water at economizer inlet								
Total Hardness, mg/kg as $CaCO_3$ max		2	1	ND	ND	ND	ND	ND
pH value at 25°C		8.5 to 9.5	8.5 to 9.5	8.5 to 9.5	8.5 to 9.5	8.5 to 9.5	8.5 to 9.5	8.5 to 9.5
Oxygen, mg/kg as O_2 max		0.02	0.02	0.01	0.005	0.005	0.005	0.005
Iron, copper, and nickel, mg/kg max		0.05	0.05	0.03	0.02	0.02	0.02	0.02
Boiler Water								
Phosphate, mg/kg PO_4^{3-}		30 to 70	20 to 50	20 to 40	15 to 30	10 to 20	3 to 10	3 to 5
Caustic alkalinity mg/kg $CaCO_3$		50 to 300	50 to 150	25 to50	10 to 20	5 to 10	2 to 5	1 to 5
Silica as mg/kg SiO_2		<0.4 times caustic alkalinity	<0.4 times caustic alkalinity	20 max.	5 max.	2 max.	1.5 max.	0.5 max.
Dissolved solids mg/kg max.		3000	2500	1000	200	50	20	10
Conductivity at 25°C, µS/cm		6000	5000	2000	450	150	60	35

However, levels of solids in feed water are dependent on the level of blowdown required to sustain the stated water conditions. Modern steam turbines have strict limits on alkali metals (e.g., sodium) typically less than 0.005 mg/L Na. One other important note is that the silica limits are based on the prevention of silicate scale deposits and limitation of silica solubility in steam, however, modern day steam turbines require silica to be much lower, <0.02 mg/L as SiO_2 based on steam silica content. As such, water quality is a major cause of boiler problems and failures and in order to protect the boiler, it is imperative to treat boiler feed water.

1.2. Aims and Objectives

The aim of this EngD thesis is to develop an in-depth understanding of the water quality issues at Tata Steel Port Talbot and evaluate new treatment technologies to address them. This was done by prioritising the water quality challenges to address, evaluating the type and sources of contaminants, evaluating the options for minimising the contamination and evaluating potential treatment technologies. These aims were addressed through the following objectives:

1. Determining the type and concentration of silica as major contaminant and challenge in the water treatment plant

2. Optimising coagulant dosage and introducing novel coagulants of titanium and zirconium in determining the effectiveness of removing silica

3. Introduction of GO and CNTs to improve membrane performance and determining its suitability for silica separation

4. Testing anion exchange resin impregnated with iron nanoparticles efficacy in silica removal

5. Exploiting the use of hybrid technologies to conclude which configuration is most effective at silica removal.

2. Water treatment of an integrated steel plant - A review

2.1. Current water treatment plant at Tata Steel Port Talbot (Margam C)

The boilers at Tata Steel Port Talbot operate at 126 bar necessitating the need for exceptionally clean water. To achieve this surface water sourced from the river Afan, goes through multiple stages of treatment. The key stages include chemical coagulation, clarification, sand filtration and multiple stages of ion exchange. Figure 2.1 below shows a block flow diagram of the process used at Tata.

Raw Water Tank → Clarifier → Sand Filters → Cation Exchanger → CO_2 Degasser →
Anion Exchanger → Mixed Bed → Deionised Water Tank → Polishing Mixed Bed → Polished Water Tank
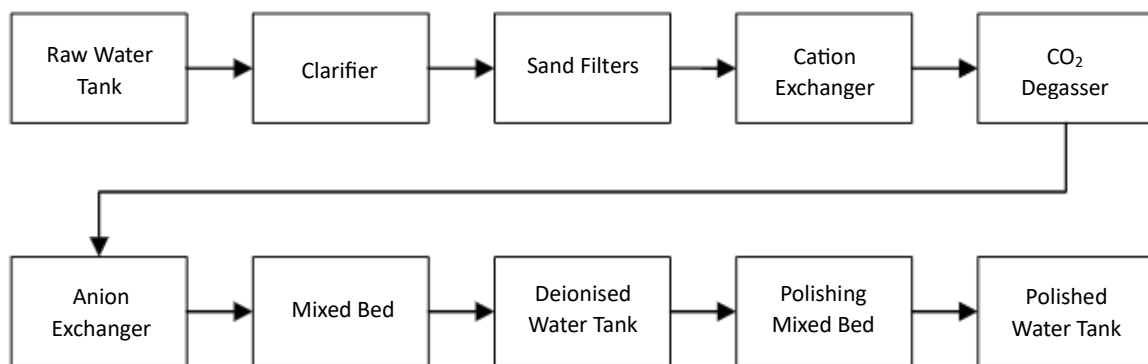
Figure 2.1. Tata Steel Port Talbot boiler feed water block flow diagram

Initially the raw water is collected from the Afan river and its tributary Nant Ffrwdwyllt, which is then sent to Margam C demineralisation plant. The plant is a manually operated plant designed to treat surface water to an acceptable standard for use as boiler feed water. The process starts off with the incoming water being dosed with a proportional dose of alum before being directed to a clarifier. The dosing is dependent on the variation of the raw water and operating conditions. The destabilised particles become settled at the bottom of the tank, which is periodically drawn off as sludge.

The clarified water is pumped from the clarified tank through sand filters to remove a portion of the remaining solids before the water is fed to the deionisation stage. It is important to highlight that these two stages are the only stages which are designed predominantly to remove particles and colloidal material in the plant.

The deionisation stage is compiled of a series of cation, anion and mixed bed systems. The cation exchange system forms the first stage of the de-ionisation plant (which removes Ca^{2+}. Mg^{2+}, Na^+ and other positively charged species), which contains polystyrene based resin in the hydrogen form. The resin is regenerated using sulfuric acid. The exhaustion of the resin is determined by a conductivity cell in the unit outlet.

Following this, the water is passed through a CO_2 degasser. The degasser must be placed after the cation unit as the water which contains bicarbonates and carbonates is converted to carbonic acid, or carbon dioxide. Using the degasser the soluble CO_2 is removed, thus, reducing the load on the anion exchanger (Dardel, 2022). The equations below represent the conversion of carbonates to carbon dioxide after passing through cation exchanger.

$$2R - H + Ca^{2+}(HCO_3^-)_2 \rightarrow 2R - Ca + 2H^+ + 2HCO3^-$$

$$H^+ + HCO_3^- \rightarrow CO_2 + H_2O$$
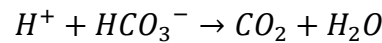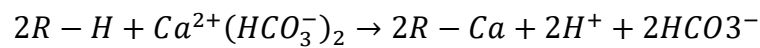
Anion exchanger is the next stage of the process, which uses a bed of polystyrene resin with quaternary amine groups in the hydroxide form. The bed is regenerated using sodium hydroxide. The exhaustion of the resin is determined by a conductivity cell in the unit outlet. The final stage of the treatment is the passage through a mixed bed unit, which consists of both cation and anion exchange resins. To regenerate the resin, a reverse flow technique is used to separate the cation and anion resins on the basis of their different densities.

After treatment in the mixed bed unit, the water is stored in a deionised water tank. Water is then drawn from the tank, prior to being sent to a polishing mixed bed unit which is mixed with the returned condensate. Water from the polisher is then sent to a polished water tank for ultimate boiler feedwater.

2.2. Water characteristics and challenges faced by Tata steel Port Talbot

The water characteristics of the river Afan can vary depending on season, Table 2.1 shows the water characteristics of River Afan from data measured in October 2022.

Table 2.1. Rive Afan water characteristics

Parameter	Result
pH	6-8
Chloride (as Cl⁻ ppm)	23.3
Hardness, Calcium (as $CaCO_3$)	33.6
Total suspended solids, TSS (ppm)	6.3
Conductivity (µS/cm)	148
Hardness, Total (as $CaCO_3$)	49.5
Iron, Total (ppm)	0.275
Silica (as SiO_2) (ppm)	2.78

With the evermore stringent limits on boilers and turbines, Tata steel Port Talbot's current water treatment plant is not meeting the requirements needed, which in turn is reducing the efficiency and increasing the potential of silica deposition in the system. One of the significant concerns with the water treatment plant is the level of colloidal silica. Independent contractors have determined that silica levels were as high as 1820 ppb, in the boiler drum, which from Table 1.1 shows it exceeds the limit for boilers operating at <121 bar (500 ppb of silica).

Silica which is found present in boiler systems can lead to the formation of silicate scale, it has been known as early as the 1940s (Behrman, A. S., & Gustafson, H., 1940) It can also interact with calcium and magnesium salts, forming calcium and magnesium silicate that have very low thermal conductivity.

Silica remaining in the system can be carried over by droplets of water in steam or in a volatile form with steam at higher pressures, and deposit on the turbine blades (Bahadori & Vuthaluru, 2010). Silica scale is dense and hard to remove by general methods, and influences the thermal efficiency and safe run of the system. Therefore, it is essential to reduce the concentration of silica within the system (Den & Wang, 2008).

2.3. Chemistry of silica

In natural surface waters, the concentration of silica can range from 0-10 ppm, and in some rare cases can be as high as 60 ppm. Silica in seawater can vary from 20 to 4000 ppb, this is due to various solubilities of silica in water. The solubility of silica is dependent on several factors including the concentration, pH, temperature other geochemical characters of natural waters (seasonal features etc). Silica may occur in natural waters in one of the following species:

- 'Soluble' or 'dissolved' silica, including monomers, dimers, and polymers of silicic acid
- 'Insoluble' or 'colloidal' silica which is a result from the polymerization of silicic acid forming particles and three-dimensional gel networks
- 'Reactive' silica containing monomers and dimers that react with ammonium molybdite within 10 minutes

2.3.1. Soluble silica
Dissolved silica is introduced to the environment by chemical and biochemical weathering processes which involve ion substitution, formation of a variety of silica species and chelate forming reactions that remove mineral lattice cations (Lunevich, 2019). The major factors that influence the solubility of amorphous silica is pH, temperature, and ionic strength (Fleming & Crerar, 1982; Greenberg & Sinclair, 1955). Silica that is dissolved in water, is fully hydrated and typically present as Ortho silicic acid H_4SiO_4 (or $Si(OH)_4$). Its tetrahedral shape predicts a very weak acidity and gives an explanation as to why silica solubility increases at a higher pH. The ionization constant of silicic acid ($K_1 = 2 \times 10^{-10}$, pKa=9.70) is considerably smaller compared to other weak acids such as carbonic acid (K_1

=4.3×10⁻⁷, pKa=6.37), meaning it does not dissociate very well (Inc., 2014). Other researchers have suggested that it is difficult to precisely define the term 'aqueous silica' as there is a range of silica species that could possibly form upon dissolution of silica (SiO_2) in water (Iler, 1979; Weres et al., 1981).

The dissolution of silica is pH dependent. The rate of dissolution is slow at pH of 1-3, which increases at higher pH (3-9). At pH greater than 10 silica is present as silicate ions and at pH above 11 silicate ions becomes divalent (Fleming & Crerar, 1982; Greenberg & Sinclair, 1955). Figure 2.2, shows the speciation curve for silica. Normally the water chemistry of boilers, is maintained at neutral or alkaline pH (Amjad & Koutsoukos, 2010). Temperature is also another important factor that determines the solubility of silica, in which solubility increases with temperature (Krauskopf, 1956). Other factors that influence the solubility of amorphous silica include ionic strength, particle size and impurities in the water such iron and aluminium (Lunevich, 2019).
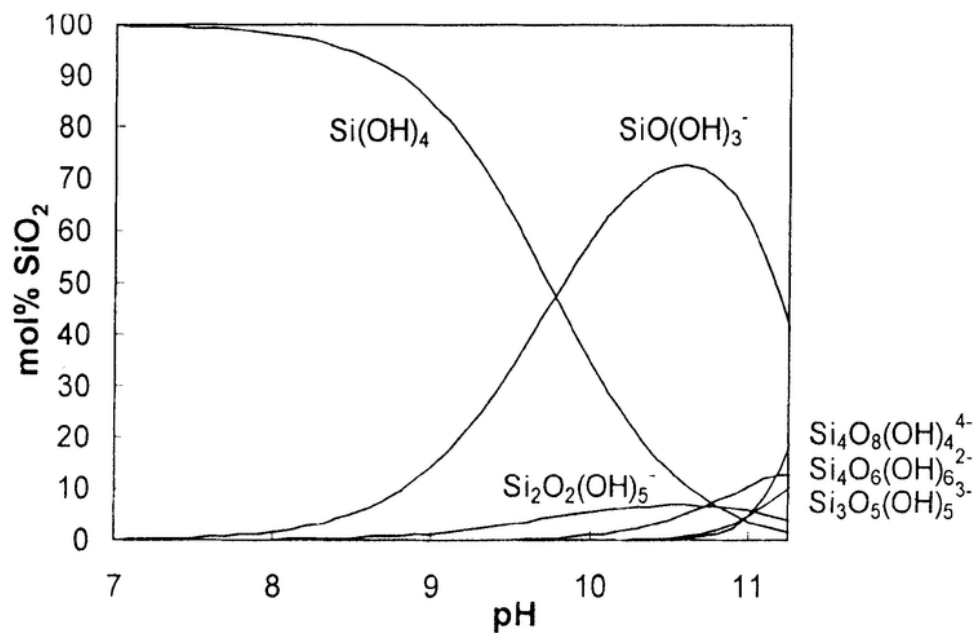
Figure 2.2. Silica speciation curve (*Dietzel, M. (2000)*)

2.3.2. Silica polymerisation

Mono silicic acid remains in the monomeric state for long periods of time in water at 25°C, provided that the concentration remains less than 100 ppm as SiO_2 (Iler, 1979). At concentrations higher than this, the monomeric silicic acid rapidly polymerizes to form low molecular weight poly silicic acids. It is widely accepted that the polymerization of silica monomers is the mechanism for the formation of amorphous silica scale (Weres et al., 1981). The polymerization of silica is a simple structural growth process, that is considered a condensation reaction, which involves the silanol groups. When the silicate ions polymerise, they form rings of various sizes, cross linked polymeric chains of different molecular weights, and oligomeric structures (Bergna, 1994; Iler, 1979; Lunevich, 2019). The growth process of silica leads to the formation of 'colloidal silica' which is a complex and amorphous product. However, the term "polymerization" is used in a broad sense.

Past studies on silica structural evolution show that structural control of silica polymerisation processes is complex, as many variables affect concurrent reactions differently. However, pH is probably the single most important variable in these reactions. Iler and Bergna has offered models for polymerisation, which applies particle nucleation and growth (Bergna, 1994; Iler, 1979). From past studies it has been found that the other factors influencing silica polymerization include temperature, saturation, impurities present in solutions and the autocatalytic effect of existing precipitated silica. Studies by Iler found that the polymerization of silicic acid occurs most rapidly at pH 8-9. Above pH 7, where the rate of dissolution and deposition of silica is high, particle growth continues at room temperature until the particles are 5-10 nm in diameter, which after, the growth becomes slow.

Polymerization rate decreases at high pH due to the solution mainly consisting of silicic acid ions, which tend to repel each other. At pH 7-10.5, due to the negatively charged silica particles, particle growth continues without aggregation, in which gelling does not occur (Makrides et al., 1980; Weres et al., 1981). At low pH silica particles bear very little ionic charge, thus can aggregate

into chains and gel networks. High temperatures and high concentrations increase the rate of silicic acid polymerization. Studies have shown that polymerization of dissolved silica species is accelerated in the presence of divalent cations, notably calcium and magnesium, but also metals such as iron and aluminium (Hingston & Raupach, 1967; Lunevich, 2019; Yokoyama et al., 1980).

The chemistry of dissolved silica in surface water is complex due to the biological activities that come into play. For example, Diatoms (species of algae) use silica to create a protective shell made of silicon dioxide crystals. Once the algal cells decompose, silica is released as dissolved silica again, creating a complex ecological balance. Biological interaction with dissolved silica will also create colloidal silica that is intrinsic to most surface waters (Belton et al.). One such study looked at the effect of natural organic matter on the aggregation of colloidal silica particles and found that depending on the type of natural organic matter and ions present, the aggregation rate of colloidal silica was enhanced (Abe et al., 2011). As such the aggregation of colloidal silica is a holistic in nature and depends on many factors.

2.3.3. Colloidal Silica

The term 'colloidal silica' refers to stable dispersions or sols of discrete particles of amorphous silica, that have particle sizes in the range of 5-1500 nm and especially in the 5-100 nm range (Bergna, 1994). Colloidal silica is the result of the polymerization of silicic acid containing particles and three-dimensional gel networks. Silica sols with particles in the range of 5-100 nm may remain for prolonged periods of time without significant loss of colloidal stability (do not aggregate at a significant rate) or settling. Silica sols lose their stability by aggregation of the colloidal particles. Iler distinguished four ways in which colloidal silica particles aggregate or link together, as follows (Iler, 1979):

1.   Gelling – particles are linked in branched chains, filling the volume of sol so that there is no increase in the concentration of silica in any macroscopic region in the medium. Instead, the overall medium becomes

viscous and then is solidified by coherent network of particles that, by capillary action, retains the liquid.

2.   Coagulation – particles come together into relatively close-packed clumps in which the silica is more concentrated than in the original sol, so the coagulum settles as a relatively dense precipitate.

3.   Flocculation – particles are linked together by bridges of the flocculating agent that are sufficiently long so that the aggregated structure remains open and voluminous.

4.   Coacervation – silica particles are surrounded by an adsorbed layer of material that makes the particles less hydrophilic but does not form bridges between particles. The particles aggregate as a concentrated liquid phase immiscible with the aqueous phase.

The size of the colloidal particle also has an effect on the aggregation. Kobayashi et al. found that particles which were above 80 nm exhibited similar features to the DLVO theory, whereas smaller particles did not adhere to the same rules (Kobayashi et al., 2005). The DLVO theory (named after Derjaguin, Landau, Verwey, and Overbeek) explains the stability of colloidal particles by balancing two opposing forces: attractive van der Waals forces and repulsive electrostatic forces. Studies which looked at the effect of pH on colloidal silica stability have shown that silica sols are extremely stable at low pH (Allen & Matijevic′, 1970).

Many of the adsorption, adhesion and chemical properties of colloidal silica depend on the chemistry and geometry of their surface. Silanol groups are formed on the surface of silica during the synthesis of condensation-polymerisation process. The silanol groups may be classified according to their nature, multiplicity of sites and type of association. The OH^- groups are the main centres of adsorption to water (Bergna, 1994). Impurities such as Na, K or Al can be taken in aqua sols in alkaline medium, which may be sealed inside the colloidal particle, replacing the silanol proton (e.g., sodium) or forming an isomorphic tetrahedra with an extra negative valence (e.g., aluminium).

2.4. Treatment technologies used in boiler feed water treatment

2.4.1. Overview

As mentioned previously, the major concerns in boiler water treatment is the prevention of water carryover into the steam, prevention of the build up of deposits and/or scale in the boiler and prevention of corrosion in the boiler. These issues are mitigated by modifying the water chemistry by removing contaminants in the water to a high degree. This can be achieved by several techniques that are used in water treatment industries. Treatment methods include, but are not limited to, demineralisation, filtration, ionization, softening and clarification (Daniel, 2009; Shokri & Sanavi Fard, 2023; Smethurst, 1979). This section will dive deeper into some of the water treatment technologies and their working principles.

2.4.2. Coagulation/flocculation

2.4.2.1. General

One of the most common methods used in the removal of particulate matter in surface water is by coagulation and flocculation, because they are efficient, easily controlled, relatively cheap and well understood. In the UK roughly more than 320,000 tonnes of coagulant is used per annum across water and wastewater treatment, with alum and ferric based salts making up a majority (Keeley et al., 2014).

Coagulation and flocculation, even though used interchangeably most of the time, are different and refer to two distinct processes. No absolute definition will be given, due to the complex nature and the wide range of use and understanding, particularly in the water treatment industry. However, for the purpose of this thesis the basis for terminology used is:

Coagulation is defined as the addition of a chemical coagulant to solution in which the colloidal particles and suspended solids go through a destabilization process (Beckett, 1991).

Flocculation is defined as the agglomeration of the destabilized particles into large aggregates (Bratby, 2016). The aggregated floc can then be removed by sedimentation and/or filtration.

2.4.2.2.Mechanism

Hydrolysing metal salts such as alum or ferric chloride and/or organic polymers are widely used in the water treatment industry. Coagulation by the addition of a metal salt can involve a combination of the following mechanisms:

- Adsorption/reaction of the negatively charged particles with the positively charged coagulant metal, also known as charge neutralisation
- Adsorption and intraparticle bridging
- Sweep flocculation with the formation of large flocs that randomly move through the water, known as Brownian motion, enmeshing the particulates

When the metal salts are dissolved in water, the metal ion is hydrolysed to form mono and polymeric species. In general, the hydrolysis reaction of a trivalent metal, such as Fe^{3+} or Al^{3+} can be represented in simplified version as follows:

$$xM^{3+} + yH_2O \leftrightarrow M_x(OH)y^{(3x-y)+} + yH^+$$
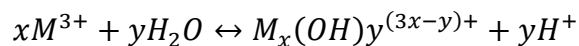
Where M is the metal ion (Ching et al., 1994). The created metal hydroxide polymers have large surface areas, amorphous structures and a positive charge (Randtke, 1988). The negatively charged particles (nearly all colloidal impurities in water are negatively charged) contain functional groups such as hydroxyl or carboxyl, can react with the aluminium or iron cations to form ligands. This adsorption of positively charged destabilizing chemical to the colloid is known as charge neutralisation (Duan & Gregory, 2003). Studies by Dentel et al detailed a model which described the charge neutralisation aspects of aluminium salt as a coagulant, which suggested the charge neutralisation was a fundamental part in particle destabilisation (Dentel & Gossett, 1988). This is further backed up by studies by Zhang et al, which studied the aggregation of hematite particles in the presence of polyacrylic acid, found that charge neutralisation mechanism was crucial, and was more crucial than polymer bridging as aggregation occurred in zones with low surface charge (Zhang & Buffle, 1995). Charge neutralisation can

then induce sweep flocculation, adsorption and bridging of organic and inorganic particles.

As mentioned earlier during hydrolysis of metal coagulants, reactions can have the tendency to polymerise. Adsorption of these polymeric species on a particle surface occur due to either coulombic charging interactions, dipole interactions, hydrogen bonding or van der Waals forces of attraction. The part of the polymer chain not attached to the particle, can then extend and attach itself to another particle, thus creating a "bridge". The bridging mechanism of destabilisation has been an accepted phenomenon for some time (Healy & Mer, 1962; Ruehrwein & Ward, 1952). Many studies have demonstrated that addition of high molecular polymers to already destabilised particles can help increase the bridging effect and create larger flocs, even at low dosages (<2 mg/L) (Hogg et al., 1993; Rattanakawin & Hogg, 2001).

Sweep flocculation occurs when colloidal particles are "enmeshed" in a gradually growing precipitate and is effectively swept out the water. This is caused when large doses of coagulants are added, in excess of the amount needed for charge neutralisation. Excess dose is required for precipitation of the hydrous metal oxide, which are then swept through the water, enmeshing the particles (Packham, 1965).

2.4.2.3. Coagulation performance parameters

The performance of the chemical coagulation process is dependent on number of key parameters including:

- Coagulant choice
- pH
- Coagulant dosage
- Mixing time

The choice of the chemical coagulant can have a great impact on its performance, and its choice will be dependent on the water type and contaminants present. Studies have demonstrated that ferric based coagulants on average had better removal of dissolved organic matter (DOC) compared to

alum based coagulants (Gough et al., 2014; Matilainen et al., 2005; Umar et al., 2016). However, for silica removal studies have demonstrated that aluminium based coagulants out performed their ferric based counter parts, this could be due to the inhibition of hydrolysis and hydroxide precipitation caused by low levels of dissolved silica (Schenk & Weber Jr, 1968). Other studies by Ghafari et al had compared conventional aluminium sulphate to pre-hydrolysed coagulants (coagulants containing a significant proportion of polymeric species) such as poly-aluminium chloride (PAC). Results from the study determined that PAC outperformed alum on all physical parameters including turbidity, colour and total suspended solids (TSS). However, alum was able to remove 5 times as much of the chemical oxygen demand (COD) compared to PAC (Ghafari et al., 2010). Other researchers such as Chuang et al showed that poly-aluminium chloride (PACl) showed higher performances of colloidal silica removal than alum (Chuang et al., 2007). Due to the growing concerns relying on chemical coagulants, which have some environmental and health concerns, there is a growing interest in the use of natural coagulants such as Moringa Oleifra seeds or Opuntia Ficus Indica cactus for the water and waste water treatment industry (Choy et al., 2014; Lester-Card et al., 2023). However, this outside the scope of this literature review.

Optimising the pH is a key parameter in the performance of a coagulant. The pH has a major effect on the speciation of the coagulant and on colloidal particles. Many minerals found in waters, have surfaces which contain functional groups (e.g. hydroxyl), and the charge of this group is dependent on the pH of the solution. Using silica as an example, which contains hydroxyl groups on its surface, can be shown how the charge differs with pH as follows:

$$Si - OH_2^{2+} \quad \leftrightarrow \quad Si - OH + H^+ \quad \leftrightarrow \quad Si - O^- + 2H^+$$

pH<<2   pH = 2   pH>>2
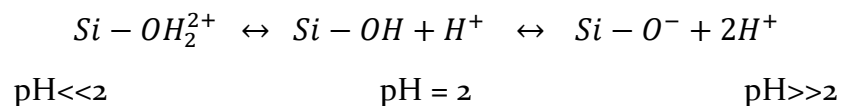
This shows that at low or acidic pHs the surface charge of silica is positive and at higher a pH the surface charge is negative. The pH at which the surface charge

is zero, is known as the point of zero charge (PZC) (J. C. Crittenden, Trussell, R.R., Hand, D.W., Howe, K.J. and Tchobanoglous, G. (2012)). There is also an effect on the coagulant when pH is adjusted. In relation to iron and aluminium, the pH value has influence on the hydrolysis and polymerisation. In low pHs (<2.2 for ferric coagulants and <4.5 for aluminium) iron and aluminium occur as hexa-aqua complexes $[Fe(H_2O)_6]^{3+}$ and $[Al(H_2O)_6]^{3+}$. Thus the effect that pH has on the charge of the molecules has a major impact on the charge neutralisation and adsorption mechanisms during coagulation (Naceradska et al., 2019). Studies by Gregory et al showed that aluminium coagulants functions within a narrow pH range in the removal of natural organic matter, and found that the optimum pH was in the acidic region of 5-6 (Gregor et al., 1997). Studies by Naceradska et al demonstrated that the optimal pH ranges required for the coagulation process are very much dependent on the specific impurities and their mixtures (Naceradska et al., 2019). For example, for natural organic matter such as humic acids, they found that acidic pH values were favourable. However, for inorganic particles, neutral pH was preferable.

The dose of a coagulant is another vital parameter in the coagulation process. The optimal dosage is the least amount of coagulant required to achieve the required water quality. The optimal dosage depends on a variety of factors including water quality, alkalinity, temperature, ionic strength etc (Maier et al., 2004; Ratnaweera & Fettig, 2015). Studies by Mao et al showed that increasing dosages of poly ferric chloride (PFC) significantly improved DOC removal, as they found that the increased dosage produced stronger and more compact flocs. However, overdosing would lead to the flocs losing its structure (Mao et al., 2013).

2.4.2.4. *Jar tests*

Jar tests are lab scale tests which simulate the coagulation/flocculation process and is widely used when wanting to test the application of a coagulant (Black et al., 1957). The typical configuration consists of a motor driven horizontal spindle driving up to six vertical paddles, with variable speed motor. Jar tests allow for easy control and variation of mixing speeds.

The general approach to jar testing typically starts off with a high intensity mixing stage that allows for the coagulant to rapidly disperse in the medium. This is then followed by a low intensity mixing, to allow the aggregation of the particles, followed finally by a settling stage with no mixing (Black & Vilaret, 1969).

Jar tests allow the user to perform a number of different tasks including, selection of a suitable coagulant, optimisation of dose and pH, optimisation of the mixing stage and more. Overall, jar testing can produce information quickly and economically, which the data gained directly applicable to plant design (Hudson Jr & Wagner, 1981).

2.4.3. Membranes
2.4.3.1. General
Membrane technology is a well established water treatment technology, with the first meaningful use implemented in 1960s to test for drinking water, with a total annual sales of roughly $20 million dollars (marked up to match with inflation in 2012) (Singh, 2015). The majority of the global membrane market share is for water and wastewater treatment (45.8%) with the rest being made up of food and beverage, gas separation and others. Membranes popularity stems to its advantages such as no addition of chemicals, simple operation, low energy consumption and modular design which is easy to scale up (Kang & Cao, 2014).

Membranes are a physiochemical separation technique that uses the differences in permeability as a separation mechanism. The membrane is typically a synthetic material which is semipermeable (J. C. Crittenden, Trussell, R.R., Hand, D.W., Howe, K.J. and Tchobanoglous, G., 2012). At present membranes within industrial use is made from inorganic and/or organic polymers, with the latter dominating. Examples of organic polymers include polysulfone (PSF), poly (ether sulfone) (PES) and poly(vinylidene fluoride) (PVDF).

Characteristically membranes can be split into two groups, isotropic and anisotropic. Isotropic membranes are uniform in composition and physical

structure. Currently isotropic membranes are widely applied in microfiltration membranes. Anisotropic membranes on the other hand, are non-uniform membranes made up of different layers with differing structures (Obotey Ezugbe & Rathilal, 2020).

2.4.3.2. Membrane classifications

Pressure driven membranes can be classified into four main types, which are, microfiltration (MF), ultrafiltration (UF), nano filtration (NF) and reverse osmosis (RO). The primary differences are the operating pressures, pore sizes and molecular weight cut off (MWCO).

MF is the first classification of membrane separation, it was developed in 1960s for applications in the pharmaceutical and biological industries. From that point forward, MFs have been widely used in the water and wastewater sectors. The MF separation mechanism is primarily through a sieving or size exclusion technique, although some charge or adsorptive separation is possible. The size range for MF membranes is in the range of 0.1 – 10 μm, and typically used to remove impurities such as particles, viruses and bacteria. The pressure applied on MF membranes is quite low when compared to the other membranes, with an operating pressure of < 2 bar (Baker, 2004).

Ultrafiltration membranes were developed as a by-product of cellulose acetate RO membranes, and was introduced commercially by Millipore and Amicon in the 1960s. UF membranes due to their porous structure (pore size 1 – 100 nm) admits micro solutes through the membrane. Due to this feature, UF membranes are used to remove macromolecules, colloids and molecules with a molecular weight greater than 10,000, these species can produce an osmotic pressure, which means UF requires higher pressures to overcome the difference. The operating pressure in UF membranes is larger than MF and ranges from 1 – 10 bar (Strathmann, 1981). Selectivity of separation for UF is based on the size difference and also surface charge of the membrane and components being removed. As mention earlier, cellulose acetate was the main material used to

produce UF membranes in the 1960s. However, due to its poor thermal and chemical stability, as well as its limited range of operational pH, the UF membranes materials has developed to use a range of polymers and or polymer blends. Polymers such as polyacrylonitrile, aromatic polyamides, polysulfone and polyvinylidene fluoride have been employed. This development of membrane materials allowed the new membranes to withstand higher operating temperatures and pressures, broader range of pH and allowed better chemical resistance, which helped broaden the application purposes (Fane et al., 2011). Two well known rejection mechanisms of membranes include electrostatic repulsion, which occurs between membrane surface and organic substances and Donnan exclusion, which happens between membrane surface and inorganic substances. As in the name, electrostatic repulsion, membrane surface and organic substances removed are conditioned to have the same charge in order to get an optimum repulsion performance. Similar to electrostatic repulsion, the Donnan exclusion is utilized through a negatively charged surface and the same negative charged (co-ions) of an inorganic species. The state of optimal Donnan exclusion is achieved following the establishment of electrochemical equilibrium between the solution and the membrane.

Nanofiltration is relatively newer membrane, with the term first used in the 1980s by FilmTec (Fane et al., 2011). NF membranes have properties between UF and RO membranes, with a pore size of around 1 nm, which equals to a molecular weight cut off (MWCO) of 300-500 Da. NF membranes operate by both sieving and mass diffusion transport mechanisms. Additionally, NF membranes surfaces are charged due to the dissociation of surface functional groups or adsorption of a charged solute, as such electrostatic interactions play a large role in the transport and selectivity behaviour. NF membranes are able to remove multivalent salts, but have a high permeability of monovalent salts. Operating pressure for NF membranes can range from 3 – 20 bar (Hilal et al., 2004; Mohammad et al., 2015).

In 1959, Reid and Breton demonstrated that cellulose acetate membranes was able to separate salt from water, however, fluxes obtained were too small to

be practical (Reid & Breton, 1959). Following this, discoveries by Loeb and Sourirajan, which developed the first synthetic RO membrane and Cadotte and Peterson, who synthesised a highly efficient thin film composite membrane, allowed the development of large scale and economically feasible RO membranes (Cadotte & Petersen, 1981; Loeb & Sourirajan, 1963). RO membranes are considered to be nonporous. This means that the mechanism of separation is by diffusion of the solvent through the membrane. The RO membrane is made up of a "dynamic" polymer network which allows water molecules to enter. RO membranes are generally asymmetric, thin -film composite membranes. Operating pressures for RO is dependent on the osmotic pressure of the solution and can range from 2 -17 bar for brackish water to 30-80 bar for seawater desalination (Cadotte & Petersen, 1981; Fane et al., 2011; Lachish, 2002).

2.4.3.3. Membrane Fouling

The biggest obstacle that faces membranes currently is the decline of the permeate flux over time due to fouling of the membrane. Membranes are operated either as constant permeate flux with variable transmembrane pressure (TMP) or constant TMP with a variable permeate flux. When fouling occurs, depending on the operational mode, either TMP increases to maintain constant flux, or there is a drop in flux when TMP is constant. This fouling can be classified as reversible and irreversible. Reversible fouling mostly occurs as a cake layer or concentration polarization at the membrane surface. Reversible fouling can typically be cleaned physically by back washing or chemically enhanced backwashing. Irreversible fouling occurs by chemisorption and pore plugging mechanisms. The TMP or flux of the membrane is not recoverable with irreversible fouling. Thus, the membrane must either goes through extensive chemical cleaning or be replaced, which are both costly.

Foulants can typically be classified into four categories:

- Particulates: Organic and inorganic particles can physically bind to the membrane surface, causing blockage of the pores and develop a cake layer hindering transport to the surface of the membrane.

- Organic: Dissolved components and colloids (e.g. humic and fulvic acids) can adsorb onto the membrane surface.

- Inorganic: Dissolved foulants (e.g. iron, manganese and silica) can precipitate on the membrane depending on the pH of the solution causing scaling. Residual coagulant/flocculant can also be present as an inorganic foulant.

- Micro-biological organisms: Often referred to as biofouling, micro-biological contaminants such as algae and bacteria can adhere to the membrane surface.

Membrane fouling by silica is a major challenge in water treatment, especially of brackish ground water which has higher silica concentrations. Silica scaling on membranes causes reduction in the permeate flux, and is resistant to simple cleaning methods (Bush et al., 2018; Koo et al., 2001). Studies by Bush et al showed that both acidification or alkalization of the silica solution, so that it was outside the ideal pH of polymerisation, were effective pretreatment strategies to reduce the silica scaling on membranes. They found that flushing the membrane using deionized water had no significant impact in removing silica scale (Bush et al., 2018). Studies by Koo determined that the presence of calcium and magnesium in the water enhanced the silica polymerisation process, where at silica concentrations of 300 ppm was metastable, and with the addition of calcium and magnesium, helped catalyse the polymerisation of silica (Koo et al., 2001). Other contaminants such as iron have also been shown to have a significant impact on the fouling of the membrane. Studies done by Sahachaiyunta showed that SEM images of fouled membranes with iron present had differing structures compared to other inorganics such as barium, manganese and nickel (Sahachaiyunta et al., 2002). Silica concentrations also showed a major role in the scaling mechanism on the membrane, as demonstrated by Semiat et al, who gathered evidence that showed at low concentrations of silica, deposition occurred by monomeric species, whereas, at higher concentrations silica deposition involved polymerized colloidal particles (Semiat et al., 2003).

Various methods exist to produce membranes, the selection depends on the choice of polymer and desired structure of the membrane. The most commonly applied fabrication methods include phase inversion, interfacial polymerisation stretching, track etching and electrospinning.

Phase inversion is the most common method and can be described as a homogeneous polymer solution being transferred in a controlled manner from a liquid to solid state (Drioli & Giorno, 2009). The method can be classified into four different categories; non-solvent induced phase conversion (NIPS), Thermal induced phase separation (TIPS), Vapour induced phase separation (VIPS), and Evaporation induced phase separation (EIPS) (Bazargan, 2022; Duraikkannu et al., 2021). NIPS is a well-established membrane preparation method, which the liquid-liquid de-mixing and solvent-nonsolvent diffusion rate determine the morphology of the membrane (Figoli et al., 2014). Other factors such as concentration of the polymer is another important factor in the fabrication process. Increasing the polymer concentrations in the solution, produces membranes with smaller sized pores which reduces the porosity. UF membranes are typically obtained when polymer concentration range is 12-20 wt%, where as RO membranes are concentrations >20 wt%. (Baker, 2004; Lalia et al., 2013).

2.4.3.5.Material and solvent used

The material selection of the membrane would depend on the application for which it would be used for. Synthetic organic polymers are typically the go to material for fabrication of membranes. These include the likes of, polysulfone (PSF), polyamide (PA), cellulose acetate (CA), polyethersulfone (PES) and polyvinylidene fluoride (PVDF).

Due to the hydrophobic nature of polymers such as PVDF, strong polar solvents are required to dissolve the PVDF. Various solvents have been investigated for the purpose of dissolving PVDF, including such solvents as, N,N-dimethyl-acetamide (DMAc), N,N-dimethylformaide (DMF) and N-methyl-2-pyrrolidone (NMP). There are concerns however that these solvents have negative impacts on the

environment and human health. Further studies in required to find solutions for greener, low-toxicity and more sustainable solvents (Clark & Tavener, 2007; Dong et al., 2021).

2.4.3.6. Modified membranes with GO and CNTs

Polymer membranes are restricted inherent challenges such as permeability/selectivity trade off and tendency to foul. Nanomaterials such as graphene oxide (GO) and carbon nanotubes (CNTs) are regarded as promising materials to help polymer membranes overcome these limitations due to their superior mechanical stability, hydrophilicity and biocidal properties (Wang et al., 2018). In addition to these characteristics, use of GO and CNTs in membranes alters the physical/chemical properties of the polymeric membrane, which has significant impact on the separation performance parameters such as porosity, pore size, surface roughness, charge of the membrane and hydrophilicity (Gupta et al., 2016; Marjani et al., 2020).

2.4.3.7. GO membranes in water treatment

Graphene by definition is a one-atom-thick 2D sheet of sp^2 hybridized carbon atoms, which are densely packed in a hexagonal honeycomb lattice (Kim et al., 2010). The effectiveness of the graphene, in a graphene-polymer composite depends on the quality of dispersion within the polymer matrix, as it tends to agglomerate (Kuilla et al., 2010). Successful preparation of GO polymer membranes has been produced by the phase inversion method, however, the nanofillers are dispersed in the solvent prior to the preparation of the casting solution (Wang et al., 2018).

GO-enhanced membranes have shown to increase the permeability in a variety of mechanisms for UF membranes. Studies by Wang et al who fabricated novel GO-PVDF blended membranes, showed that the permeability of PVDF membrane with 0.2 wt% GO, increased the permeability by 96.4% compared to PVDF membrane, due to increased pore channels and hydrophilicities (Wang et al., 2012).

Other studies by Chang et al, have also demonstrated dramatic increases in water flux with PVDF/GO membranes, due to the increased hydrophilicity and

decreased surface roughness (Chang et al., 2014). Additionally, they demonstrated the increase of antifouling properties of the membrane. This was further studied by Zhao et al who demonstrated an increase in fouling resistance of GO/PVDF membranes, due to improved hydrophilicity and smoother surface membrane (Zhao et al., 2013).

The use of GO in membranes has shown to improve the mechanical properties of the membrane. Studies by Ionita et al that through thermogravimetric analysis (TGA), the thermal stability of polysulfone/GO membranes had improved considerably (Ionita et al., 2015). Other studies by Xu et al discovered that tensile strength of PVDF/functionalised GO had improved by up to 69% compared to pure PVDF membrane (Xu et al., 2014).

Membrane selectivity is determined by several factors, including pore size and distribution and surface charge. Studies by Wang et al had found that the mean pore size had increased from 25.1 nm to 55.3 nm with PVDF/GO membrane, with content of 0.20 wt% of GO, with GO above this value had the reverse effect, and pore size decreased (Wang et al., 2012). The surface charge is another key feature and helps to understand and predict the antifouling characteristics of the membrane. Studies by Shukla et al who made polyphenylsulfone blended GO membranes, found that with the addition of GO, the surface zeta potential had decreased (Shukla et al., 2017). This helped the antifouling properties of the membrane with the proteins being used due to the adsorption inhibition effect.

2.4.3.8.   CNT membranes

Carbon nanotubes (CNTs) are sp^2 nano carbon materials with tubular structures compose of rolled-up graphene sheets (Maruyama, 2021). CNTs are classified into two types, single walled CNTs and multiwalled CNTs. CNTs is one of the favoured candidates for the advancement of membrane performance, due to its unique properties such as excellent adsorption capacity by high specific area (Pan & Xing, 2008), electroconductivity (Wang & Weng, 2018) and enhanced hydrophilicity and near frictionless encounter with water (Secchi et al., 2016). However, some of the challenges associated with CNT/polymer membranes is the

trade off between high removal efficiency and adhesion of foulants to the membrane as well as CNTs tendency to agglomerate with each other in dispersion of the solvent. The agglomeration of CNTs is due to a strong π-π stacking interaction with itself, which results in a poor interfacial interaction between the CNT and polymer (Andrews & Weisenberger, 2004).

As with GO, addition of CNTs to polymer membranes has an influence on the physio-chemical properties. A chemical characteristic of membranes is recognized as hydrophilicity, this is typically measured as the water contact angle, in which, a decrease in the angle relates to an increase in hydrophilicity. Various studies have shown that with differing CNT ratios, on average, the contact angle decreases with the addition of CNTs (Choi et al., 2006; Kim et al., 2020; Otitoju et al., 2018). This increase in hydrophilicity is resulted in reducing fouling on the membrane during operation.

Many studies have demonstrated that presence of CNTs improved the performances of the modified membrane. The improvement of permeability could be due to the larger pore size as well as porosity of the membrane due to the presence of CNTs (Hosseini et al., 2023; Khalid et al., 2015; Zhang et al., 2013). For the case of mixed matrix membranes with CNT, preparation by phase inversion and solution precipitation, may be due to interaction of CNT in the casting solution. The hydrophilic nature of CNTs can contribute to faster exchange of the solvent and non solvent resulting in higher porosity (Sianipar et al., 2017; Wu et al., 2010).

One of the major benefits of increased hydrophilicity by the addition of CNTs to membranes is the increased antifouling property of the membrane. The flux recovery ratio (FRR) and total fouling resistance (R_T) are parameters used to quantify the antifouling performance. FRR defines the recovery ability of the membrane after fouling occurs, while total fouling resistance is the defines the total fouling number occurring on the surface of the membrane. High permeability of a fouled membrane during operation and after backwashing, decreases R_T and increases FRR number, respectively (Lee et al., 2001; Rezakazemi et al., 2018; Zhang et al., 2016). Studies by Khalid et al, developed

polysulfone/CNT nanocomposite membranes which showed a much higher flux recovery ratio (83%) compared to the base membrane (57%) as well as a reduction in the irreversible resistance by 26% (Khalid et al., 2015). Similar studies by Moon Son et al showed that polyether sulfone membranes with CNTs had a greater flux recovery ratio compared to the base membrane (Son et al., 2015).

2.4.4. Ion exchange

2.4.4.1. General

One of the first mentions of ion exchange applied was by Aristotle, who observed that some types of sand was able to remove impurities from sea water. Since then, the development of ion exchange has come a long way, with improvements on the process to the manufacturing of ion exchange resins (Lucy, 2003). The ion exchange process is typically defined as the process that removes ions from water by exchanging them for other ions, be it in a direct e.g. ion exchange resins, or indirect, ion exchange membranes (Kumar & Jain, 2013). Traditionally boiler feedwater is treated by ion exchange demineralisers, to remove ionic constituents which can cause scaling within the boiler (Scott, 1995).

2.4.4.2. Mechanism

Ion exchange is a chemical reaction in which free mobile ions of a solid (the ion exchanger) are exchanged with ions of similar charge in solution. An ion exchanger is a water-insoluble substance. Below is a generic equation representing the ion exchange reaction:

$$M^+A^- + B^- \leftrightarrow M^+B^- + A^-$$
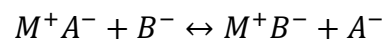
Which, M^+A^-, represents the solid exchanger carrying the Anion A^-, which exchanges with the solution phase containing B^- anions.

When an ion exchanger comes into contact with a mobile phase ion of the same charge, an equilibrium situation will be achieved, the thermodynamic chemical potential for each ion is the same inside and outside of the resin (Slater, 2013). A number of factors determine the equilibrium state, with prediction from first principles being difficult due to the ion activities and the relatively high concentrated environment of the resin.

The ion exchange process itself is accompanied by transfer of ions from the interphase boundary, which includes the chemical reaction itself, diffusion inside the material and diffusion in the surrounding solution (Kumar & Jain, 2013).

2.4.4.3. *Selectivity*

Selectivity is a parameter which in simple terms can be defined as the preference of one ion over another for exchange on the resin site. If assumed that ion exchange is a simple stoichiometric reaction then the mass action laws can be applied to obtain an equilibrium expression. For example, the following reaction (Morgan et al., 1995):

$$n[\overline{R^{\mp}}]A^{\mp} + B^{n\mp} \leftrightarrow [n\overline{R^{\mp}}]B^{n\mp} + nA^{\mp}$$
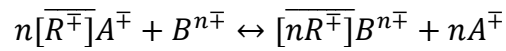
Where $\overline{R^{\mp}}$ is the ionic group attached to the resin, A and B are the exchanging ions and n is the valence of the exchanging ion. With respect to equation above, for a binary exchange reaction, the selectivity can be expressed as:

$$K_B^A = \frac{[A^{\mp}]^n[\overline{R^{\mp}B^{n\mp}}]}{[\overline{R^{\mp}A^{\mp}}]^n[B^{n\mp}]}$$

Where K_B^A is the selectivity coefficient, $[A^{\mp}]$ is the aqueous phase concentration of pre-saturant ion (mol/L), $[B^{n\mp}]$ is the aqueous phase concentration of counterion (mol/L) and $[\overline{R^{\mp}B^{n\mp}}]$ and $[\overline{R^{\mp}A^{\mp}}]^n$ are the activities of the resin pre-saturant ion and counter ion respectively. Ion exchange resin manufactures typically provide equilibrium data as selectivity coefficients (John C. Crittenden, 2012).

2.4.4.4. *Kinetics*

The kinetics of ion exchange is dependant on a combined effect of liquid and solid phase transport, and the reaction between the counterions and fixed ionic group on the resin. Kinetics of mass transfer plays an important role in the performance of the ion exchange resin. Most commonly ion exchange resins kinetics are purely dependent on diffusion.

Two main rate determining steps are considered in most ion exchange rate kinetics; the diffusion of ions inside the material (referred to as particle diffusion) and the diffusion of ions through the liquid film (referred to as film diffusion). The rate of ion exchange is determined by the slower of the two processes. Film diffusion control may prevail in systems with ion exchangers of high concentration of fixed ionic groups, low degree of crosslinks, small particle size, dilute solutions and inefficient agitation (Helfferich, 1995).

2.4.4.5. Ion exchange resin

Synthetic ion exchange resins are commonly used in water treatment, due to their durability and properties which can be modified to selectively remove cations and anions. The resin itself is typically composed of a crosslinked polymer matrix that contains covalently bonded functional groups with fixed ionic charges. Divinylbenzene (DVB) is used to crosslink the polymer backbone.

Based on the functional groups bonded to the resin four general classifications of resins exist, including, strong acid cation (SAC), weak acid cation (WAC), strong base anion (SBA) and weak base anion (WBA). For the purpose of this review only anion exchange resin will be discussed. Table 2.2 shows the characteristics of anion exchange resins used in water treatment.

Table 2.2. Types of anionic ion exchange resin

Resin type	Functional group	Regenerant ion	pK	Exchange capacity (meq/L)
Strong base anion (type 1)	$R(CH_3)_3N^+$	OH^- or Cl^-	>13	1-1.4
Strong base anion (type 2)	$R(CH_3)_2(CH_3CH_2OH)N^+$	OH^- or Cl^-	>13	2-2.5
Weak base anion	$R(CH_3)_2NH^+$	OH^-	5.7-7.3	2-3

2.4.4.6. *Removal of silica using ion exchange*

Dissolved silica in water is typically removed by strong base anion resins, while colloidal silica present in water is difficult to remove with ion exchange. Due to the size and low ionic properties of colloidal silica, it becomes very difficult to remove via ion exchange. Studies by Agui et al showed that colloidal silica was able to adsorb well onto the surface of strong base anion resins (Agui et al., 1993). They also demonstrated that resins with larger pores was able to adsorb greater amounts of the colloidal silica.

Sasan et el conducted research on selective removal of dissolved silica using inorganic anion exchangers, their studies showed that hydrotalcite (HTC) anion exchanger had an adsorption capacity of 45 mg SiO_2/g of HTC. They also found that HTC could selectively remove silica with competing ions such as sulphate and chloride present (Sasan et al., 2017).

Pilot studies by Roy Osmun studied silica removal using strong basic anion resins, the study was able to prove that the resin was able to reduce a feed water containing 3 ppm of silica as $CaCO_3$, down to 0.05 ppm of silica as $CaCO_3$ (Osmun & Wirth, 1951).

Studies by Ben Sik Ali et al looked at developing thermodynamic and kinetic models for silica removal via ion exchange. They showed that the resin showed better selectivity for silica when it was in the hydroxide form, compared to the chloride form. Resins showed they were in the third order reaction at temperatures of 20 and 30 °C (Ben Sik Ali et al., 2004).

2.4.5. Advanced oxidation processes

2.4.5.1. General

For the treatment of drinking water, a group of chemical oxidative technologies classified as advanced oxidation processes (AOPs) have had a significant level of interest over the last three decades. They are known for producing highly reactive and non-selective hydroxyl radicals, which are strong oxidants in aqueous solutions (Miklos et al., 2018). Hydroxyl radicals are able to oxidize nearly all the organic compounds to water, carbon dioxide and mineral salts (Wang & Xu, 2012). Out of the many AOPs developed, ozone has garnered major interest.

There have been significant research done on ozone with respect to optimisation, modelling and in-depth reaction kinetics (Ma et al., 2021).

2.4.5.2. Ozone

Ozone in water treatment has been used for disinfection, odour control and colour removal. Ozone can oxidise organic and inorganic species in wide range of pHs. Ozonation is achieved in two ways, direct and indirect reactions (Agustina et al., 2005). Direct reaction occurs when ozone reacts with organic matter, and is highly selective. It attacks organic compounds with reducible double bonds. Indirect reactions refer to the decomposition of ozone in water to form hydroxyl radicals which join in the oxidation reactions (Ma et al., 2021).

Presently the method of ozone generation is by dielectric barrier discharge (DBD) method, the system generates a corona in the gas through alternating high-voltage electric field. The free high electrons dissociate oxygen molecules, which are polymerised into ozone molecules by collision (Jodzis & Zięba, 2018).

Studies by Sadrnourmohamadi have demonstrated ozonation prior to coagulation showed enhanced DOC removal, at ozone doses of 0.6-0.8 mg/L. The researchers attributed this to ozone induced particle destabilisation which resulted in lower particle surface charge (Sadrnourmohamadi & Gorczyca, 2015).

Chheda et al studied the surface dynamics of ozone induced particle destabilization on montmorillonite. They found that ozonation had decreased the surface charge and the Lewis base parameter. They credited the modification in the surface thermodynamics to the partial dealumination of montmorillonite (Chheda & Grasso, 1994).

To summarise:

- This chapter addresses water treatment challenges in an integrated steel plant, specifically at Tata Steel Port Talbot, with a focus on removal of silica. Silica is a major contaminant causing scaling, corrosion, and operation inefficiencies in boiler systems.
- The boiler at Port Talbot site operates at very high pressures (~126 bar) and uses processed water from the River Afan. Water treatment involves

multiple stages including, coagulation, filtration and ion exchange producing demineralised water. In recent years, silica in the boilers has exceeded recommended concentrations, increasing the potential of silica deposition.

- Silica in water can exist as dissolved, colloidal and reactive species. The plant primarily faces challenges associated with colloidal silica.

- A number of treatment technologies exist in removing silica including, coagulation/flocculation, membranes and ion exchange. Taking a hybrid approach and combining technologies can be implemented to achieve optimal silica removal.

2.5. References

Abe, T., Kobayashi, S., & Kobayashi, M. (2011). Aggregation of colloidal silica particles in the presence of fulvic acid, humic acid, or alginate: Effects of ionic composition. *Colloids and Surfaces A: Physicochemical and Engineering Aspects, 379*(1), 21-26. https://doi.org/https://doi.org/10.1016/j.colsurfa.2010.11.052

Agui, W., Shimoyamada, H., Abe, M., & Ogino, K. (1993). Removal of Colloidal Silica from Water with Anion Exchange Resins. *Journal of Ion Exchange, 4*(3), 176-182. https://doi.org/10.5182/jaie.4.176

Agustina, T. E., Ang, H. M., & Vareek, V. K. (2005). A review of synergistic effect of photocatalysis and ozonation on wastewater treatment. *Journal of Photochemistry and Photobiology C: Photochemistry Reviews, 6*(4), 264-273. https://doi.org/https://doi.org/10.1016/j.jphotochemrev.2005.12.003

Allen, L. H., & Matijevic´, E. (1970). Stability of colloidal silica: II. Ion exchange. *Journal of Colloid and Interface Science, 33*(3), 420-429. https://doi.org/https://doi.org/10.1016/0021-9797(70)90234-1

Amjad, Z., & Koutsoukos, P. (2010). Mineral Scales and Deposits. In (pp. 1-20). https://doi.org/10.1201/9781420071450-c1

Andrews, R., & Weisenberger, M. C. (2004). Carbon nanotube polymer composites. *Current Opinion in Solid State and Materials Science, 8*(1), 31-37. https://doi.org/https://doi.org/10.1016/j.cossms.2003.10.006

Bahadori, A., & Vuthaluru, H. B. (2010). Prediction of silica carry-over and solubility in steam of boilers using simple correlation. *Applied Thermal Engineering, 30*(2), 250-253. https://doi.org/https://doi.org/10.1016/j.applthermaleng.2009.07.010

Baker, R. W. (2004). *Membrane Technology and Applications*. Wiley. https://books.google.co.uk/books?id=dLhSHOmdiOkC

Bazargan, A. (2022). *A Multidisciplinary Introduction to Desalination*. River Publishers. https://books.google.co.uk/books?id=V_yGEAAAQBAJ

Beckett, R. (1991). *Surface and Colloid Chemistry in Natural Waters and Water Treatment*. Springer US. https://books.google.co.uk/books?id=YiWiwl9eNHoC

Belton, D. J., Deschaume O Fau - Perry, C. C., & Perry, C. C. An overview of the fundamentals of the chemistry of silica with relevance to biosilicification and technological advances. (1742-4658 (Electronic)).

Ben Sik Ali, M., Hamrouni, B., Bouguecha, S., & Dhahbi, M. (2004). Silica removal using ion-exchange resins. *Desalination, 167*, 273–279. https://doi.org/10.1016/j.desal.2004.06.136

Bergna, H. E. (1994). Colloid Chemistry of Silica. In *The Colloid Chemistry of Silica* (Vol. 234, pp. 1-47). American Chemical Society. https://doi.org/doi:10.1021/ba-1994-0234.ch001

10.1021/ba-1994-0234.ch001

Behrman, A. S., & Gustafson, H. (1940). Removal of Silica from Water. *Industrial & Engineering Chemistry, 32*, 468-472.

Black, A. P., Buswell, A. M., Eidsness, F. A., & Black, A. L. (1957). Review of the jar test. *Journal (American Water Works Association), 49*(11), 1414-1424.

Black, A. P., & Vilaret, M. R. (1969). EFFECT OF PARTICLE SIZE ON TURBIDITY REMOVAL. *Journal AWWA, 61*(4), 209-214. https://doi.org/https://doi.org/10.1002/j.1551-8833.1969.tb03740.x

Bratby, J. (2016). *Coagulation and flocculation in water and wastewater treatment*. IWA publishing.

Bush, J. A., Vanneste, J., Gustafson, E. M., Waechter, C. A., Jassby, D., Turchi, C. S., & Cath, T. Y. (2018). Prevention and management of silica scaling in membrane distillation using pH adjustment. *Journal of membrane science, 554*, 366-377. https://doi.org/https://doi.org/10.1016/j.memsci.2018.02.059

Cadotte, J. E., & Petersen, R. J. (1981). Thin-Film Composite Reverse-Osmosis Membranes: Origin, Development, and Recent Advances. In *Synthetic Membranes:* (Vol. 153, pp. 305-326). AMERICAN CHEMICAL SOCIETY. https://doi.org/doi:10.1021/bk-1981-0153.ch021

10.1021/bk-1981-0153.ch021

Chang, X., Wang, Z., Quan, S., Xu, Y., Jiang, Z., & Shao, L. (2014). Exploring the synergetic effects of graphene oxide (GO) and polyvinylpyrrodione (PVP) on poly(vinylylidenefluoride) (PVDF) ultrafiltration membrane performance. *Applied Surface Science*, *316*, 537-548. https://doi.org/https://doi.org/10.1016/j.apsusc.2014.07.202

Chheda, P., & Grasso, D. (1994). Surface Thermodynamics of Ozone-Induced Particle Destabilization. *Langmuir*, *10*(4), 1044-1053. https://doi.org/10.1021/la00016a016

Ching, H.-W., Tanaka, T. S., & Elimelech, M. (1994). Dynamics of coagulation of kaolin particles with ferric chloride. *Water Research*, *28*(3), 559-569. https://doi.org/https://doi.org/10.1016/0043-1354(94)90007-8

Choi, J.-H., Jegal, J., & Kim, W.-N. (2006). Fabrication and characterization of multi-walled carbon nanotubes/polymer blend membranes. *Journal of membrane science*, *284*(1), 406-415. https://doi.org/https://doi.org/10.1016/j.memsci.2006.08.013

Choy, S. Y., Prasad, K. M. N., Wu, T. Y., Raghunandan, M. E., & Ramanan, R. N. (2014). Utilization of plant-based natural coagulants as future alternatives towards sustainable water clarification. *Journal of Environmental Sciences*, *26*(11), 2178-2189. https://doi.org/https://doi.org/10.1016/j.jes.2014.09.024

Chuang, S. H., Chang, T. C., Ouyang, C. F., & Leu, J. M. (2007). Colloidal silica removal in coagulation processes for wastewater reuse in a high-tech industrial park. *Water science and technology : a journal of the International Association on Water Pollution Research*, *55*, 187-195. https://doi.org/10.2166/wst.2007.054

Clark, J. H., & Tavener, S. J. (2007). Alternative Solvents: Shades of Green. *Organic Process Research & Development*, *11*(1), 149-155. https://doi.org/10.1021/op060160g

Crittenden, J. C., Trussell, R.R., Hand, D.W., Howe, K.J. and Tchobanoglous, G. (2012). Membrane Filtration. In *MWH's Water Treatment: Principles and Design, Third Edition* (pp. 819-902). https://doi.org/https://doi.org/10.1002/9781118131473.ch12

Crittenden, J. C., Trussell, R.R., Hand, D.W., Howe, K.J. and Tchobanoglous, G. ((2012). Coagulation and Flocculation. In *MWH's Water Treatment: Principles and Design, Third Edition* (pp. 541-639). https://doi.org/https://doi.org/10.1002/9781118131473.ch9

Daniel, F. (2009). *Nalco Water Handbook, Third Edition* (Third Edition ed.). McGraw-Hill Education. https://www.accessengineeringlibrary.com/content/book/9780071548830

Dardel, F. d. (2022). *Degasifier*.

Dietzel, M. (2000). Dissolution of silicates and the stability of polysilicic acid.

Geochimica et Cosmochimica Acta, 64(19), 3275-3281. https://doi.org/https://doi.org/10.1016/S0016-7037(00)00426-9

Den, W., & Wang, C.-J. (2008). Removal of silica from brackish water by electrocoagulation pretreatment to prevent fouling of reverse osmosis membranes. *Separation and purification technology, 59*(3), 318-325. https://doi.org/https://doi.org/10.1016/j.seppur.2007.07.025

Dentel, S. K., & Gossett, J. M. (1988). Mechanisms of Coagulation With Aluminum Salts. *Journal AWWA, 80*(4), 187-198. https://doi.org/https://doi.org/10.1002/j.1551-8833.1988.tb03025.x

Dong, X., Lu, D., Harris, T. A. L., & Escobar, I. C. (2021). Polymers and Solvents Used in Membrane Fabrication: A Review Focusing on Sustainable Membrane Development. *Membranes, 11*(5).

Drioli, E., & Giorno, L. (2009). *Membrane Operations: Innovative Separations and Transformations*. Wiley. https://books.google.co.uk/books?id=1pXNwAEACAAJ

Duan, J., & Gregory, J. (2003). Coagulation by hydrolysing metal salts. *Advances in colloid and interface science, 100-102*, 475-502. https://doi.org/https://doi.org/10.1016/S0001-8686(02)00067-2

Duraikkannu, S. L., Castro-Muñoz, R., & Figoli, A. (2021). A review on phase-inversion technique-based polymer microsphere fabrication. *Colloid and*

Interface Science Communications, *40*, 100329. https://doi.org/https://doi.org/10.1016/j.colcom.2020.100329

Fane, A. G., Wang, R., & Jia, Y. (2011). Membrane Technology: Past, Present and Future. In L. K. Wang, J. P. Chen, Y.-T. Hung, & N. K. Shammas (Eds.), *Membrane and Desalination Technologies* (pp. 1-45). Humana Press. https://doi.org/10.1007/978-1-59745-278-6_1

Figoli, A., Marino, T., Simone, S., Di Nicolò, E., Li, X. M., He, T., Tornaghi, S., & Drioli, E. (2014). Towards non-toxic solvents for membrane preparation: a review [10.1039/C4GC00613E]. *Green Chemistry*, *16*(9), 4034-4059. https://doi.org/10.1039/C4GC00613E

Fleming, B. A., & Crerar, D. A. (1982). Silicic acid ionization and calculation of silica solubility at elevated temperature and pH application to geothermal fluid processing and reinjection. *Geothermics*, *11*(1), 15-29. https://doi.org/https://doi.org/10.1016/0375-6505(82)90004-9

Ghafari, S., Aziz, H. A., & Bashir, M. J. K. (2010). The use of poly-aluminum chloride and alum for the treatment of partially stabilized leachate: A comparative study. *Desalination*, *257*(1), 110-116. https://doi.org/https://doi.org/10.1016/j.desal.2010.02.037

Gough, R., Holliman, P. J., Heard, T. R., & Freeman, C. (2014). Dissolved organic carbon and trihalomethane formation potential removal during coagulation of a typical UK upland water with alum, PAX-18 and PIX-322. *Journal of Water Supply: Research and Technology—AQUA, 63*(8), 650-660.

Greenberg, S. A., & Sinclair, D. (1955). The Polymerization of Silicic Acid. *The Journal of Physical Chemistry*, *59*(5), 435-440. https://doi.org/10.1021/j150527a014

Gregor, J. E., Nokes, C. J., & Fenton, E. (1997). Optimising natural organic matter removal from low turbidity waters by controlled pH adjustment of aluminium coagulation. *Water Research*, *31*(12), 2949-2958. https://doi.org/https://doi.org/10.1016/S0043-1354(97)00154-1

Gupta, V. K., Moradi, O., Tyagi, I., Agarwal, S., Sadegh, H., Shahryari-Ghoshekandi, R., Makhlouf, A. S. H., Goodarzi, M., & Garshasbi, A.

(2016). Study on the removal of heavy metal ions from industry waste by carbon nanotubes: Effect of the surface modification: a review. *Critical reviews in environmental science and technology*, *46*(2), 93-118. https://doi.org/10.1080/10643389.2015.1061874

Haribhakti, P., Joshi, P. B., & Kumar, R. (2018a). *Failure Investigation of Boiler Tubes: A Comprehensive Approach*. https://doi.org/10.31399/asm.tb.fibtca.9781627082532

Haribhakti, P., Joshi, P. B., & Kumar, R. (2018b). Role of Water Chemistry in Boiler Tube Failure. In P. Haribhakti, P. B. Joshi, & R. Kumar (Eds.), *Failure Investigation of Boiler Tubes: A Comprehensive Approach* (pp. 0). ASM International. https://doi.org/10.31399/asm.tb.fibtca.t52430379

Healy, T. W., & Mer, V. K. L. (1962). THE ADSORPTION-FLOCCULATION REACTIONS OF A POLYMER WITH AN AQUEOUS COLLOIDAL DISPERSION. *The Journal of Physical Chemistry*, *66*(10), 1835-1838. https://doi.org/10.1021/j100816a014

Helfferich, F. G. (1995). *Ion exchange*. Courier Corporation.

Hilal, N., Al-Zoubi, H., Darwish, N. A., Mohamma, A. W., & Arabi, M. A. (2004). A comprehensive review of nanofiltration membranes: Treatment, pretreatment, modelling, and atomic force microscopy. *Desalination*, *170*(3), 281-308.

Hingston, F., & Raupach, M. (1967). The reaction between monosilicic acid and aluminium hydroxide. I. Kinetics of adsorption of silicic acid by aluminium hydroxide. *Soil Research*, *5*, 295-309.

Hogg, R., Bunnaul, P., & Suharyono, H. (1993). Chemical and physical variables in polymer-induced flocculation. *Mining, Metallurgy & Exploration*, *10*(2), 81-85. https://doi.org/10.1007/BF03403004

Hosseini, S. M., Mohammadianfar, S., Farahani, S. K., & Solhi, S. (2023). Polyether sulfone-graphite nanocomposite for nanofiltration membrane with enhanced separation, antifouling and antibacterial properties. *Korean Journal of Chemical Engineering*, *40*(1), 185-194. https://doi.org/10.1007/s11814-022-1266-1

Hudson Jr, H. E., & Wagner, E. G. (1981). Conduct and uses of jar tests. *Journal AWWA*, *73*(4), 218-223. https://doi.org/https://doi.org/10.1002/j.1551-8833.1981.tb04683.x

Iler, R. K. (1979). *The chemistry of silica : solubility, polymerization, colloid and surface properties, and biochemistry / Ralph K. Iler*. Wiley.

Inc., P. M. R. (2014). BEHAVIOR OF SILICA IN ION EXCHANGE AND OTHER SYSTEMS.

Ionita, M., Vasile, E., Crica, L. E., Voicu, S. I., Pandele, A. M., Dinescu, S., Predoiu, L., Galateanu, B., Hermenean, A., & Costache, M. (2015). Synthesis, characterization and in vitro studies of polysulfone/graphene oxide composite membranes. *Composites Part B: Engineering*, *72*, 108-115. https://doi.org/https://doi.org/10.1016/j.compositesb.2014.11.040

Jodzis, S., & Zięba, M. (2018). Energy efficiency of an ozone generation process in oxygen. Analysis of a pulsed DBD system. *Vacuum*, *155*, 29-37. https://doi.org/https://doi.org/10.1016/j.vacuum.2018.05.035

John C. Crittenden, R. R. T., David W. Hand, Kerry J. Howe, George Tchobanoglous. (2012). Ion Exchange. In *MWH's Water Treatment: Principles and Design, Third Edition* (pp. 1263-1334). https://doi.org/https://doi.org/10.1002/9781118131473.ch16

Kang, G.-d., & Cao, Y.-m. (2014). Application and modification of poly(vinylidene fluoride) (PVDF) membranes – A review. *Journal of membrane science*, *463*, 145-165. https://doi.org/https://doi.org/10.1016/j.memsci.2014.03.055

Keeley, J., Jarvis, P., & Judd, S. J. (2014). Coagulant Recovery from Water Treatment Residuals: A Review of Applicable Technologies. *Critical reviews in environmental science and technology*, *44*(24), 2675-2719. https://doi.org/10.1080/10643389.2013.829766

Khalid, A., Al-Juhani, A. A., Al-Hamouz, O. C., Laoui, T., Khan, Z., & Atieh, M. A. (2015). Preparation and properties of nanocomposite polysulfone/multi-walled carbon nanotubes membranes for desalination. *Desalination*, *367*, 134-144. https://doi.org/https://doi.org/10.1016/j.desal.2015.04.001

Kim, H., Abdala, A. A., & Macosko, C. W. (2010). Graphene/Polymer Nanocomposites. *Macromolecules*, *43*(16), 6515-6530. https://doi.org/10.1021/ma100572e

Kim, Y., Yang, E., Park, H., & Choi, H. (2020). Anti-biofouling effect of a thin film nanocomposite membrane with a functionalized-carbon-nanotube-blended polymeric support for the pressure-retarded osmosis process [10.1039/C9RA08870A]. *RSC advances, 10*(10), 5697-5703. https://doi.org/10.1039/C9RA08870A

Kobayashi, M., Juillerat, F., Galletto, P., Bowen, P., & Borkovec, M. (2005). Aggregation and Charging of Colloidal Silica Particles: Effect of Particle Size. *Langmuir, 21*(13), 5761-5769. https://doi.org/10.1021/la046829z

Koo, T., Lee, Y. J., & Sheikholeslami, R. (2001). Silica fouling and cleaning of reverse osmosis membranes. *Desalination, 139*(1), 43-56. https://doi.org/https://doi.org/10.1016/S0011-9164(01)00293-4

Krauskopf, K. B. (1956). Dissolution and precipitation of silica at low temperatures. *Geochimica et Cosmochimica Acta, 10*(1), 1-26. https://doi.org/https://doi.org/10.1016/0016-7037(56)90009-6

Kuilla, T., Bhadra, S., Yao, D., Kim, N. H., Bose, S., & Lee, J. H. (2010). Recent advances in graphene based polymer composites. *Progress in Polymer Science, 35*(11), 1350-1375. https://doi.org/https://doi.org/10.1016/j.progpolymsci.2010.07.005

Kumar, S., & Jain, S. (2013). History, introduction, and kinetics of ion exchange materials. *Journal of Chemistry, 2013*.

Lachish, U. (2002). *Optimizing the Efficiency of Reverse Osmosis Seawater Desalination*. https://doi.org/10.13140/RG.2.2.12099.20003

Lalia, B. S., Kochkodan, V., Hashaikeh, R., & Hilal, N. (2013). A review on membrane fabrication: Structure, properties and performance relationship. *Desalination, 326*, 77-95. https://doi.org/https://doi.org/10.1016/j.desal.2013.06.016

Lee, H., Amy, G., Cho, J., Yoon, Y., Moon, S.-H., & Kim, I. S. (2001). Cleaning strategies for flux recovery of an ultrafiltration membrane fouled by

natural organic matter. *Water Research, 35*(14), 3301-3308. https://doi.org/https://doi.org/10.1016/S0043-1354(01)00063-X

Lenard, J. (2014). Flat Rolling – A General Discussion. In (pp. 39-55). https://doi.org/10.1016/B978-0-08-099418-5.00004-4

Lester-Card, E., Smith, G., Lloyd, G., & Tizaoui, C. (2023). A green approach for the treatment of oily steelworks wastewater using natural coagulant of Moringa oleifera seed. *Bioresource Technology Reports, 22*, 101393. https://doi.org/https://doi.org/10.1016/j.biteb.2023.101393

Loeb, S., & Sourirajan, S. (1963). Sea Water Demineralization by Means of an Osmotic Membrane. In *Saline Water Conversion—II* (Vol. 38, pp. 117-132). AMERICAN CHEMICAL SOCIETY. https://doi.org/doi:10.1021/ba-1963-0038.ch009

10.1021/ba-1963-0038.ch009

Lucy, C. A. (2003). Evolution of ion-exchange: from Moses to the Manhattan Project to Modern Times. *Journal of Chromatography A, 1000*(1), 711-724. https://doi.org/https://doi.org/10.1016/S0021-9673(03)00528-4

Lunevich, L. (2019). Aqueous silica and silica polymerisation. *Desalination-Challenges and Opportunities, 6*, 1-19.

Ma, D., Yi, H., Lai, C., Liu, X., Huo, X., An, Z., Li, L., Fu, Y., Li, B., Zhang, M., Qin, L., Liu, S., & Yang, L. (2021). Critical review of advanced oxidation processes in organic wastewater treatment. *Chemosphere, 275*, 130104. https://doi.org/https://doi.org/10.1016/j.chemosphere.2021.130104

Maier, H. R., Morgan, N., & Chow, C. W. K. (2004). Use of artificial neural networks for predicting optimal alum doses and treated water quality parameters. *Environmental Modelling & Software, 19*(5), 485-494. https://doi.org/https://doi.org/10.1016/S1364-8152(03)00163-4

Makrides, A. C., Turner, M. J., & Slaughter, J. (1980). Condensation of silica from supersaturated silicic acid solutions. *Journal of Colloid and Interface Science, 73*, 345-367.

Mao, R., Wang, Y., Zhang, B., Xu, W., Dong, M., & Gao, B. (2013). Impact of enhanced coagulation ways on flocs properties and membrane fouling:

Increasing dosage and applying new composite coagulant. *Desalination*, *314*, 161-168. https://doi.org/https://doi.org/10.1016/j.desal.2013.01.012

Marjani, A., Nakhjiri, A. T., Adimi, M., Jirandehi, H. F., & Shirazian, S. (2020). Effect of graphene oxide on modifying polyethersulfone membrane performance and its application in wastewater treatment. *Scientific Reports*, *10*(1), 2049. https://doi.org/10.1038/s41598-020-58472-y

Maruyama, T. (2021). Chapter 6 - Carbon nanotubes. In S. Thomas, C. Sarathchandran, S. A. Ilangovan, & J. C. Moreno-Piraján (Eds.), *Handbook of Carbon-Based Nanomaterials* (pp. 299-319). Elsevier. https://doi.org/https://doi.org/10.1016/B978-0-12-821996-6.00009-9

Matilainen, A., Lindqvist, N., & Tuhkanen, T. (2005). Comparison of the Effiency of Aluminium and Ferric Sulphate in the Removal of Natural Organic Matter During Drinking Water Treatment Process. *Environmental Technology*, *26*(8), 867-876. https://doi.org/10.1080/09593332608618502

Miklos, D. B., Remy, C., Jekel, M., Linden, K. G., Drewes, J. E., & Hübner, U. (2018). Evaluation of advanced oxidation processes for water and wastewater treatment – A critical review. *Water Research*, *139*, 118-131. https://doi.org/https://doi.org/10.1016/j.watres.2018.03.042

Mohammad, A. W., Teow, Y., Ang, W., Chung, Y., Oatley-Radcliffe, D., & Hilal, N. (2015). Nanofiltration membranes review: Recent advances and future prospects. *Desalination*, *356*, 226-254.

Moran, S. (2018). Chapter 1 - Introduction: The nature of water and effluent treatment plant design. In S. Moran (Ed.), *An Applied Guide to Water and Effluent Treatment Plant Design* (pp. 1-12). Butterworth-Heinemann. https://doi.org/https://doi.org/10.1016/B978-0-12-811309-7.00001-1

Morgan, J. D., Napper, D. H., & Warr, G. G. (1995). Thermodynamics of Ion Exchange Selectivity at Interfaces. *The Journal of Physical Chemistry*, *99*(23), 9458-9465. https://doi.org/10.1021/j100023a024

Naceradska, J., Pivokonska, L., & Pivokonsky, M. (2019). On the importance of pH value in coagulation. *Journal of Water Supply: Research and Technology-Aqua*, *68*(3), 222-230. https://doi.org/10.2166/aqua.2019.155

Obotey Ezugbe, E., & Rathilal, S. (2020). Membrane Technologies in Wastewater Treatment: A Review. *Membranes, 10*(5).

Osmun, R., & Wirth, L. (1951). Silica Removal with Highly Basic Anion Exchange Resins. *Industrial & Engineering Chemistry, 43*(5), 1076-1079. https://doi.org/10.1021/ie50497a023

Otitoju, T. A., Ahmad, A. L., & Ooi, B. S. (2018). Recent advances in hydrophilic modification and performance of polyethersulfone (PES) membrane via additive blending [10.1039/C8RA03296C]. *RSC advances, 8*(40), 22710-22728. https://doi.org/10.1039/C8RA03296C

Packham, R. F. (1965). Some studies of the coagulation of dispersed clays with hydrolyzing salts. *Journal of Colloid Science, 20*(1), 81-92. https://doi.org/https://doi.org/10.1016/0095-8522(65)90094-2

Pan, B., & Xing, B. (2008). Adsorption Mechanisms of Organic Chemicals on Carbon Nanotubes. *Environmental Science & Technology, 42*(24), 9005-9013. https://doi.org/10.1021/es801777n

Randtke, S. J. (1988). Organic Contaminant Removal by Coagulation and Related Process Combinations. *Journal AWWA, 80*(5), 40-56. https://doi.org/https://doi.org/10.1002/j.1551-8833.1988.tb03037.x

Ratnaweera, H., & Fettig, J. (2015). State of the Art of Online Monitoring and Control of the Coagulation Process. *Water, 7*(11), 6574-6597.

Rattanakawin, C., & Hogg, R. (2001). Aggregate size distributions in flocculation. *Colloids and Surfaces A: Physicochemical and Engineering Aspects, 177*(2), 87-98. https://doi.org/https://doi.org/10.1016/S0927-7757(00)00662-2

Reid, C. E., & Breton, E. J. (1959). Water and ion flow across cellulosic membranes. *Journal of Applied Polymer Science, 1*(2), 133-143. https://doi.org/https://doi.org/10.1002/app.1959.070010202

Rezakazemi, M., Dashti, A., Riasat Harami, H., Hajilari, N., & Inamuddin. (2018). Fouling-resistant membranes for water reuse. *Environmental Chemistry Letters, 16*(3), 715-763. https://doi.org/10.1007/s10311-018-0717-8

Ruehrwein, R. A., & Ward, D. W. (1952). MECHANISM OF CLAY AGGREGATION BY POLYELECTROLYTES. *Soil Science, 73*, 485–492.

Sadrnourmohamadi, M., & Gorczyca, B. (2015). Effects of ozone as a stand-alone and coagulation-aid treatment on the reduction of trihalomethanes precursors from high DOC and hardness water. *Water Research*, *73*, 171-180. https://doi.org/https://doi.org/10.1016/j.watres.2015.01.023

Sahachaiyunta, P., Koo, T., & Sheikholeslami, R. (2002). Effect of several inorganic species on silica fouling in RO membranes. *Desalination*, *144*(1), 373-378. https://doi.org/https://doi.org/10.1016/S0011-9164(02)00346-6

Sasan, K., Brady, P. V., Krumhansl, J. L., & Nenoff, T. M. (2017). Removal of dissolved silica from industrial waters using inorganic ion exchangers. *Journal of Water Process Engineering*, *17*, 117-123. https://doi.org/https://doi.org/10.1016/j.jwpe.2017.02.006

Schenk, J. E., & Weber Jr, W. J. (1968). Chemical Interactions of Dissolved Silica With Iron (II) and (III). *Journal AWWA*, *60*(2), 199-212. https://doi.org/https://doi.org/10.1002/j.1551-8833.1968.tb03534.x

Scott, K. (1995). WATER PURIFICATION. In K. Scott (Ed.), *Handbook of Industrial Membranes* (pp. 521-572). Elsevier Science. https://doi.org/https://doi.org/10.1016/B978-185617233-2/50013-1

Secchi, E., Marbach, S., Niguès, A., Stein, D., Siria, A., & Bocquet, L. (2016). Massive radius-dependent flow slippage in carbon nanotubes. *Nature*, *537*(7619), 210-213. https://doi.org/10.1038/nature19315

Semiat, R., Sutzkover, I., & Hasson, D. (2003). Scaling of RO membranes from silica supersaturated solutions. *Desalination*, *157*(1), 169-191. https://doi.org/https://doi.org/10.1016/S0011-9164(03)00398-9

Shokri, A., & Sanavi Fard, M. (2023). Principles, operational challenges, and perspectives in boiler feedwater treatment process. *Environmental Advances*, *13*, 100389. https://doi.org/https://doi.org/10.1016/j.envadv.2023.100389

Shreir, L. L. (1994). Dissolved Oxygen. In L. L. Shreir, R. A. Jarman, & G. T. Burstein (Eds.), *Corrosion (Third Edition)* (pp. xv-xxiii). Butterworth-Heinemann. https://doi.org/https://doi.org/10.1016/B978-0-08-052351-4.50007-8

Shukla, A. K., Alam, J., Alhoshan, M., Dass, L. A., & Muthumareeswaran, M. R. (2017). Development of a nanocomposite ultrafiltration membrane based on polyphenylsulfone blended with graphene oxide. *Scientific Reports*, 7(1), 41976.

Sianipar, M., Kim, S. H., Khoiruddin, Iskandar, F., & Wenten, I. G. (2017). Functionalized carbon nanotube (CNT) membrane: progress and challenges [10.1039/C7RA08570B]. *RSC advances*, 7(81), 51175-51198. https://doi.org/10.1039/C7RA08570B

Singh, R. (2015). Chapter 1 - Introduction to Membrane Technology. In R. Singh (Ed.), *Membrane Technology and Engineering for Water Purification (Second Edition)* (pp. 1-80). Butterworth-Heinemann. https://doi.org/https://doi.org/10.1016/B978-0-444-63362-0.00001-X

Slater, M. J. (2013). *Principles of Ion Exchange Technology*. Elsevier Science. https://books.google.co.uk/books?id=Sbb-BAAAQBAJ

Smethurst, G. (1979). *Basic Water Treatment: For Application World-wide*. Telford. https://books.google.co.uk/books?id=BzVBAAAAYAAJ

Son, M., Choi, H.-g., Liu, L., Celik, E., Park, H., & Choi, H. (2015). Efficacy of carbon nanotube positioning in the polyethersulfone support layer on the performance of thin-film composite membrane for desalination. *Chemical engineering journal*, 266, 376-384. https://doi.org/https://doi.org/10.1016/j.cej.2014.12.108

Sparks, T., & Chase, G. (2016). Section 5 - Solid–Liquid Filtration – Examples of Processes. In T. Sparks & G. Chase (Eds.), *Filters and Filtration Handbook (Sixth Edition)* (pp. 297-359). Butterworth-Heinemann. https://doi.org/https://doi.org/10.1016/B978-0-08-099396-6.00005-8

Strathmann, H. (1981). Membrane separation processes. *Journal of membrane science*, 9(1), 121-189. https://doi.org/https://doi.org/10.1016/S0376-7388(00)85121-2

Umar, M., Roddick, F., & Fan, L. (2016). Comparison of coagulation efficiency of aluminium and ferric-based coagulants as pre-treatment for UVC/H2O2 treatment of wastewater RO concentrate. *Chemical engineering journal*, 284, 841-849. https://doi.org/https://doi.org/10.1016/j.cej.2015.08.109

Wang, J. L., & Xu, L. J. (2012). Advanced Oxidation Processes for Wastewater Treatment: Formation of Hydroxyl Radical and Application. *Critical reviews in environmental science and technology, 42*(3), 251-325. https://doi.org/10.1080/10643389.2010.507698

Wang, X., Zhao, Y., Tian, E., Li, J., & Ren, Y. (2018). Graphene Oxide-Based Polymeric Membranes for Water Treatment. *Advanced Materials Interfaces, 5*(15), 1701427. https://doi.org/https://doi.org/10.1002/admi.201701427

Wang, Y., & Weng, G. J. (2018). Electrical Conductivity of Carbon Nanotube- and Graphene-Based Nanocomposites. In S. A. Meguid & G. J. Weng (Eds.), *Micromechanics and Nanomechanics of Composite Solids* (pp. 123-156). Springer International Publishing. https://doi.org/10.1007/978-3-319-52794-9_4

Wang, Z., Yu, H., Xia, J., Zhang, F., Li, F., Xia, Y., & Li, Y. (2012). Novel GO-blended PVDF ultrafiltration membranes. *Desalination, 299*, 50-54. https://doi.org/https://doi.org/10.1016/j.desal.2012.05.015

Weres, O., Yee, A., & Tsao, L. (1981). Kinetics of silica polymerization. *Journal of Colloid and Interface Science, 84*(2), 379-402. https://doi.org/https://doi.org/10.1016/0021-9797(81)90230-7

WorldsteelAssociation. (2020). Water management in the steel industry.

Wu, H., Tang, B., & Wu, P. (2010). Novel ultrafiltration membranes prepared from a multi-walled carbon nanotubes/polymer composite. *Journal of membrane science, 362*(1), 374-383. https://doi.org/https://doi.org/10.1016/j.memsci.2010.06.064

Xu, Z., Zhang, J., Shan, M., Li, Y., Li, B., Niu, J., Zhou, B., & Qian, X. (2014). Organosilane-functionalized graphene oxide for enhanced antifouling and mechanical properties of polyvinylidene fluoride ultrafiltration membranes. *Journal of membrane science, 458*, 1-13. https://doi.org/https://doi.org/10.1016/j.memsci.2014.01.050

Yokoyama, T., Nakazato, T., & Tarutani, T. (1980). Polymerization of Silicic Acid Adsorbed on Iron(III) Hydroxide. *Bulletin of the Chemical Society of Japan, 53*(4), 850-853. https://doi.org/10.1246/bcsj.53.850

Zhang, J., & Buffle, J. (1995). Kinetics of Hematite Aggregation by Polyacrylic Acid: Importance of Charge Neutralization. *Journal of Colloid and Interface Science*, *174*(2), 500-509. https://doi.org/https://doi.org/10.1006/jcis.1995.1417

Zhang, J., Xu, Z., Mai, W., Min, C., Zhou, B., Shan, M., Li, Y., Yang, C., Wang, Z., & Qian, X. (2013). Improved hydrophilicity, permeability, antifouling and mechanical performance of PVDF composite ultrafiltration membranes tailored by oxidized low-dimensional carbon nanomaterials [10.1039/C2TA01415G]. *Journal of Materials Chemistry A*, *1*(9), 3101-3111. https://doi.org/10.1039/C2TA01415G

Zhang, R., Liu, Y., He, M., Su, Y., Zhao, X., Elimelech, M., & Jiang, Z. (2016). Antifouling membranes for sustainable water purification: strategies and mechanisms [10.1039/C5CS00579E]. *Chemical Society Reviews*, *45*(21), 5888-5924. https://doi.org/10.1039/C5CS00579E

Zhao, C., Xu, X., Chen, J., & Yang, F. (2013). Effect of graphene oxide concentration on the morphologies and antifouling properties of PVDF ultrafiltration membranes. *Journal of Environmental Chemical Engineering*, *1*(3), 349-354. https://doi.org/https://doi.org/10.1016/j.jece.2013.05.014

3. Removal of colloidal silica using aluminium, iron, titanium, and zirconium coagulants

3.1. Introduction

Removal of colloidal silica in clean water is a critical factor in lowering the running costs and increasing efficiency of a clean water treatment plant. Amorphous silica appears naturally in water either as a soluble (which includes monomers, dimers, and small chained polymers of silicic acid), or as colloidal silica (which are long polymeric chains of silicic acid). Typically, in natural waters the concentration of total silica ranges from 0 to 20 mg SiO_2/L, in which a portion of it is colloidal (Ning, 2010). Various treatment methods can be used to remove the total silica load such as lime softening, anion exchange resins, membrane filtration etc. Of these methods, the most practical and widely used is chemical coagulation as a pre-treatment which is typically followed by a filtration process. Coagulation plays a vital role in the removal of colloids, organic and inorganic matter. Chemicals such as iron and aluminium salts are widely used in industry, most typically, ferric chloride or alum, with the combination of polymer as a flocculant aid. However, there are some issues that need to be addressed in the application of Al/Fe coagulants, such as small floc size and long sedimentation times, issues with colour and odour of the effluent caused by iron coagulants and harmful residual species of aluminium leading to health problems in humans (Gan et al., 2020). Studies have showed that aluminium salts alone could not reduce the levels of silica concentration and that the addition of soda ash only slightly improved the process (Sheikholeslami & Tan, 1999). Other studies have shown that the removal of colloidal silica by aluminium salts was greatly dependent on the pH of the solution (Chuang et al., 2007). New coagulants with titanium and zirconium salts are emerging in the field of water treatment. Studies have reported that Ti salts used in wastewater have shown a high flocculation and turbidity removal and that zirconia have shown a strong floc formation property (Okour & Ahemd, 2018; Priya et al., 2017).

Currently there is no data on the removal efficiency of colloidal silica by these new and emerging coagulants. Thus, this study was conducted to compare

traditional coagulants (ferric and alum) to novel coagulants (titania and zirconia) for silica removal in water. This study evaluated the effect of pH and coagulant dosages on zeta potential and the characteristics of the flocs formed, and conducted a cost analysis of the various coagulants used to reduce colloidal silica by >95% from 25 mg/L to 1 mg/L .

3.2. Experimental procedures
3.2.1. Colloidal silica
Stock solutions of colloidal silica were prepared from a commercial solution (LUDOX-TM 50) purchased from Sigma-Aldrich UK. The LUDOX-TM 50 is an aqueous dispersion of silica particles with intermediate particle size and narrow particle size distribution. The solution is a 50 wt.% suspension in water with counterion sodium. The aqueous dispersion is kept at a pH of 9 and has a density of 1.4 g/mL at 25 °C.

For the preparation of stock solutions, 2 Litre volumetric flasks were used by adding the required amount of LUDOX-TM 50 solution to the volumetric flask followed by diluting with Milli-Q ultrapure water. All flasks were pre-treated by washing, drying in an oven for one hour at 120 °C, and after cooling at room temperature, they were ready for use.

3.2.2. Reagents
All reagents or chemicals were of analytical grade supplied by either Sigma Aldrich UK or Fisher Scientific UK. High quality DI water supplied by a Milli-Q system (UV Synergy system, with a MPK01 vent filter) was used throughout the study. Glassware were washed with 4% solution of Decon 90, rinsed with Milli-Q water and dried in oven for one hour at 120 °C. The anionic polymer FloPam AN910 (SNF, UK) was used as a flocculant aid. A stock solution at a concentration of 2g/L of flocculant was prepared by dissolving 1g of the polymer floc in 500mL of DI water. For pH adjustment, 0.2M HCl and NaOH were prepared using reagent grade sodium hydroxide (NaOH) and hydrochloric acid (HCl) (32%) supplied by Fisher Scientific, UK.

3.2.3. Source of Coagulants

Four different coagulant chemicals were used in this study: alum, ferric, titanium and zirconium. Alum based polymer in this study was obtained from aluminium sulphate octadecahydrate ($[(Al_2(SO_4)_3.18H_2O)]$) supplied by Sigma-Aldrich. The alum was prepared in high purity Milli-Q water (de-ionised water, 18 mΩ), at a concentration of 2 g/L (0.2 wt/vol %), in a 1L volumetric flask. The preparation involved agitating the solution by a magnetic stirrer to ensure the mixture was fully dissolved.

Ferric was obtained from Iron(III) chloride whereas zirconium was from zirconyl chloride octahydrate ($ZrOCl_2.8H_2O$), both provided by Sigma-Aldrich. Like the alum, the ferric and zirconium solutions were prepared in high purity Milli-Q water (de-ionised water, 18 mΩ), at 2 g/L (0.2 wt/vol %) in a 1L volumetric flask, followed by agitation of the solution by a magnetic stirrer to ensure the chemicals were fully dissolved.

Titanium was acquired from a ~15 wt. % titanium (IV) oxysulfate ($TiOSO_4$) stock solution in dilute sulfuric acid (Sigma-Aldrich, UK). The working solution was prepared in high purity Milli-Q water (de-ionised water, 18 mΩ) at 2 g/L (0.2 wt/vol %) by diluting the titanium stock solution to the required concentration in a 1L volumetric flask.

3.2.4. Steel works water sample

Real water samples were collected from the inlet of the clarifiers, before any chemical addition, from Tata Steel Port Talbot Margam C water treatment plant, which uses the river Afan as its water source. The water was collected in the winter season of November 2022 and January 2023 where water temperature was 6-12 °C. Prior to collecting the samples, the valve was opened and allowed to drain for 30 seconds to remove any stagnant liquid in the sampling pipe. The collected samples were used on the same day of collection.

3.2.5. Analysis of water samples

Different analytical techniques were used to characterise the water before and after treatment including silica and residual metal concentrations, Total Organic

Carbon (TOC), turbidity, pH, UV_{254}, zeta potentials, and floc size distribution. The methods used for these are discussed next.

3.2.5.1. MP-AES

The analysis of total silica (SiO_2) was performed by microwave plasma atomic emission spectrometer (4200 MP-AES) (Agilent technologies, UK) equipped with a standard torch. For plasma gas production, an Agilent 4107 nitrogen generator was used. The working pressure of the nitrogen generator was 5 bar. The silica concentration was analysed at a wavelength of 251.611 nm, with a stabilisation time of 15 seconds and 3 number of replicates, as suggested by Renata et al (Amais et al., 2013). Prior to measurement, the instrument was calibrated using a silica standard solution, 50 mg/L as SiO_2 (HACH, UK). The silica standard solution was diluted with DI water to produce five solutions (50, 40, 30, 20 and 10 mg/L).

The MP-AES was also used to measure the residual metal coagulant left in the water (aluminium, iron, titanium, and zirconium). The concentrations of aluminium, iron, titanium, and zirconium were analysed at the wavelengths of 396.152, 259.204, 334.941 and 343.8923 nm, respectively, with a stabilisation time of 15 seconds and 3 number of replicates. The MP-AES was calibrated using an ICP universal multi element standard provided by Agilent, UK.

3.2.5.2. HACH DR 2400

Analysis of the Total Organic Carbon (TOC) for the raw and treated river water completed by the HACH Method 10129. The method was conducted by the HACH DR/2400 model spectrophotometer. The method is based on the heated-persulfate oxidation of organic carbon to carbon dioxide as in the Standard Methods for the Examination of Water and Wastewater (APHA, 2017). The first step was to switch on the Hach 45600 COD reactor set to 103-105 °C inside a fume hood. 10 mL of the sample was mixed with a 0.4 mL of buffer solution at pH 2. It is important to note that HCl must not be used to acidify the samples as chloride interferes with the persulfate oxidation. The mixture was then mixed with a magnetic stirrer at a moderate speed for up to 10 minutes. Low range acid digestion vials were prepared by funnelling TOC persulfate powder pillow to each

vial. 3 mL of the sample with buffer solution was pipetted to the prepared vials, while one vial was only filled with 3 mL organic free deionised water. The deionised water was used straight away ensuring minimal CO_2 absorption. The vials were mixed thoroughly. Blue indicator ampules were cleaned with deionised water and wiped with a lint free wipe. They were then lowered into the vials up until the score mare on the ampule, which was then snapped off allowing the content to drop into the vial. The capped vials were then placed in the pre heated COD reactor for 2 hours. The vials were then removed and placed on a test tube rack to cool down, once cooled, the reagent blank was used to calibrate and zero the HACH DR/2400. Sample vials were then measured and the results are displayed in mg/L C.

3.2.5.3. Turbidity

The turbidity measurement was carried out on a Hach 2100AN laboratory turbidimeter, with a glass sample cell for lab turbidimeters and 10 NTU standard solution for calibration. 30 mL of the sample was placed in the glass cell, shaken up, and placed in the turbidimeter. The sample was then measured, and the results were given in nephelometric turbidity unit (NTU).

3.2.5.4. pH

Sample pH was measured using an Orion Star A211 pH meter (Thermo Scientific, UK). The pH electrode was washed with distilled water, before being dried with a soft paper towel and placed into a pH buffer solution for calibration. The pH probe was calibrated using solutions of pH 4, 7 and 10, provided by Fisher Scientific, UK.

3.2.5.5. UV-Vis

UV Vis absorption for samples was carried out by an HP 8453 Ultra-Violet spectrophotometer (Agilent Technologies UK), measuring the absorbance at 254 nm for the raw water samples.

3.2.5.6. Zeta potential and floc size distribution

Floc size distribution and zeta potential was measured by the ZetaSizer Nano (Malvern instruments, UK). For zeta potential measurements, glass cuvettes were filled with the sample in which a universal 'dip' cell was placed, so that the

palladium electrodes were in contact. Samples were set to run between 10-100 times, in which 3 measurements were taken.

For floc size distribution measurements, 1cm pathlength quartz cuvette was loaded with the sample, which was then analysed using dynamic light scattering (DLS). The method was set that the sample refractive index was 1.46 (Fröhlich et al., 2016). The measurement was carried out at a 173° backscatter angle, with 120s settling time, 10 runs per sample with 3 recorded measurements (average taken).

3.2.5.7. Jar Test

The coagulation/flocculation studies were conducted using a bench-scale jar test unit with a six-paddle mixer (W1 flocculation test unit). In 500-mL beakers, 400 mL colloidal silica solutions were placed and mixed at rapid mixing speed of 150 rpm for 1 minute followed by 15 minutes slow mixing at 30 rpm. At the end of the flocculation period the solution was allowed to settle for 1 hour. All experiments were conducted at room temperature of 20±1°C. At Tata Steel Port Talbot, an aluminium based inorganic coagulant followed by a polymer flocculant aid. To recreate this process, a polymer solution was used to aid flocculation. The anionic polymer Flopam AN910 was used at an optimum dosage of 2.5 mg/L (MWH, 2012; Swift et al., 2015). Once settled, the supernatant was collected with a syringe from about 2 cm below the water surface, before being analysed. The pH of the solution was set to the desired value after addition of the coagulant to account for any pH drop due to hydrolysis of the coagulant. Small adjustments were made during the jar test experiment period if the pH was outside the range of ±0.2 of the desired pH value. The effects of both pH and coagulant dosage were studied in the ranges 2 to 10 and 2.5 to 30 mg/L, respectively. The removal efficiencies of silica, TOC, turbidity, and UV_{254} were calculated using the following equation:

$$Removal\ (\%) = \left[\frac{(C_i - C_f)}{C_i}\right] \times 100 \qquad (3.1)$$

Where, C_i and C_f are the initial and final values of the analysed parameter.

3.3. Results and Discussions

3.3.1. Effect of coagulant dosage on the zeta potential, floc size and removal of colloidal silica

The effect of dosage of each coagulant on the zeta potential, floc size and removal of colloidal silica was studied. Dosages ranged from 2.5 to 30 mg/L (as titanium oxysulfate, zirconyl chloride octahydrate, ferric chloride and aluminium sulphate octadecahydrate) were used for solutions of colloidal silica in DI water at a concentration of ~ 35 mg SiO_2/L. Figure 3.1 (a & b) shows the effects of the different coagulants and their dosages on zeta potential and floc sizes, respectively, with no pH adjustment. According to these figures, the coagulant dosage has a significant effect on both the zeta potential and floc size of the colloidal silica. For all coagulants, a progressive increase in dosage resulted in a corresponding rise in zeta potential, which continued until a threshold charge was achieved, beyond which the zeta potential plateaued. The increase in zeta potential is consistent with the positive charge of the coagulants. The dosages required to reach the point of isoelectric point (IEP) for the coagulants can be found in Figure 3.2. These results show that zirconium required the least quantity to reach the IEP, at 0.30 mg Zr/L. While titanium required the largest dose of 1.5 mg Ti/L to reach the PZC. This could be due to the highly charged cationic hydrolysis species produced when zirconium is dissolved in water, some authors have proposed the formation of $[Zr_3(OH)_3]^{8+}$ others have suggested $[Zr_4(OH)(OH_2)_7]^{3+}$ and a cyclical tetramer of $[Zr_4(OH)_8(OH_2)_{16}^{8+}]$, the extent and nature of hydrolysis depend on the pH of solution (Rose et al., 2003). Ferric and alum required intermediary dosages of 0.84 mg Fe/L and 0.4 mg Al/L, respectively, to reach the IEP. Other studies have also supported the higher

dosages required for titanium coagulants to reach the PZC compared to ferric and aluminium based coagulants (Zhao et al., 2011; Zhao et al., 2014)
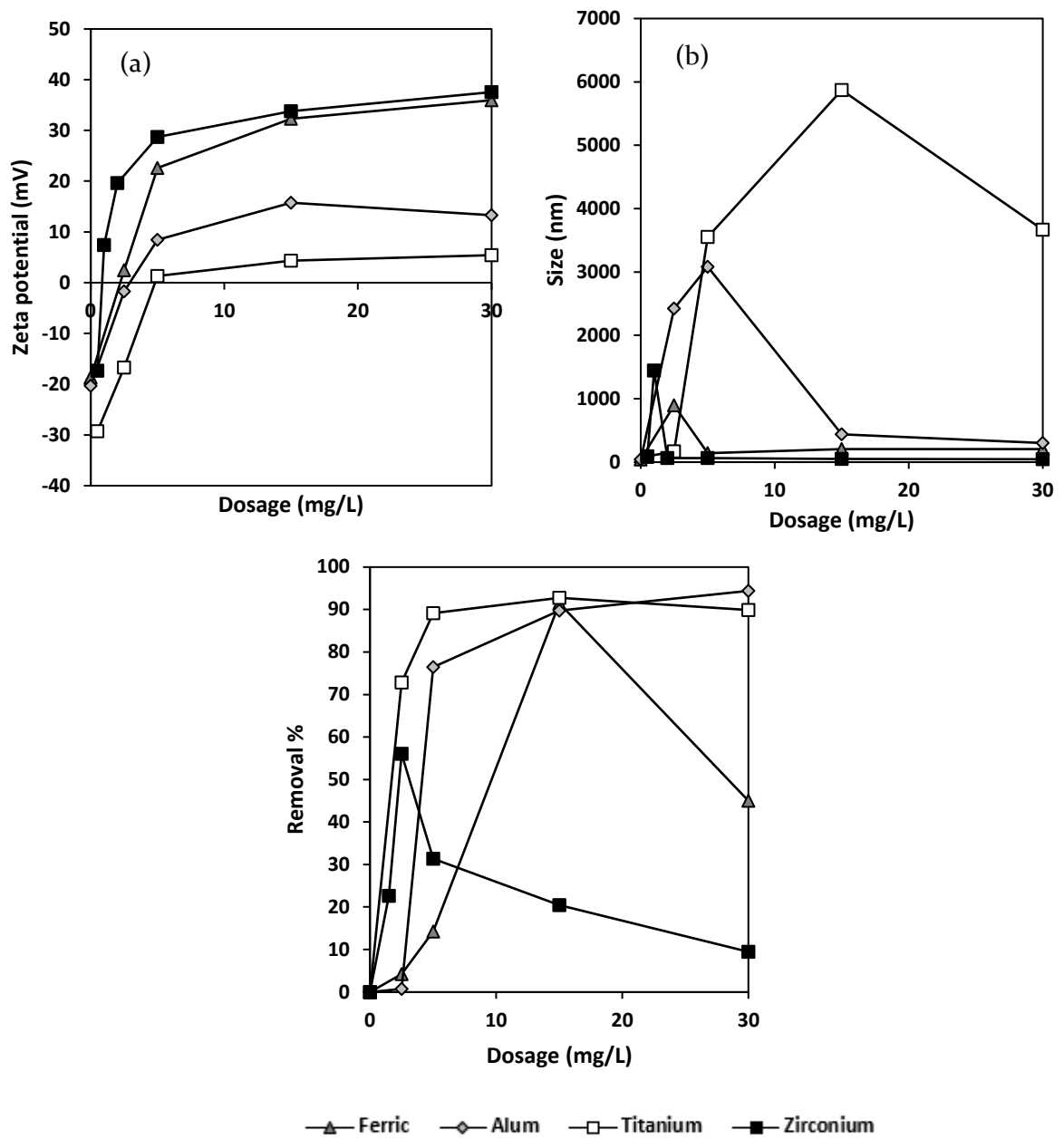
Figure 3.1. Effect of coagulant dosage on zeta potential (a), floc size (b) and removal efficiency of colloidal silica (pH=7.8)
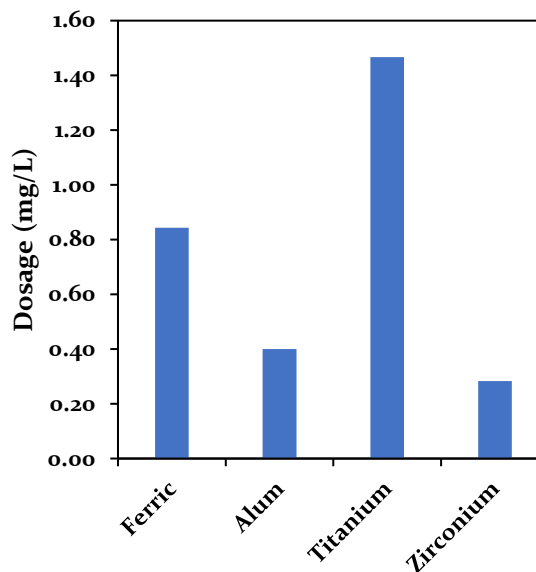
Figure 3.2. Dosage required to reach the point of zero charge for each coagulant

According to Figure 3.1 (b), the floc size increased initially until reaching a maximum after which it dropped to values close to zero for all coagulants except titanium. This could be due to re-stabilisation of the particle and reverse charge, in which particle charges change from negative to positive allowing the particles to repel again. This coincides with the zeta potential measurements where at dosages around the IEP, the size of the particles is the largest and it drops significantly at higher dosages, due to the positive charged particles. When overdosed, alum and titanium gave zeta potential values that remained relatively low compared to the other two coagulants. This is reflected in the size of the flocs in Figure 3.1 (b), which showed that alum and titanium had larger sized particles over the range of dosages, whereas ferric and zirconium floc sizes drastically decreased at doses above 5 mg/L and 2.5 mg/L, respectively. Titanium had the largest floc size of above 5000 nm, which was almost double when compared to alum (3079 nm) and zirconium (3000 nm). Zirconium had a larger floc size compared to ferric, however once its dosage increased only slightly, the sizes dropped off sharply, which indicates that the dosage optimisation window for zirconium is very narrow. The dosage window for iron is only slightly better than zirconium but significantly narrower than Al and Ti. During the experiment, it

was observed that flocs produced by titanium alone were large and dense enough to settle quickly without the aid of a polymer flocculant. This was not observed with the other coagulants until the polyelectrolyte was added. This could be due to bridging effect, which can be caused by highly polymerised Ti hydrolysates which act as a bridge to connect pollutants through chemical bonds, effectively creating larger and denser flocs (Gan et al., 2020). Additionally, titanium coagulants often form insoluble hydroxides, such as $Ti(OH)_4$, which precipitate out of solution and sweep suspended particles (Xu et al., 2023).

Figure 3.1 (c) shows the removal efficiency when the coagulant dosage was adjusted. The optimum dosage for ferric and alum was 15 mg/L (5.2 mg Fe/L and 2.4 mg Al/L), for titanium it was between 5 and 15 mg/L (1.5-4.5 mg Ti/L), and for zirconium was 2.5 mg/L (0.71 mg Zr/L). Both titanium and alum had the best removal efficiencies and maintained the efficiency at high dosages. The efficiency of ferric, however, dropped significantly once the dosage was increased to 30 mg/L (10.2 mg Fe/L) and that of zirconium worsened as the dosage increased above 2.5 mg/L (0.71 mg Zr/L). Studies by Kim et al. found that colloidal silica removal was better near the isoelectric point (IEP), thus proper destabilization of particles is very important to achieve better floc removal. It was also found that the mean zeta potential of silica particles at a given coagulant dosage was a function of particle concentration, thus optimisation will be dependent on the silica concentration of the solution (Kim & Lawler, 2005).

Similar patterns are seen in the relationship between dosage and removal efficiencies of contaminants in water, where studies by Kuzin et al showed that the efficiency of removal drops when coagulants (aluminium sulphate, poly aluminium chloride, titanium chloride, titanium oxy sulphate and ferric chloride) are overdosed when removing various solids in alcohol industrial waste waters. However, the dosages used in this study were comparatively higher to the doses used in this the study by Kuzin et al. (2022).

3.3.2. Effect of pH on the zeta potential, floc size and removal of colloidal silica

One of the most important parameters in coagulation is the pH of the solution, as it influences the coagulation mechanism and its effectiveness. Figure 3.3 (a-c) shows the effect of pH on zeta potential, floc size, and removal efficiency when dosages were kept constant at 5 mg/L of coagulant. Ferric had isoelectric point (IEP) at around pH of 5.8, titanium at pH 4.2 , alum at pH 4 and zirconium at pH 6.6, respectively. These results agree with those reported in previous studies who studied titanium, however, the IEP of ferric was found to be pH 7, the difference could be due to preparation methods, ionic strengths, or presence of other ions and organic matter in the solution (Wang et al., 2018; Wu et al., 2011). Figure 3.3 (b) shows the effect of pH on floc size. Zirconium gave the smallest particle size compared to the other coagulants at all pHs; the largest size that could be achieved by zirconium was 429 nm at pH 4. Ferric and alum gave similar sizes of 2000 and 2400 nm, at pH of about 4.5, respectively. Interestingly, titanium gave the largest floc size, more than twice larger than alum and ferric. The largest floc size for titanium was around 6500 nm at a pH of 6.3. It was observed that the particles formed with titanium were large enough to settle without the aid of a flocculant. The titanium coagulant also provided large flocs over a larger range of pH, from pHs of approximately 3 to 8, compared to the other coagulants. Literature from species-pH distribution shows that the hydrolysis of titanium begins at much lower pHs compared to alum (Gan et al., 2020). Figures 3.4 (a) and (b) show the speciation of aluminium and titanium. Figure 3.4 (a) shows at pH below 4 aluminium exists as Al^{3+}, as pH increases to 4-5.5, hydrolysed species like $[Al(OH)]^{2+}$ and $[Al(OH)_2)^+$ become more significant. Figure 3.4 (b) show at pH below 2 Ti exists mainly as TiO^{2+} and as pH increases to 2-4 hydrolysed species like $TiO(OH)^+$ and $TiO(OH)_2$ exists prevail (Gan et al., 2020; Lekhlif et al., 2014).
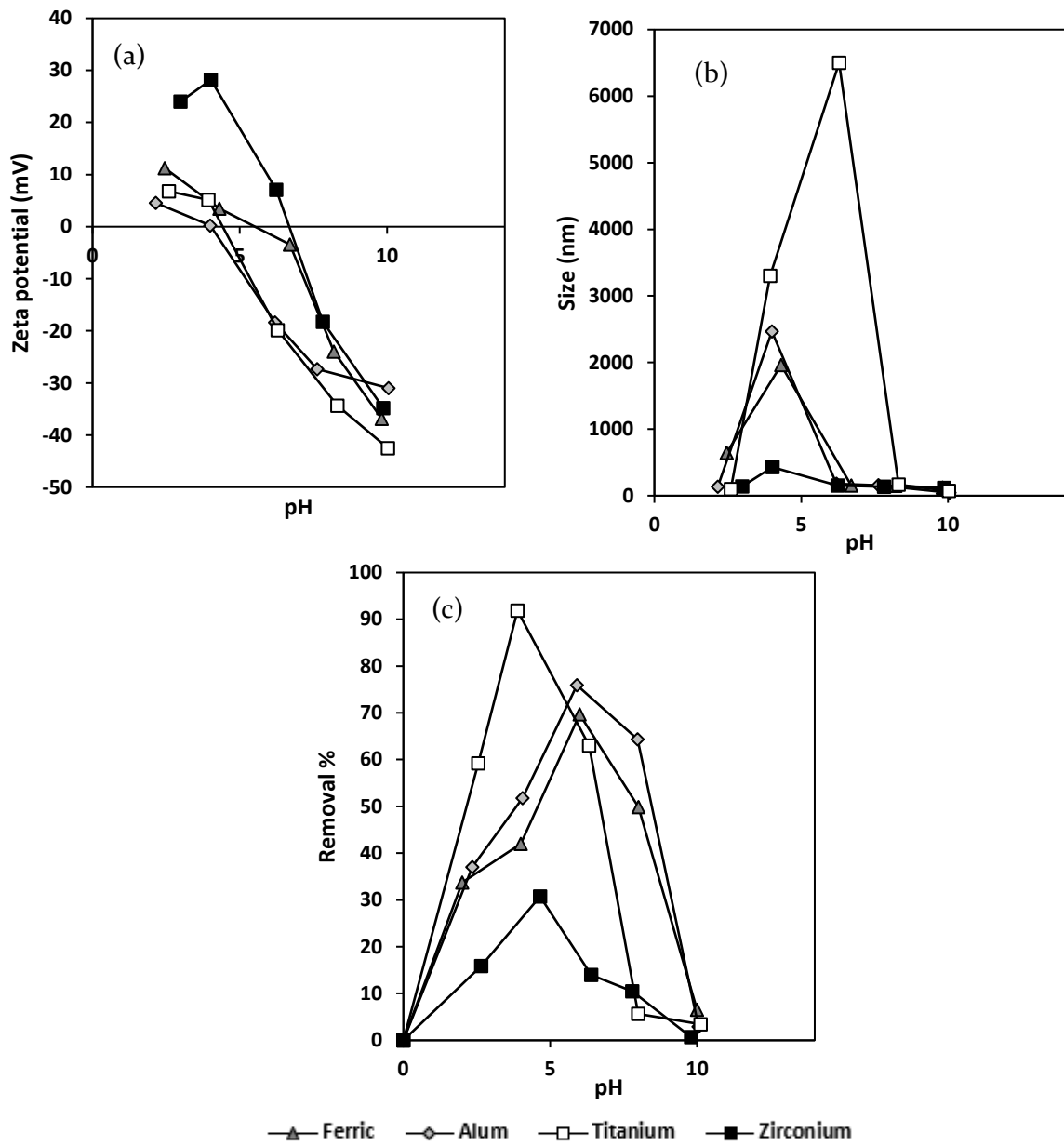
*Figure 3.3. Effect of pH on zeta potential (a), floc size (b) and removal efficiency of colloidal silica*

Figure 3.3 (c) shows the removal efficiencies of colloidal silica when the solution pH was adjusted. The ranges of pH values within which the coagulants achieved at least 50% removal were determined. Figure 3.3 (c), results showed that for ferric and alum, this pH range was almost similar of about 4 to 8, whereas titanium had a slightly wider acidic pH range of about 2 to 7. Zirconium was not capable to achieve 50% silica removal; the best removal achieved by zirconium was 30% at pH 4.5.
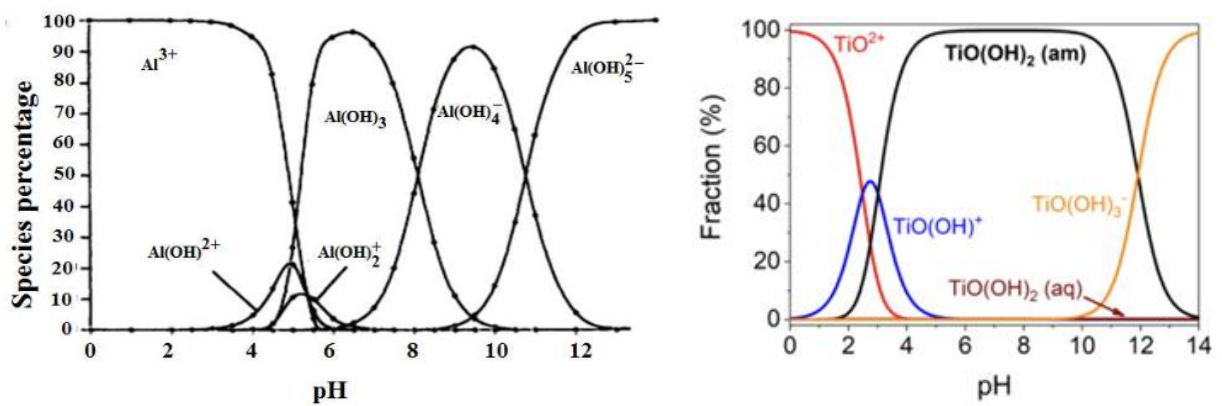
Figure 3.4. Species percentage at varying pH of aluminium (Lekhlif, B., Oudrhiri, L., Zidane, F., Drogui, P., & Blais, J.-F. (2014)) and titanium (Dong, Y., Zhang, P., & Lin, H. (2022))

The performance of traditional salt coagulants is greatly influenced by the solution pH because of pH effects on coagulation mechanisms and contaminant speciation. During coagulation, contaminants are removed by charge neutralization, bridging effects, sweep flocculation and sorption onto newly formed metal hydroxides, from the hydrolysis products of the metal coagulants (Al, Fe, Ti and Zr). Studies have shown that the formation and solubility of these hydroxides are strongly linked to the pH of the solution. Additionally, the surface complexes formed between the metal and colloidal silica is strong and not easily reversed except at high pH when excess hydroxide ions are present, thus they compete with the silica particles. As a result, there is a decrease in the fraction of positively charged adsorption sites on the metal hydroxide surface (Lakshmanan et al., 2008). Studies by Wang et al have shown that ferric as a coagulant used to remove arsenic had the largest particle size at pH 6-7 (Wang et al., 2014) . Studies have shown that a similar pattern is seen in the relationship between zeta

potential and the pH of solution which shows that zeta potential decreases at higher pH, including alum, ferric, titanium and zirconium (Hussain et al., 2014; Lester-Card et al., 2023; Wang et al., 2014).

3.3.3. Steel works surface water - Spiked and un-spiked samples and raw water

Surface water from the Afan river, which is used for the feed in Tata steel Port Talbot water treatment plant was sampled (November 2022); Table 3.1 summarises the characteristics. Both un-spiked and spiked experiments were used in this study. The spiked experiments used colloidal silica at concentrations similar to those used in previous experiments while the un-spiked experiments used the river water as received without further processing. , to discover the effect the coagulant has on raw water. For the spiked samples, 2L of the river water was spiked with 0.1 mL of approximately 50 w/v% of colloidal silica. The specific gravity of 50 w/v% colloidal silica is ~1.4 g/cm³, therefore the concentration is ~35 mg/L. The samples of the spiked/un-spiked and raw water were collected on different dates and thus there are slight variations in the compositions of the waters.

Table 3.1. Raw water characteristics of spiked and un-spiked water from the River Afan

Parameter	Spiked water sample	Un-spiked water sample
Total Silica (mg/L)	38.9	5.75
Colloidal Silica (mg/L)	33.15	0.63
TOC (mg/L)	4.5	4.5
Turbidity (NTU)	5.38	5.38
UV_{254}	0.1685	0.1685
Aluminium (mg/L)	0.49	0.49
Iron (mg/L)	0.19	0.19
Titanium (mg/L)	0.0	0.0

3.3.3.1. Spiked sample results

The effects of coagulant dosages and initial pH on the coagulation performance of alum, ferric, titanium, titanium with no polyelectrolyte and zirconium were

studied. Figure 4 shows the removal efficiency obtained by each coagulant. The optimum coagulation conditions were selected based on the previous experiments (Table 3.2).

According to Fig 3.5 alum, titanium, and titanium (with no polymer) showed the best removal efficiencies for the four parameters studied. They all had similar removal efficiencies for silica (~80%) and UV_{254} (~95%). However, titanium (with and without polymer) had higher removal efficiencies of TOC and turbidity than alum. Comparing titanium with and without polymer, it appears that titanium without the polymer performs slightly better, which suggests that the titanium coagulant can be used without the need for polymer addition to aid flocculation. These results also confirmed that titanium achieved slightly better removal of organics compared to alum, which agrees with literature (Zhao et al., 2011).

As illustrated in Fig 3.5, zirconium showed a poor performance in silica removal, which agrees with the results previously discussed when DI water was used. Ferric also exhibited a poor silica removal performance compared to previous experiments, which could be due to interference from other contaminants in the water. The effect of such interference could be compensated by increasing the coagulant dosage (Achite et al., 2024; Haghiri et al., 2018; Nti et al., 2021). For both zirconium and ferric, the removal efficiencies of silica, TOC, turbidity and UV_{254} were all less than 30%, with silica being particularly poor.

According to Fig 3.5, colloidal silica removal efficiency had decreased by ~10-20% for alum and titanium, and ~50% for ferric and zirconium when compared to the previous experiments when DI water was used (Fig 3). Higher dosages are likely to be required due to additional contaminants found in the river water, especially with seasonal changes as seen in the spiked/un-spiked and raw water sample that was taken 3 months apart, shows TOC had increased by more than 2 times. Water in the River Afan is relatively clean compared to rivers from urban surroundings and even with the increased TOC was still in the lower range of organics typically found in rivers (Worrall et al., 2004).

Table 3.2. Conditions set for dosage and pH for spiked samples

Coagulant	Dosage (mg/L)	pH	Polyelectrolyte dose (mg/L)
Alum	30	5.85	1.0
Ferric	15	5.95	1.0
Titanium	15	3.78	1.0
Zirconium	2.5	6.11	1.0
Titanium (no polyelectrolyte)	15	3.89	0
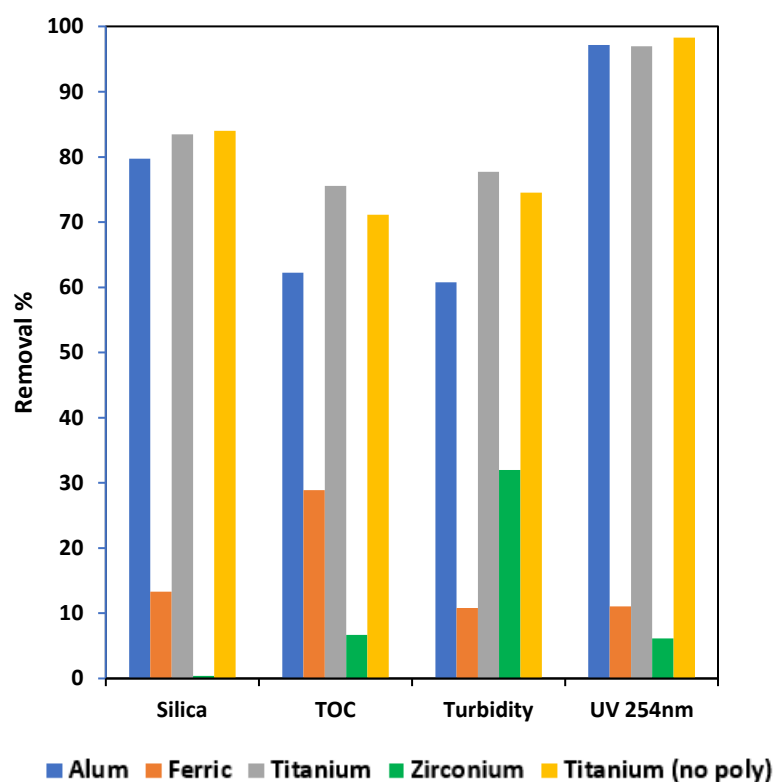
Figure 3.5. Colloidal silica removal efficiency of alum, ferric, titanium, zirconium, and titanium (no polyelectrolyte)

3.3.3.2. Un-spiked samples

Optimisation of dosage for the coagulation performance of alum, ferric, titanium and titanium (no polyelectrolyte) were conducted on un-spiked raw surface water. Zirconium was not used in these tests due to its poor performance as shown in previous tests with DI water and spiked river water. The same water parameters as in previous experiments, including silica concentration, turbidity, TOC, and UV_{254}, were measured, and the results are shown in Fig 3.6. The coagulant dosages were in the range 1 to 40 mg/L and the pHs used were as previous experiments (Table 3.3).
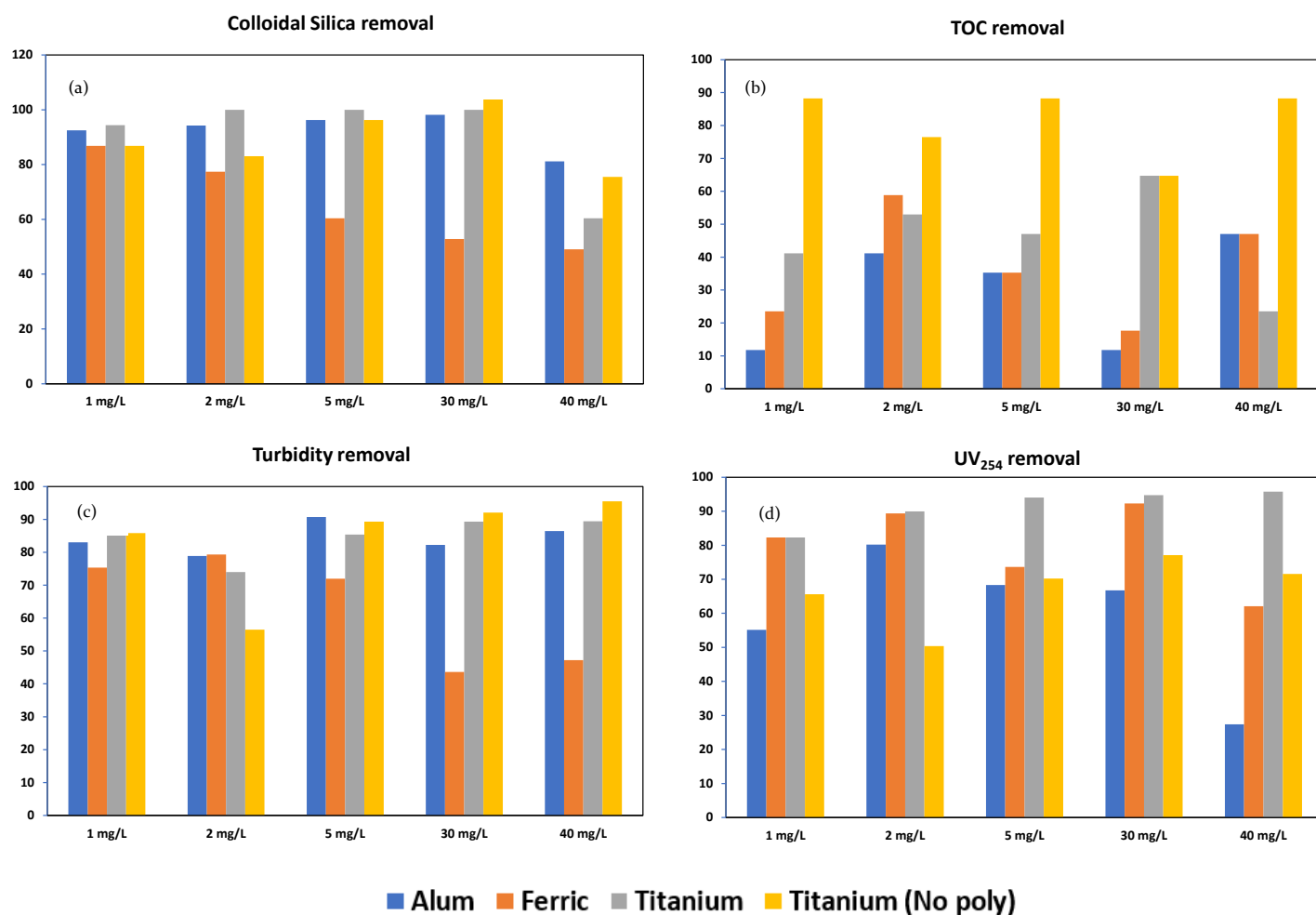
Figure 3.6. Removal efficiencies of colloidal silica, turbidity, TOC and UV_{254} with varying dosages of coagulant dosage for raw un-spiked water from the river Afan (pH found in Table 3.2)

The highest colloidal silica removal efficiency in real un-spiked river water was 100% achieved using titanium coagulant at a dose of only 2 mg/L when the polymer flocculant was used and at a dose of 30 mg/L when the polymer was not used. Alum also showed high silica removal (98%) but at a dose of 30 mg/L in the presence of the polymer. It was also observed that titanium achieved more than 100% removal of colloidal silica (data is not shown), which suggests that it removed dissolved silica in addition. At dosages of 40 mg/L, the removal efficiency dropped by more than 15% for all coagulants. Ferric at 1 mg/L showed its best silica removal of 86%, but as its dose increased, the removal efficiencies dropped continuously. This again correlates well with the previous experiments, that when ferric was overdosed the removal of colloidal silica also decreased (Figure 3.1 (c)). Titanium (no polymer) was able to perform as good or even better as alum within the dosage range of 1 to 40 mg/L.

Turbidity had the highest removal of 95% with titanium (no polyelectrolyte) at 40 mg/L, however, both alum and titanium also had high turbidity removal of 90% at dosages of 5-30 mg/L. Other studies have reported high turbidity removals of above 80% when using $TiCl_4$ compared to alum and ferric (Okour et al., 2009; Zhao et al., 2011). Ferric had a similar pattern seen in the previous results, in which, turbidity removal decreased at dosages above 30 mg/L.

Titanium (no polyelectrolyte) showed the best TOC removal compared to the rest of the coagulants, with the highest removal efficiency of 88% at 5 mg/L. Ferric was the next best performer which removed 60% of TOC at a dosage of 2 mg/L. Alum was the worst performing coagulant at removing TOC.

UV_{254} removal results showed that ferric and titanium had the best removal efficiency of 92 and 94% respectively, at a dosage of 30 mg/L. This correlates well with other studies which showed better removal of UV_{254} by titanium coagulants as compared to aluminium and iron counterparts (Zhao et al., 2013; Zhao et al., 2014). Alum removal efficiency of UV_{254} had significantly dropped at dosage of 40 mg/L.

Table 3.3. Optimum dosage and removals of Total silica, turbidity, TOC and UV254 for coagulants

Coagulant/parameter		Fe	Al	Ti	Ti (no polyelectrolyte)
pH		5.95	5.85	3.78	3.89
Total Colloidal Silica	Max. removal (%)	86	98	100	100
	Dose (mg/L)	1	15	2	30
Turbidity	Max. removal (%)	79.3	90.7	89.3	95.5
	Dose (mg/L)	2	5	30	40
TOC	Max. removal (%)	58.8	41.2	64.7	88.2
	Dose (mg/L)	2	2	30	5
UV_{254}	Max. removal (%)	89.4	80.2	94.0	77.2
	Dose (mg/L)	2	2	5	30

3.3.3.3. Sludge characterisation

Figure 3.7 shows the sludge from the jar tests which had been dried. It showed that alum and ferric had similar appearance, which were all dark brown with large

patches. Titanium samples were similar but slightly lighter brown. The sample titanium (no polymer), comparatively, had a much lighter and smaller patches of brown colour. This suggests that the flocculant aid was aggregating larger particles in the jar tests, however, there was no correlation with the removal efficiencies of the contaminants, as titanium (no polymer) was able to compete with the other coagulants.

When ferric salts such as ferric chloride are used as coagulants they react with water to form iron hydroxides, primarily ferric hydroxide ($(Fe(OH)_3$). These iron hydroxides are inherently brown/reddish, which imparts the brown colour to the resulting sludge. This can be seen in Figure 3.8 (a) which shows the jar test during slow mixing of ferric coagulant has a brown/reddish particles, compared to the other coagulants. Alum coagulants typically produce white/light grey aluminium hydroxides compared to ferric, which results in sludge generally having a lighter appearance. Titanium salts when hydrolysed by water produce titanium hydroxides, which can convert to titanium dioxide (TiO_2). Titanium dioxide is commonly used as a white pigment in various industries such as paints. Due to the presence of organics and subsequent oxidation, brown patches are observed with the titanium, however, the resulting sludge is much lighter compared to ferric and alum, as can be seen in Figures 3.7.
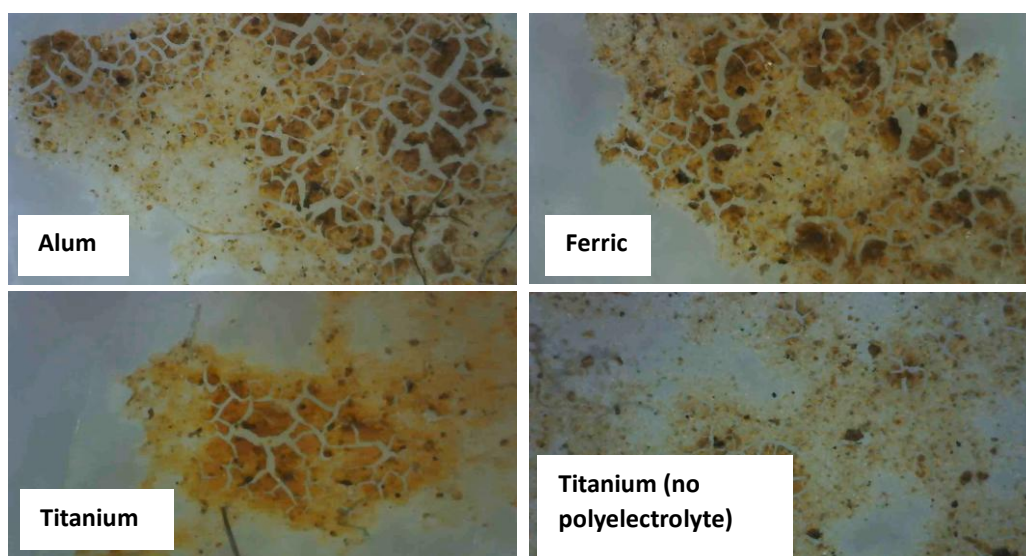
Figure 3.7. Dried sludge from the jar tests with alum, ferric, titanium and titanium (no polymer)
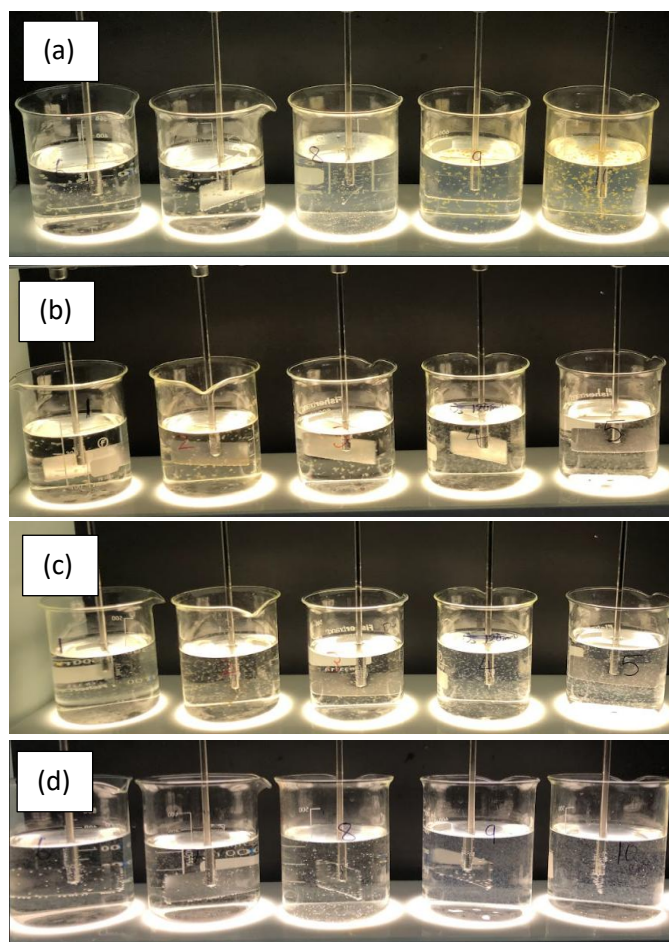
Figure 3.8. Slow mix stage of tests for (a) ferric, (b) alum, (c) titanium and (d) titanium (no polyelectrolyte)

3.3.4. Comparison of coagulant costs

The economic feasibility of using these salts and floc aids as coagulants/polyelectrolyte for silica removal was studied by comparing the costs (https://www.echemi.com/, 2023). Dosages optimised in Table 3.3 was chosen as it had the best colloidal silica removal efficiency for alum, titanium, and titanium (no polyelectrolyte), to treat 142 m³/hr of Afan river water (un-spiked). The cost calculation did not consider costs of sludge settlement and handling and process control.

The calculations revealed that ferric has the lowest chemical cost was the most cost-effective coagulant, costing $0.71 to treat 142 m3/hr of water. Alum was found to be 3-4 times more expensive as ferric, for silica removal, at $2.73. Both titanium cost slightly lower compared to alum due to the low dosages at $2.31. Titanium

with no polyelectrolyte, was noticeably cheaper compared to alum and titanium with polyelectrolyte, costing $1.68. Finally, zirconium, which was optimised in Table 3.2, was the most expensive out of all the coagulants costing, $8.68.

Overall, with the effectiveness of titanium at low dosages, as well as high removal rates with no poly electrolyte, make it a financially competitive coagulant compared to traditional coagulants such as alum and ferric.

3.4. Conclusions

The following conclusions are made based on this study of colloidal silica removal by common (ferric and alum) and novel (titanium and zirconium) coagulants:

- Floc size, zeta potential, and silica removal was highly dependent on the dosages of the coagulant. When overdosed it was found that titanium kept the largest particle sizes and removal efficiencies high and the zeta potential was also kept close to the PZC. This was followed by alum, ferric and lastly zirconium. The results also showed that in removing colloidal silica, the control of ferric and zirconium dosages was very difficult.
- Particle size, zeta potential, and silica removal was highly dependent on the pH of the solution with titanium and zirconium was most effective in the pH of range ~6-7 , whereas alum and ferric the in the pH of range was ~6, and finally titanium in the pH of ~4
- Results found that the titanium coagulant was able to produce large and dense enough particles that settle easily without the aid of a polymer flocculant.
- Spiked and un-spiked samples of raw surface water tests revealed that alum, titanium and titanium (no polymer) had the best removal rates of colloidal silica, turbidity and TOC. Ferric had the best removal of UV_{254}.
- Chemical costs, excluding sludge and control costs, were compared to treat 140 m3/h of river Afan water with ferric, alum, zirconium, titanium and titanium (no polyelectrolyte) to remove colloidal silica. The most

economical and lowest chemical cost was for ferric ($0.71). Alum was found to be 3-4 times more expensive compared to ferric ($2.73). Titanium costs were comparably lower to alum costs ($2.31) due to the lower dosages, with no polyelectrolyte costing even lower ($1.68). Zirconium was the most expensive ($8.6).This study suggests that pilot plant studies using titanium coagulant should be carried out to ascertain the potential of this coagulant in treating Afan raw water for boiler feed water at Tata Steel, Port Talbot site.

3.5. References

Achite, M., Farzin, S., Elshaboury, N., Valikhan Anaraki, M., Amamra, M., & Toubal, A. K. (2024). Modeling the optimal dosage of coagulants in water treatment plants using various machine learning models. *Environment, Development and Sustainability*, *26*(2), 3395-3421. https://doi.org/10.1007/s10668-022-02835-0

Amais, R. S., Donati, G. L., Schiavo, D., & Nóbrega, J. A. (2013). A simple dilute-and-shoot procedure for Si determination in diesel and biodiesel by microwave-induced plasma optical emission spectrometry. *Microchemical Journal*, *106*, 318-322. https://doi.org/https://doi.org/10.1016/j.microc.2012.09.001

APHA. (2017). 5310 TOTAL ORGANIC CARBON. In *Standard Methods For the Examination of Water and Wastewater*. American Public Health Association. https://doi.org/doi:10.2105/SMWW.2882.104

10.2105/SMWW.2882.104

Lekhlif, B., Oudrhiri, L., Zidane, F., Drogui, P., & Blais, J.-F. (2014).

Study of the electrocoagulation of electroplating industry wastewaters charged by nickel (II) and chromium (VI). *Journal of Materials and Environmental Science*, *5*, 111-120.

Chuang, S. H., Chang, T. C., Ouyang, C. F., & Leu, J. M. (2007). Colloidal silica removal in coagulation processes for wastewater reuse in a high-tech industrial park. *Water science and technology : a journal of the International Association on Water Pollution Research*, *55*, 187-195. https://doi.org/10.2166/wst.2007.054

Fröhlich, K. A., Mitrentsis, E., Clemens, F., Hoffmann, B., Michaud, V., & Graule, T. (2016). Assessment of the Dispersion Quality of Refractive Index-Matched Nanodispersions. *26*(6), 33-42. https://doi.org/doi:10.3933/applrheol-26-65050 (Applied Rheology)

Gan, Y., Jingbiao, L., Li, Z., Wu, B., Wenguang, H., Li, H., & Zhang, S. (2020). Potential of titanium coagulants for water and wastewater treatment:

Current status and future perspectives. *Chemical Engineering Journal, 406*. https://doi.org/10.1016/j.cej.2020.126837

Haghiri, S., Daghighi, A., & Moharramzadeh, S. (2018). Optimum coagulant forecasting by modeling jar test experiments using ANNs. *Drinking Water Engineering and Science, 11*(1), 1-8.

https://www.echemi.com/. (2023). https://www.echemi.com/. Retrieved 12/04/2023 from

Hussain, S., van Leeuwen, J., Chow, C. W. K., Aryal, R., Beecham, S., Duan, J., & Drikas, M. (2014). Comparison of the coagulation performance of tetravalent titanium and zirconium salts with alum. *Chemical Engineering Journal, 254,* 635-646. https://doi.org/https://doi.org/10.1016/j.cej.2014.06.014

Kim, J.-K., & Lawler, D. (2005). Characteristics of Zeta Potential Distribution in Silica Particles. *Bulletin of the Korean Chemical Society, 26.* https://doi.org/10.5012/bkcs.2005.26.7.1083

Kuzin, E., Averina, Y., Kurbatov, A., Kruchinina, N., & Boldyrev, V. (2022). Titanium-Containing Coagulants in Wastewater Treatment Processes in the Alcohol Industry. *Processes, 10*(3).

Lakshmanan, D., Clifford, D., & Samanta, G. (2008). Arsenic Removal by Coagulation With Aluminum, Iron, Titanium, and Zirconium. *Journal American Water Works Association - J AMER WATER WORK ASSN, 100,* 76-88. https://doi.org/10.1002/j.1551-8833.2008.tb08144.x

Lekhlif, B., Oudrhiri, L., Zidane, F., Drogui, P., & Blais, J.-F. (2014). Study of the electrocoagulation of electroplating industry wastewaters charged by nickel (II) and chromium (VI). *Journal of Materials and Environmental Science, 5,* 111-120.

Lester-Card, E., Smith, G., Lloyd, G., & Tizaoui, C. (2023). A green approach for the treatment of oily steelworks wastewater using natural coagulant of Moringa oleifera seed. *Bioresource Technology Reports, 22,* 101393. https://doi.org/https://doi.org/10.1016/j.biteb.2023.101393

MWH. (2012). Coagulation and Flocculation. In *MWH's Water Treatment: Principles and Design, Third Edition* (pp. 541-639). https://doi.org/https://doi.org/10.1002/9781118131473.ch9

Ning, R. Y. (2010). Reactive silica in natural waters — A review. *Desalination and Water Treatment, 21*(1-3), 79-86. https://doi.org/10.5004/dwt.2010.1229

Nti, S. O., Buamah, R., & Atebiya, J. (2021). Polyaluminium chloride dosing effects on coagulation performance: case study, Barekese, Ghana. *Water Practice and Technology, 16*(4), 1215-1223. https://doi.org/10.2166/wpt.2021.069

Okour, Y., & Ahemd, D. S. (2018). An effective method of wastewater treatment using titanium salt and a coagulant aid of chitosan. *Water and Environment Journal, 33.* https://doi.org/10.1111/wej.12414

Okour, Y., El Saliby, I., Shon, H. K., Vigneswaran, S., Kim, J. H., Cho, J., & Kim, I. S. (2009). Recovery of sludge produced from Ti-salt flocculation as pretreatment to seawater reverse osmosis. *Desalination, 247*(1), 53-63. https://doi.org/https://doi.org/10.1016/j.desal.2008.12.012

Priya, T., Mohanta, V. L., & Mishra, B. K. (2017). Performance evaluation of zirconium oxychloride for reduction of hydrophobic fractions of natural organic matter. *Separation and Purification Technology, 174,* 104-108. https://doi.org/https://doi.org/10.1016/j.seppur.2016.10.003

Rose, J., De Bruin, T. J. M., Chauveteau, G., Tabary, R., Hazemann, J.-L., Proux, O., Omari, A., Toulhoat, H., & Bottero, J.-Y. (2003). Aqueous Zirconium Complexes for Gelling Polymers. A Combined X-ray Absorption Spectroscopy and Quantum Mechanical Study. *The Journal of Physical Chemistry B, 107*(13), 2910-2920. https://doi.org/10.1021/jp027114c

Sheikholeslami, R., & Tan, S. (1999). Effects of water quality on silica fouling of desalination plants. *Desalination, 126*(1), 267-280. https://doi.org/https://doi.org/10.1016/S0011-9164(99)00182-4

Swift, T., Swanson, L., Bretherick, A., & Rimmer, S. (2015). Measuring poly (acrylamide) flocculants in fresh water using inter-polymer complex formation. *Environmental Science: Water Research & Technology, 1*(3), 332-340.

Wang, X., Gan, Y., Guo, S., Ma, X., Xu, M., & Zhang, S. (2018). Advantages of titanium xerogel over titanium tetrachloride and polytitanium tetrachloride in coagulation: A mechanism analysis. *Water Research*, *132*, 350-360. https://doi.org/https://doi.org/10.1016/j.watres.2017.12.081

Wang, Y., Duan, J., Liu, S., Li, W., van Leeuwen, J., & Mulcahy, D. (2014). Removal of As(III) and As(V) by ferric salts coagulation – Implications of particle size and zeta potential of precipitates. *Separation and Purification Technology*, *135*, 64-71. https://doi.org/https://doi.org/10.1016/j.seppur.2014.08.004

Worrall, F., Harriman, R., Evans, C. D., Watts, C. D., Adamson, J., Neal, C., Tipping, E., Burt, T., Grieve, I., Monteith, D., Naden, P. S., Nisbet, T., Reynolds, B., & Stevens, P. (2004). Trends in Dissolved Organic Carbon in UK Rivers and Lakes. *Biogeochemistry*, *70*(3), 369-402. https://doi.org/10.1007/s10533-004-8131-7

Wu, Y.-F., Liu, W., Gao, N.-Y., & Tao, T. (2011). A study of titanium sulfate flocculation for water treatment. *Water Research*, *45*(12), 3704-3711. https://doi.org/https://doi.org/10.1016/j.watres.2011.04.023

Xu, X., Guo, J., Yang, R., Gao, Y., Xue, Y., Wang, L., Zhang, L., Zhang, Q., Peng, M., & Liu, X. (2023). Construction of titanium-aluminum xerogel composite coagulant for removal of tetracycline in water: synergy effects and improvement mechanisms insight. *Environmental Science and Pollution Research*, *30*(7), 18285-18295. https://doi.org/10.1007/s11356-022-23448-0

Dong, Y., Zhang, P., & Lin, H. (2022). A Review of Modified Clay Minerals for Thallium Absorption from Aqueous Environment: Preparation, Application, and Mechanism. *Water, Air, & Soil Pollution*, *233*. https://doi.org/10.1007/s11270-022-05987-x

Zhao, Y. X., Gao, B. Y., Shon, H. K., Cao, B. C., & Kim, J. H. (2011). Coagulation characteristics of titanium (Ti) salt coagulant compared with aluminum (Al) and iron (Fe) salts. *Journal of Hazardous Materials*, *185*(2), 1536-1542. https://doi.org/https://doi.org/10.1016/j.jhazmat.2010.10.084

Zhao, Y. X., Gao, B. Y., Zhang, G. Z., Phuntsho, S., Wang, Y., Yue, Q. Y., Li, Q., &
Shon, H. K. (2013). Comparative study of floc characteristics with titanium
tetrachloride against conventional coagulants: Effect of coagulant dose,
solution pH, shear force and break-up period. *Chemical Engineering
Journal*, *233*, 70-79.
https://doi.org/https://doi.org/10.1016/j.cej.2013.08.017

Zhao, Y. X., Gao, B. Y., Zhang, G. Z., Qi, Q. B., Wang, Y., Phuntsho, S., Kim, J. H.,
Shon, H. K., Yue, Q. Y., & Li, Q. (2014). Coagulation and sludge recovery
using titanium tetrachloride as coagulant for real water treatment: A
comparison against traditional aluminum and iron salts. *Separation and
purification technology*, *130*, 19-27.
https://doi.org/https://doi.org/10.1016/j.seppur.2014.04.015

4. Removal of colloidal silica in water with PVDF membranes impregnated with multiwalled carbon nanotubes and graphene oxide

4.1. Introduction

Membrane technology is an integral part of separation processes in many industries including water treatment. The most widely used membranes are ultrafiltration and microfiltration, which can remove particles in the size range of 1-100 nm and 0.1 to 10 μm, respectively. In the steam boiler industry, high purity water is required to ensure proper operation of steam generation systems. High purity water will ensure lower blowdown frequency, and reduce scale build up in the boiler.

The use of reverse osmosis (RO) in boiler feed water treatment can reduce chemical costs by minimising the frequency of ion exchange regeneration. However, the downside of this is that the water passing through the RO unit requires substantial pre-treatment, which in turn adds to the systems total costs.

An alternative to RO membranes, is the use of ultrafiltration (UF) membranes. As seen in Literature review, some of the biggest challenges facing water treatment works at Tata steel, Port Talbot, is the silicate and colloidal particulates that are present in the water, which is seen to pass through the system decreasing boiler efficiency. UF membranes have been shown to reduce particulate, colloidal and organics by up to 99%. The success of membranes is accredited to their separation performance, consistency of permeate, ease of operation and reduced capital and process costs. However, the use of conventional UF membranes has faced substantial membrane fouling challenges, which can decrease the membranes lifetime and decrease membrane performance. Blockage of the membrane pores and formations of fouling layers, leading to higher transmembrane pressures.

The majority of commercially available membranes are fabricated from hydrophobic polymers, which due to their nature, are more prone to fouling. On

the plus side, they have excellent mechanical properties and high permeate rates. One of the recent trends in improving the performance of polymeric membranes is the application of inorganic filler materials with the membrane. The introduction of inorganic materials such as carbon nanotubes (CNT) and graphene oxide (GO), has shown significant improvement in the chemical and physical properties of the membrane. Polymer membranes containing CNTs have shown to significantly increase water permeability (Holt et al., 2006; Suhartono & Tizaoui, 2015). Other studies have reported that using CNT showed high hydrophilicity, permeability, chemical stability, and excellent separation performance (Wu et al., 2010). GO is another popular filler in creating mixed matrix membranes. The remarkable characteristics of GO such as its high surface area, mechanical strength and narrow pore distribution make it a popular choice (Fan et al., 2020). Incorporation of GO into membranes has shown to increase its hydrophilic features, selectivity and antifouling characteristics (Januário et al., 2021). Studies on the effect of GO and CNT incorporated membranes on inorganic contaminants such as colloidal silica is missing. This study is the first on colloidal silica removal using GO and CNT modified PVDF membranes.

This work aimed to produce PVDF membranes, enhanced with GO and CNTs, and to test them under various fouling conditions. The polymer membranes were produced via phase inversion at bench scale. Membrane performance was tested with various solutions, including colloidal silica at varying pH conditions and the effect in the absence and presence of BSA. Membranes were characterised by Fourier-transform infrared spectroscopy (FTIR), X-ray photon spectroscopy (XPS), scanning electron microscopy (SEM), contact angle measurements and surface zeta potential measurements. Fouling behaviour was studied with BSA, colloidal silica and surface water to cover a varying range of molecular sizes and charged molecules.

4.2. Materials and Methods

All reagents or chemicals were of analytical grade supplied by either Sigma Aldrich UK or Fisher Scientific UK. High quality DI water supplied by a Milli-Q system (UV Synergy system, with a MPK01 vent filter) was used throughout the

study. Glassware were washed with 4% solution of Decon 90, rinsed with Milli-Q water and dried in oven for one hour at 120 °C. For pH adjustment, 0.2M HCl and NaOH were prepared using reagent grade sodium hydroxide (NaOH) and hydrochloric acid (HCl) (32%) supplied by Fisher Scientific, UK. Multi-walled carbon nanotubes (MWCNT) and 4-10% edge oxidised graphene oxide (GO) were purchased from Sigma Aldrich, UK. N-methyl pyrrolidine (NMP) 99.5%, purchased from Sigma Aldrich, UK was used as solvent. Kynar 761 PVDF powder, which was used as polymer membrane, was purchased from Arkema Innovative Chemistry, France. Colloidal silica solutions of 35 mg/L was prepared using the LUDOX TM-50, purchased from Sigma Aldrich, UK. Bovine serum albumin (BSA) provided by Sigma Aldrich, UK, was used to prepare stock solutions of 0.5 g/L BSA.

4.2.1.Membrane fabrication

GO and MWCNT solutions were prepared in NMP at 2 wt.% and 1 wt.% respectively by dispersing 0.412 g of GO in 100 mL NMP and 0.206 g of MWCNT in 100 mL of NMP. To ensure homogeneous dispersion, the solutions were ultrasonicated for 30 minutes.

Flat sheet porous membranes were fabricated from Kynar 761 PVDF powder. Pure PVDF membranes were prepared by dissolving 4.12g of PVDF powder in a round bottom flask, followed by the addition of 20 mL of N-methyl pyrrolidine. For the mixed matrix membranes, the GO or CNT dispersion mixture was used instead of pure NMP. The round bottom flask was then placed in a setup with a mechanical mixer, water bath and hotplate underneath. The temperature was set to 70 °C, and the mixture was left to stir for 3 hours to ensure full polymer dissolution. After 3 hours, the mixture was ultrasonicated for 10-15 minutes to remove bubbles. The well homogenised, dispersed and bubble-free mixture was then ready for casting.

To cast the membrane, a glass drawdown plate was placed on the lab bench which was cleaned with acetone before use. The casting knife was then calibrated on the flat glass drawdown plate to the required thickness by adjusting the blade gap to the desired thickness using a calibrated metal plate. Once the membrane was

cast, the glass drawdown plate was immediately placed in 20L of DI water at 20 ±2 °C, to reduce solvent evaporation from the membrane surface. The membrane was left overnight to ensure solvent non-solvent dissolution. After this process the membrane was washed with DI water and stored in a plastic container containing DI water.

4.2.2. Filtration experiments

The fabricated membranes were subjugated to clean water permeation and flux tests using a recirculating cross flow filtration unit (CFU). A Micropump GA series pump, USA, powered by DP-415 A AC driver with a min speed of 500 RPM and max of 9000 RPM was used to pump the water. The unit was equipped with a flowmeter and two digital WIKA DG-10-E pressure gauges, for transmembrane pressure (TMP) measurements, and inlet/outlet valves to control flow and pressure. The following equation was used for TMP calculation:

$$TMP = \left(\frac{P_F + P_R}{2}\right) - P_p \qquad (4.1)$$

Where, P_F is the pressure of the feed (bar), P_R is the pressure of the retentate, and P_p is the pressure of the permeate (bar).

The permeate was collected in a plastic beaker and measured using an analytical balance interfaced with a PC using a data collection software to record the data over time. For the clean water permeability, water was collected for a minimum of 20 minutes to allow for the permeation to stabilise. For unpure water, the experiment was run for 30 minutes.

The water flux was calculated with the following equation:

$$J = \frac{m}{\rho A t} \qquad (4.2)$$

Where J is the membrane flux (L/m²h), m is the mass of permeate collected (kg), ρ is the water density taken equal to 998.2 kg/L, A is the effective area of the membrane (m²) and t is the time (hour) the permeate was collected. To calculate the permeability, the flux was divided by the TMP, to determine the water that passed through the surface area of the membrane per time per transmembrane

pressure. The membranes were tested with solutions of BSA, colloidal silica and real raw water from the river Afan.

4.2.3. Cleaning experiments

To determine the flux recovery of the membranes, the membranes were initially run for 15 minutes with BSA solution at 0.5 g/L, the run was stopped, and the membrane was carefully flipped. Pure water was then allowed to flow through the flipped membrane for 5 minutes. The membrane was then flipped back to its original orientation and was fed with pure water. The antifouling parameter of the membrane was determined by calculating the flux recovery ratio (FRR), which is related to the irreversible membrane fouling and was calculated measuring the pure water flux before and after BSA experiments. FRR is defined as

$$FRR \; (\%) = \frac{J_{w2}}{J_{w1}} \times 100 \qquad (4.3)$$

Where J_{w2} is the water flux of the membrane after the BSA and flipped-cleaning experiments, and J_{w1} is the water flux of the fresh membrane.

4.2.4. Characterization methods

The hydrophilicity of the membrane was measured using the contact angle method via the VCA optima contact angle instrument (VCA, USA). Sample of the required membrane was placed flat on the instrument holder using double sided tape. A single drop of water was dropped on the membrane using a syringe, and image captured using the instrument's camera. The images were then analysed using ImageJ software with the contact angle plugin. The plug-in calculates the contact angle of a drop on a flat surface using the sphere approximation and the ellipse approximation, with the points of the image being manually selected.

The membrane molecular properties were analysed using a Fourier Transform Infrared spectrophotometer (FTIR) that was coupled with Attenuated Total Reflectance (ATR) UATR Two (PerkinElmer, UK). The instrument sample holder was cleaned and then calibrated with the background being measured and

recorded. The membrane sample was then placed in the sample holder, with the active layer facing the crystal. Three measurements of the sample were taken, with the average spectra being used to compare the samples.

Membrane zeta potential was determined using the SurPASS 3, provided by Anton Paar, UK. The instrument is an Electrokinetic analyser for solid surface analysis. Initially the sample was set up using the adjustable cell gap. Before use, the pH electrode was calibrated using three buffer solutions at pHs of 3, 7 and 10. The conductivity probe was calibrated using 0.1 mol/L KCl solution. The membrane sample was then measured using 0.01 mol/L KCl solution, at pHs ranging from 2 to 10.

Membrane volume porosity and mean pore radius was specified by the gravimetric method, in which the mass of membrane sample was measured before and after drying. The membrane thickness was measured using a RS Micrometre (RS, UK), followed by drying in an oven at low temperature (50°C). The porosity relationship was then established using the following equation:

$$\varepsilon = \frac{(m_{wet} - m_{dry})/\rho_w}{\frac{(m_{wet} - m_{dry})}{\rho_w} + \frac{m_{dry}}{\rho_{PVDF}}} \tag{4.4}$$

Where, ε is the porosity, m_{wet} is the wet mass of the membrane (g), m_{dry} is the dry mass of the membrane (g), ρ_w is the density of water (g/cm³) and ρ_{PVDF} is the density of PVDF polymer is 1.78 g/cm³.

The mean pore radius (r_p) was determined by the filtration velocity method according to the revised form of the Guerout-Elford-Ferry equation:

$$r_p = \sqrt{\frac{(2.9 - 1.75\varepsilon) \times 8\eta lQ}{\varepsilon A \Delta P}} \tag{4.5}$$

Where, l is the membrane thickness (m), η is the water viscosity (Pa.s), ε is the membrane volume porosity as determined above, A is the membrane surface

area (m²), Q is the flowrate of permeate (m³/s) and ΔP is the transmembrane pressure (Pa).

The SEM imaging of the membrane surface was achieved made using a JEOL 7800 scanning electron microscope. Before use, the sample was coated with platinum with a thickness of 5 nm, using an Agar HR metal sputter coater to reduce electron charging. Once coated, the samples were then loaded into the SEM using the specimen holders. Working distance of 10 mm and probe current of 5 kV was set for all membrane samples.

The atomic composition of the membranes was analysed using AXIS Supra X-Ray Photoelectron Spectroscopy (XPS) (Kratos, UK). Samples were prepared by drying in a vacuum oven overnight at 60°C, before cutting and mounting onto the sample holder with carbon tape.

4.3. Results and Discussion

4.3.1. Membrane characterisation

Membrane characterisation is extremely important as it allows an insight into the relationship between membrane chemistry, structure and transport properties. The chemical properties of the membranes were determined by FT-IR spectrometer. The change in chemical state was determined by X-ray photoelectron spectroscopy (XPS). The hydrophilicity of the membrane was measured using water droplets on a contact angle goniometer. Membrane surface charge was measured as zeta potential by electrokinetic analysis.

4.3.1.1. FTIR

The chemical structure of the surface layer measured by ATR-FTIR membranes is shown in Figure 4.1 (a) and (b) at the wavelength ranges of 700-4000 cm^{-1} and 700-1600 cm^{-1}, respectively. The vibrations at 762 cm^{-1} are accounted for the CF_2 bending, whereas 796, 840, 875 and 974 cm^{-1} are CH_2 rocking (Shukla et al., 2010). Peaks found at 1068 cm^{-1} are for the groups of symmetric C-C stretching. CF_2 stretching is found at the bands of 1182 and 1271 cm^{-1}. Bands at 1403 cm^{-1} account for the CH_2 wagging (Nallasamy & Mohan, 2005).
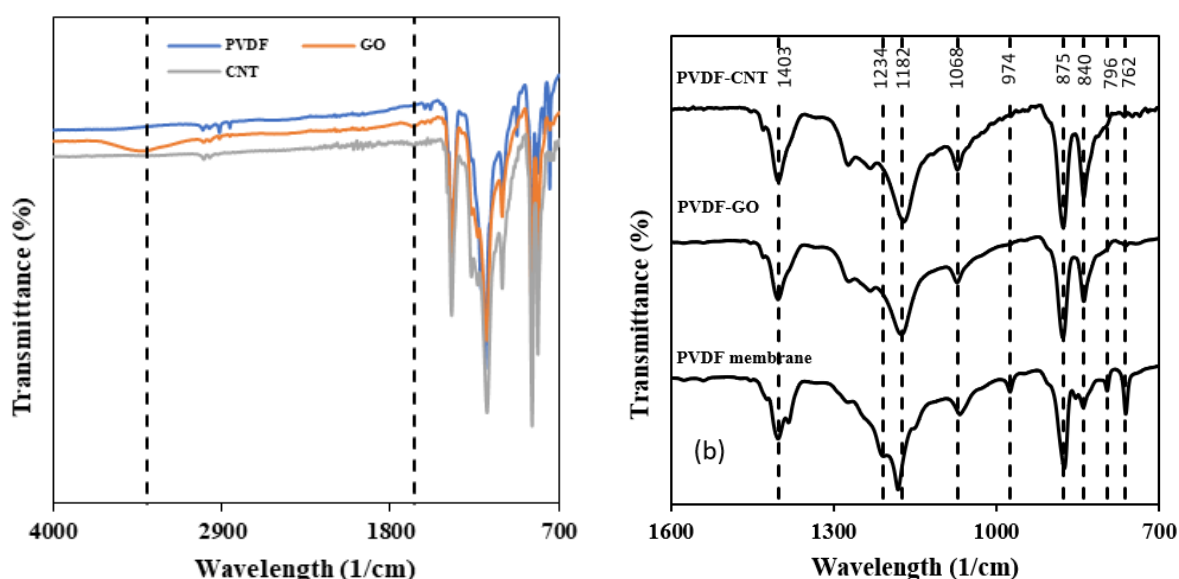
Figure 4.1. FTIR spectra of PVDF, PVDF-CNT and PVDF-GO (a) full wavelength range (700-4000 cm^{-1}) and (b) wavelength of 700-1600 cm^{-1}

The absorption spectra at 762, 840 and 1234 cm^{-1} could be selected as a representation for the PVDF crystalline phase (Kabir et al., 2017). Values at 762 cm^{-1} correspond to the α-phase whereas values of 840 cm^{-1} to γ-phase and 1280 cm^{-1} for the β-phase, which are the two main electroactive forms (Cerrada et al., 2023; Imamura et al., 2008). The pure PVDF membrane exhibits a significantly higher peak at 762 cm^{-1} compared to the PVDF-GO and PVDF-CNT membranes, whereas the introduction of GO and CNT to the membrane exhibited greater absorbance at 840 cm^{-1}. This indicates that pure PVDF membrane is found in α-phase crystalline structure whilst PVDF-CNT and PVDF-GO are mainly found in γ -phase structure. The addition of CNT and GO yielded decrease in intensity of the bands located at 762 and 796 as well as 974 cm^{-1}. Simultaneously, new bands

located at 840 cm^{-1} and 1280 cm^{-1}, indicating that β polymorph has developed (Cerrada et al., 2023).

From Figure 4.1 (b), GO membrane shows a peak between 1600 and 1700 cm^{-1} which could be attributed to the C=C absorption, from the graphene carbon bonding, this peak is not seen in the CNT membrane (Lin et al., 2008). This means that the peak seen at 1600-1700 cm^{-1} is more likely due to the C=O carboxyl stretching seen with the GO (Yang et al., 2012). With GO membrane there is also a strong broad peak seen between 3400-3500 cm^{-1}, which represents the O-H hydroxyl stretching (Surekha et al., 2020).

4.3.1.2. Membrane zeta potential

Figure 4.2 displays the results of the membrane zeta potentials of all 3 membranes. The results show that all 3 membranes at neutral pH of 7 exhibit a negative surface zeta potential. The isoelectric points for all three membranes were found to be very similar, at pH of around 3.5 to 4. As the pH was increased from their isoelectric points, both GO, and CNT membranes displayed a greater negative surface zeta potential compared to the PVDF membrane. At pH 7, the PVDF, GO and CNT membranes displayed zeta potential values of -6.6, -12.8 and -14 mV respectively. This demonstrates that the addition of GO and CNTs to the PVDF membrane, has increased the negative charge on the membrane surface. This could be due to the functional groups found on the oxidized graphene and carbon nanotubes, as seen in Figure 1(b), GO membrane had a peak 3400-3500 cm^{-1} showing that hydroxyl O-H stretching was occurring that was not present with CNT and PVDF membranes. The CNT and GO membranes had increased IR absorbance at the γ and β bands, which are the electroactive forms enhancing the zeta potential of the membranes.
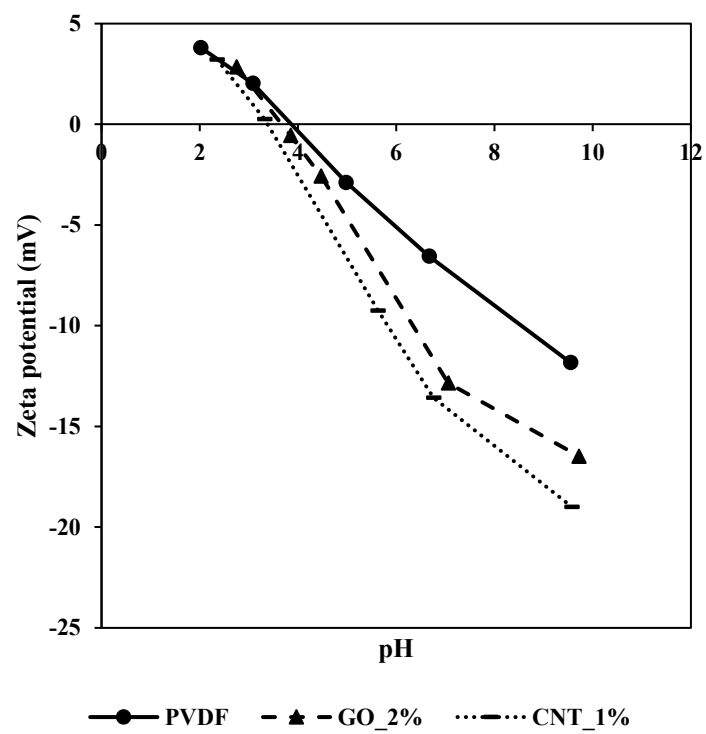
Figure 4.2. Surface zeta potential of PVDF, PVDF-GO and PVDF-CNT membranes
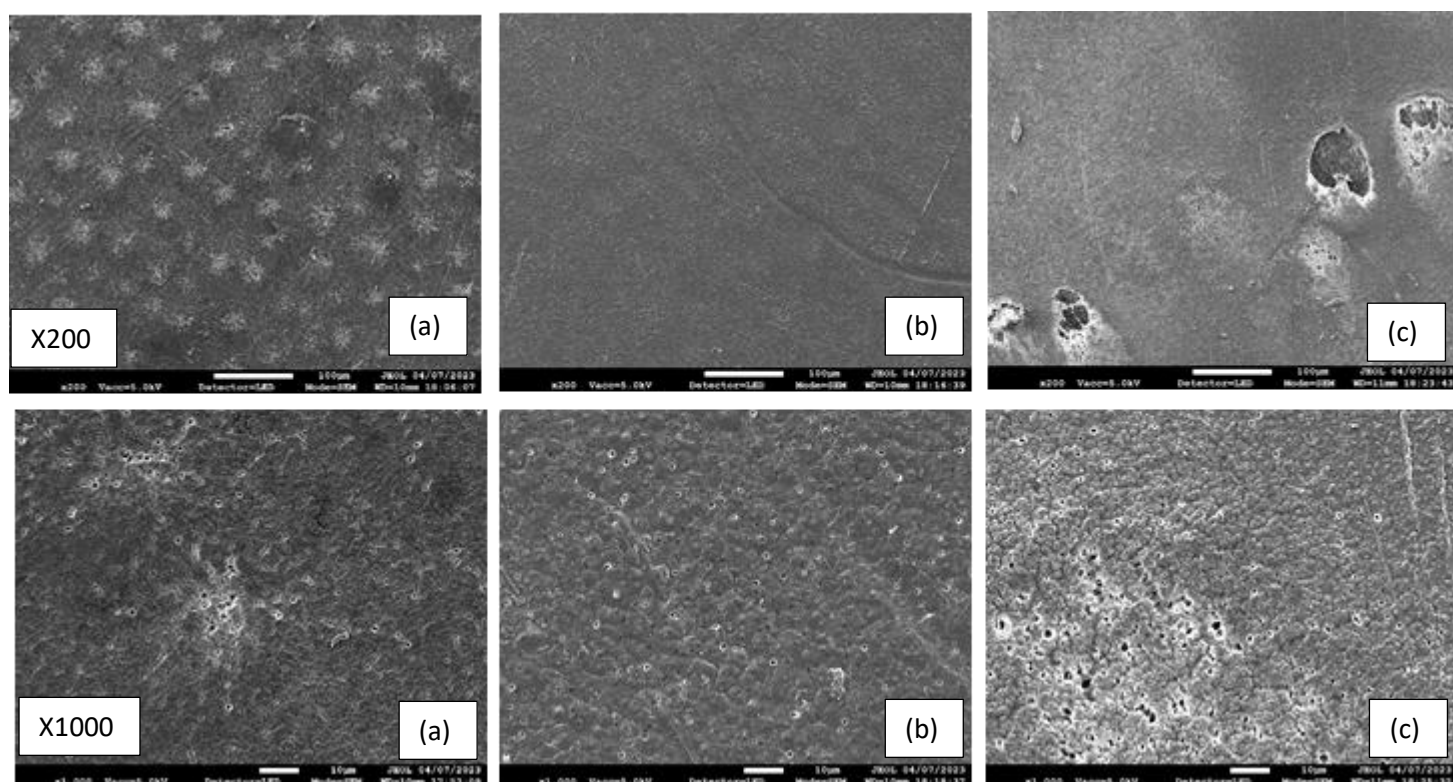
Figure 4.3. SEM images of (a) PVDF, (b) GO and (c) CNT membranes at x1000 and x200 magnification

Figure 4.3 (a), (b) and (c) shows the SEM images of the PVDF, GO and CNT membranes. Magnification of 200 and 1000 was used at a current of 5 kV. The results show that the PVDF membrane pores were not evenly distributed but had sporadically clustered over the surface of the membrane. Figure 4.3 (a) at 1000 magnification depicts clusters of pores with minimal pores outside of the cluster. With the GO membrane (Figure 4.3 (b)), the pores are more evenly spread all over the surface and are not clustered. With CNT, the membrane presents pores spread evenly with large crater like formation is observed.

The coagulation bath stage during the phase inversion method, plays a vital role on the morphology of the membrane. The morphology of the membrane depends on both the rate of outer diffusion of the solvent into the water bath as

well as the rate of inner diffusion of the water into the casting solution. The diffusion of solvent expelled from the surrounding polymer solution causes macro void growth (Guillen et al., 2011). Studies have shown that the addition of inorganic materials such as GO to PVDF casting solutions, increases the thermodynamic instability, which leads to thinner and more selective top layer with higher porosities (Mohsenpour et al., 2022). Research has shown that the presence of inorganic fillers like silica, titanium dioxide and GO can lead to membranes with more uniform pore size distribution and reduced macro void formations, these additives provide a heterogenous nucleation surface, promoting phase separation. (Wu et al., 2010; Yang et al., 2020). Addition Impregnation of the membrane matrix with of additives such as GO has also shown to increase the porosity of the membranes produced via phase inversion, as it accelerated the diffusion rate of the solvent, due to the hydrophilic nature of GO (Zhao et al., 2013).

To further characterise the pore structure of the membranes, mean pore size and porosity of the different membranes were determined and the results are shown in Table 4.1. According to this table the porosity had increased with the addition of Graphene oxide, which agrees with the SEM results. The addition of 2 wt% GO decreased the mean pore size whereas 1% CNT increased it, also in agreement with the SEM observations. Low loading of fillers such as GO and CNTs, have shown to increase pore size, but with higher loading the pore sizes decreased, studies by Choi et al had shown that MWCNTs contents of up to 1.5% had increased the pore size, but decreased at 4% (Choi et al., 2006). With a further increase in the filler loading, the viscosity of the solution would increase, leading to a diffusion delay, causing the top layer to be dense and thick with low porosity and low degree of pore interconnectivity (van de Witte et al., 1996). Table 1 shows that the pore size had increased with addition of 1% CNT, however, decreased with 2% of GO. Addition of MWCNTs have shown to increase the porosity and pore sizes of PVDF membranes (Yuan et al., 2020). Higher polymer loading has also shown to decrease pore size (Ragunath et al., 2018). The trade- off between permeability and selectivity is a fundamental aspect of membrane technology. B,

by incorporating fillers such as CNTs and GO this trade off can be manipulated to achieve both high permeability and selectivity for removing colloidal silica.

Table 4.1. PVDF, GO and CNT membrane porosity and mean pore size

Membrane type	Porosity (%)	Mean pore size (nm)
PVDF	70.8	19.8
GO (2 wt%)	74.8	14.4
CNT (1 wt%)	63.3	21.1

4.3.1.4. XPS
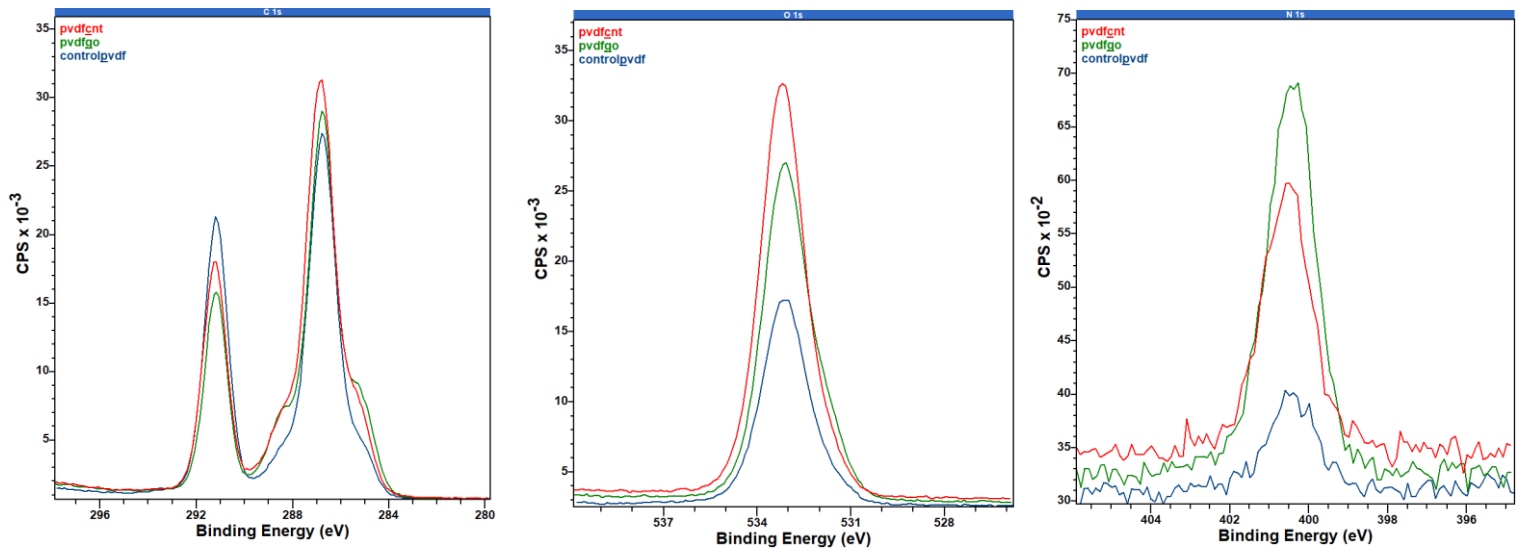
Figure 4.4. (a) Comparison of C(1s), (b) O(1s) and (c) N(1s) envelope of the three membranes

C1s XPS spectra from Figure 4.4(a) show a standard set of bands expected for PVDF, CNT and GO membranes. C-C band at 284.4 eV is used as an identifier for the presence of graphite, however, is overshadowed by the C-O/CH_2 band , as the ratio of PVDF to CNT and GO are heavily in favour of PVDF. However, there is a slight increase at 284.4 eV for the CNT and GO membranes compared to the pure PVDF, indicating presence of graphite. The peaks at 298 eV are indications of the CF_2 bonds, which decrease with the addition of CNT and GO.

Figure 4(b) compares the O1s XPS spectra of PVDF, GO and CNT membranes. The most prominent band seen with all 3 is at 531-533 eV, suggesting presence of

C-O and C=O functionalities. PVDF has the lowest peak, followed by GO and CNT membranes, respectively. The peak shapes appear slightly different due to the combination of oxygen containing groups that introduce asymmetry to the peaks.

Figure 4.4(c) shows the N1s XPS spectra for all 3 membranes, the results show an increase of the peak at 400.6 eV for the modified membranes, with GO having the highest, followed by CNT and PVDF respectively, indicating an increase in nitrogen containing groups.

Table 4.2 presents the surface composition of the membranes. Here it is found that the total oxygen increases in GO and CNT membrane, compared to PVDF. The percentage of fluorine is also seen to decrease with additions of GO and CNT.

Table 4.2. Surface composition by element for PVDF, GO and CNT membranes

Sample	Total Carbon (Atom %)	Total Calcium (Atom %)	Total Fluorine (Atom %)	Total Nitrogen (Atom %)	Total Sodium (Atom %)	Total Oxygen (Atom %)	Total Silicon (Atom %)
PVDF	55.78	0.0934	37.24	0.7	0.0398	6.04	0.0872
GO	58.84	0.0532	24.22	2.72	0.0138	14.04	0.1442
CNT	57.22	0.0252	28.58	1.46	0.0326	12.58	0.0934

4.3.1.5. Contact angle
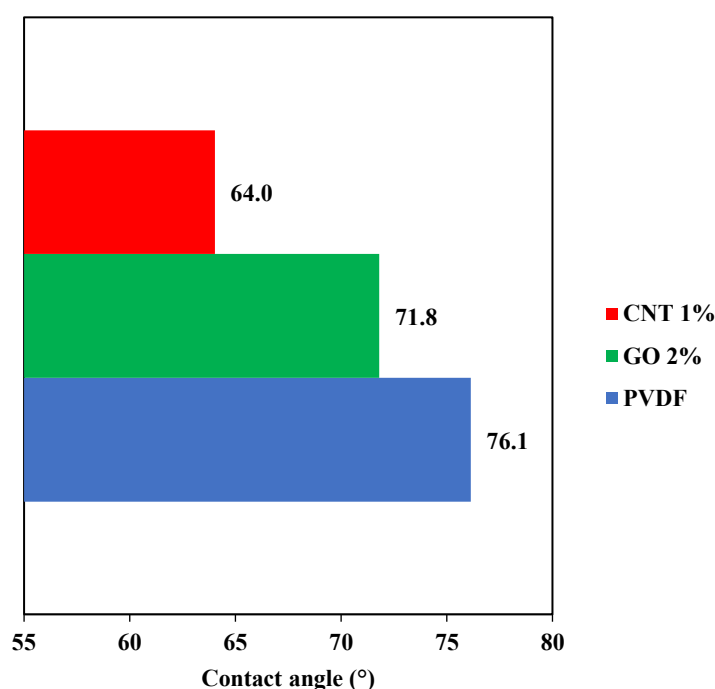
Figure 4.5. Contact angle measurements for PVDF, GO and CNT membranes

Wettability properties of the membrane can be determined by measuring the contact angle between the membrane surface area and water, as the wetting liquid. Typically, high contact angles mean that the material is more difficult to wet and that contact angles less than 90° means a higher affinity to water and therefore is a hydrophilic membrane. As shown in Figure 4.5, the averaged contact angles of the 3 different membranes show that PVDF membrane has the highest contact angles, and the addition of graphene oxide or carbon nanotubes decrease the contact angle, making the membranes more hydrophilic. CNTs and GO membranes showed a reduction of 4.3 and 12.1° respectively. This reduction in contact angle indicates that the GO and CNTs have modified the surface energy of the PVDF membrane. This could be attributed to either a higher polarity (surface charge) of the membrane surface therefore stronger intermolecular interaction between membrane and water (Giovambattista et al., 2007; Vu et al., 2021), and/or that the layer with GO and CNTs produced a smoother surface (Duca et al., 1998; Qing et al., 2019), as also observed in the

SEM images of this study (particularly the GO membrane). The contact angle had the following order: PVDF > GO > CNT, the reverse order of this is true for the hydrophilicity.

4.3.2. Performance and evaluation of membranes

4.3.2.1. Clean water permeability

Permeability of the solution depends on the transmembrane pressure, the linear velocity of water over the membrane and the compactness of the membrane. Studies have shown that with increasing TMP, the flux of permeate also increases (Madaeni & Mansourpanah, 2004; Miner, 2005).

The flux and permeability of all three membranes were evaluated using pure water. The membranes were kept soaked in aqueous solution, with regular changes of the solution. Conditions for each experiment were set that so, TMP was kept constant at 2 bar and retentate water flow rate at 1 L/min. The permeability became steady after ~10 minutes.

Figure 4.6 shows that addition of GO and CNT to PVDF membrane drastically increased the permeance of clean water. GO and CNT increased the average permeability by 141% and 174% respectively.
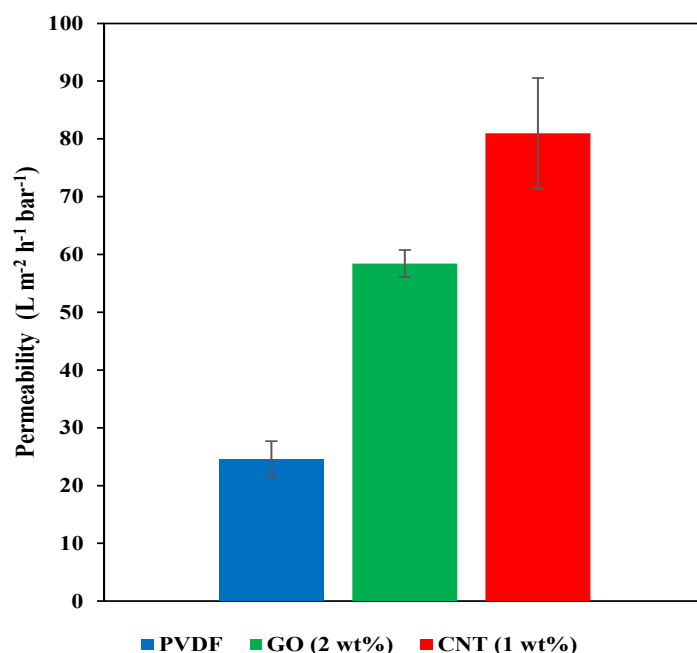
Figure 4.6. Pure water permeability of PVDF, GO and CNT membranes

This increase in permeability is consistent with increases in porosity that was seen with GO and CNT membranes, as well as the increase in pore size with CNT. This indicates that the GO and CNT additions have both improved the water permeability of the membranes. The permeability of PVDF membrane can be in the range of 10-200 L m^{-2} h^{-1} bar^{-1} (Ali et al., 2018; Wang et al., 2013; Zhang et al., 2020). Incorporating GO and CNT to membranes have shown an increase of 30-100% or more depending on GO or CNT content and dispersion (Chang et al., 2014; Gholami et al., 2022; Tofighy et al., 2021). The increased permeability can be attributed to the improved hydrophilicity, as seen with the contact angles, as well as the improved porosity.

Despite CNT exhibited a slightly reduced porosity, the permeability was seen to be greater (by 14% on average). This could be attributed to the larger pore size seen with CNTs. Additionally, the increased membrane wettability (lower contact angles) observed with CNTs and GO could also enhance the water permeability by attracting water molecules inside the membrane pores and facilitate their passage through the membrane.

4.3.2.2.Solute rejection - BSA

The permeance of PVDF, GO and CNT membranes was evaluated using BSA (0.5 g/L) and the results are presented in Figure 4.7 (a), (b) (b) c). The permeability values follow the expected trend from the pure water permeance, as discussed earlier. (a) rmeability follows the order: PVDF < GO < CNT, for BSA solution. However, when BSA solutions were used, there was a steep decline in permeability of 79%, 84% and 80% with the PVDF, GO and CNT membranes
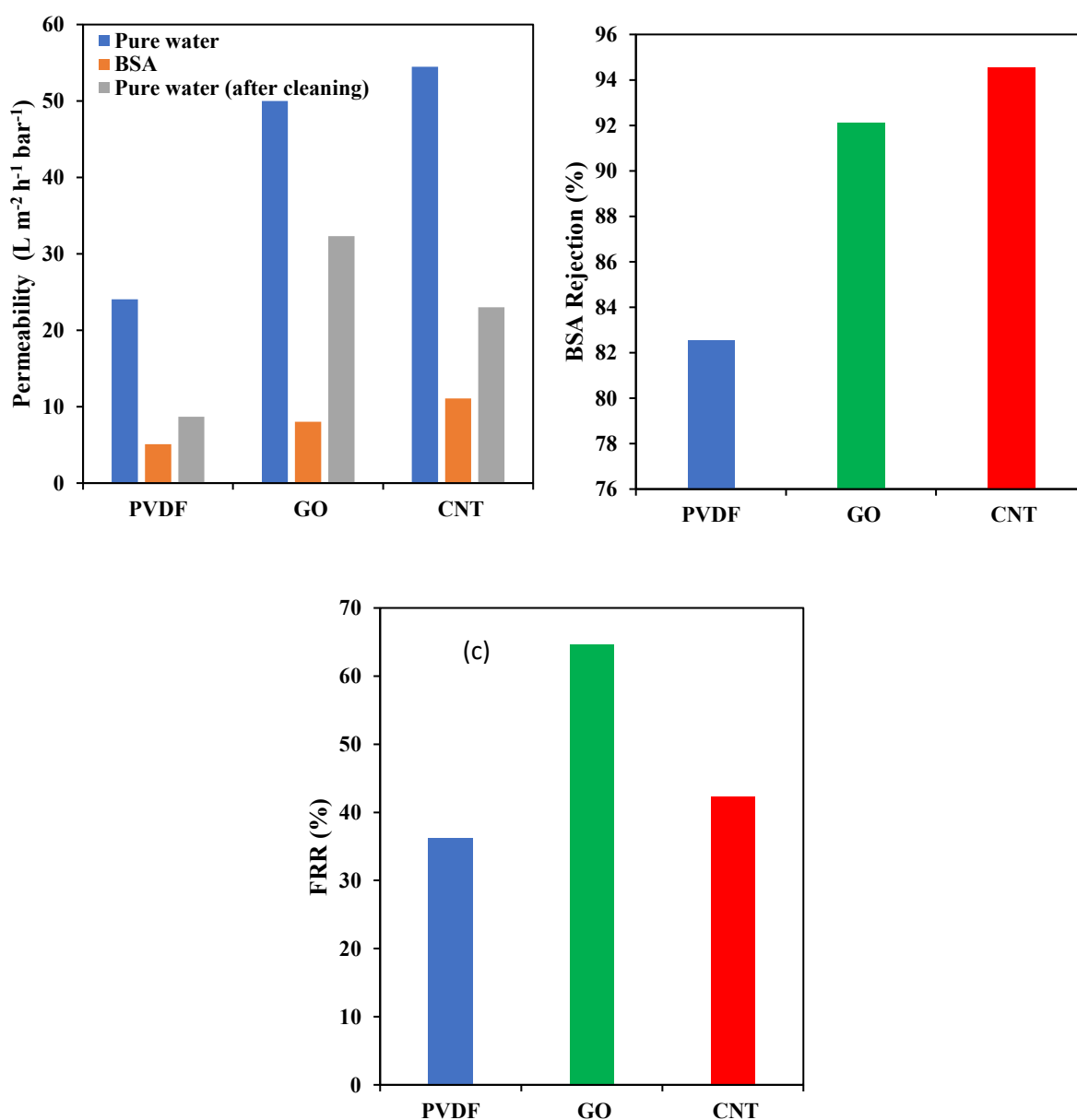
Figure 4.7. (a) permeability, (b) rejection and (c) FRR for BSA solution

respectively compared to the pure water permeance. The causes of permeability decline could be attributed to i) concentration polarisation, which is the accumulation of retained solutes and ii) fouling phenomena due to adsorption, pore-blocking and deposition of solidified solutes   (van den Berg & Smolders, 1990).

After cleaning with pure water, the highest recovery was seen with GO, followed by CNT and lastly PVDF. This is reflected in the antifouling capacity of the membrane from Figure 4.7 (c), where higher FRR (flux recovery ratio), indicate the antifouling potential of the membranes. It is observed that membrane with GO shows an FRR of 65%, whereas the membrane with CNT had an FRR of 42%, followed lastly by the PVDF membrane with FRR of 36%. The increased recovery could be attributed to the increased porosity of the GO and CNT membranes, which restricts the deposition of fouling agents on the membrane surface (Pishnamazi et al., 2020). Another reason is that hydrophobic and non-polar membranes have a higher tendency to foul. Therefore, highly charged and smooth surface are identified as key features for antifouling properties. As reported earlier, PVDF membrane had a higher contact angle and lower surface zeta potential compared to GO and CNT. Due to BSA being a negatively charged protein molecule (Fologea et al., 2007), BSA protein will have less affinity to the surface of the negatively charged membrane and therefore causes less fouling.

Figure 4.7 (b) shows the rejection of BSA for each membrane. According to the figure, the addition of GO and CNT improved the rejection of BSA. The rejection of BSA for PVDF was determined to be 83%, GO at 92% closely followed by CNT at 95%. The increased rejection could be due to the reduced pore size that was observed earlier, as well as the improved hydrophilicity seen with the contact angle experiments.

The membranes were tested with solutions of colloidal silica (35-38 mg SiO_2/L). Figure 4.8 (a) illustrates, PVDF exhibited the lowest permeability, followed by GO and CNT. PVDF membrane showed a decrease of 14% in permeability of pure water compared to colloidal silica solution, whereas GO and CNT exhibited a decrease of 16%. CNT had the largest decline in permeability at 28%.
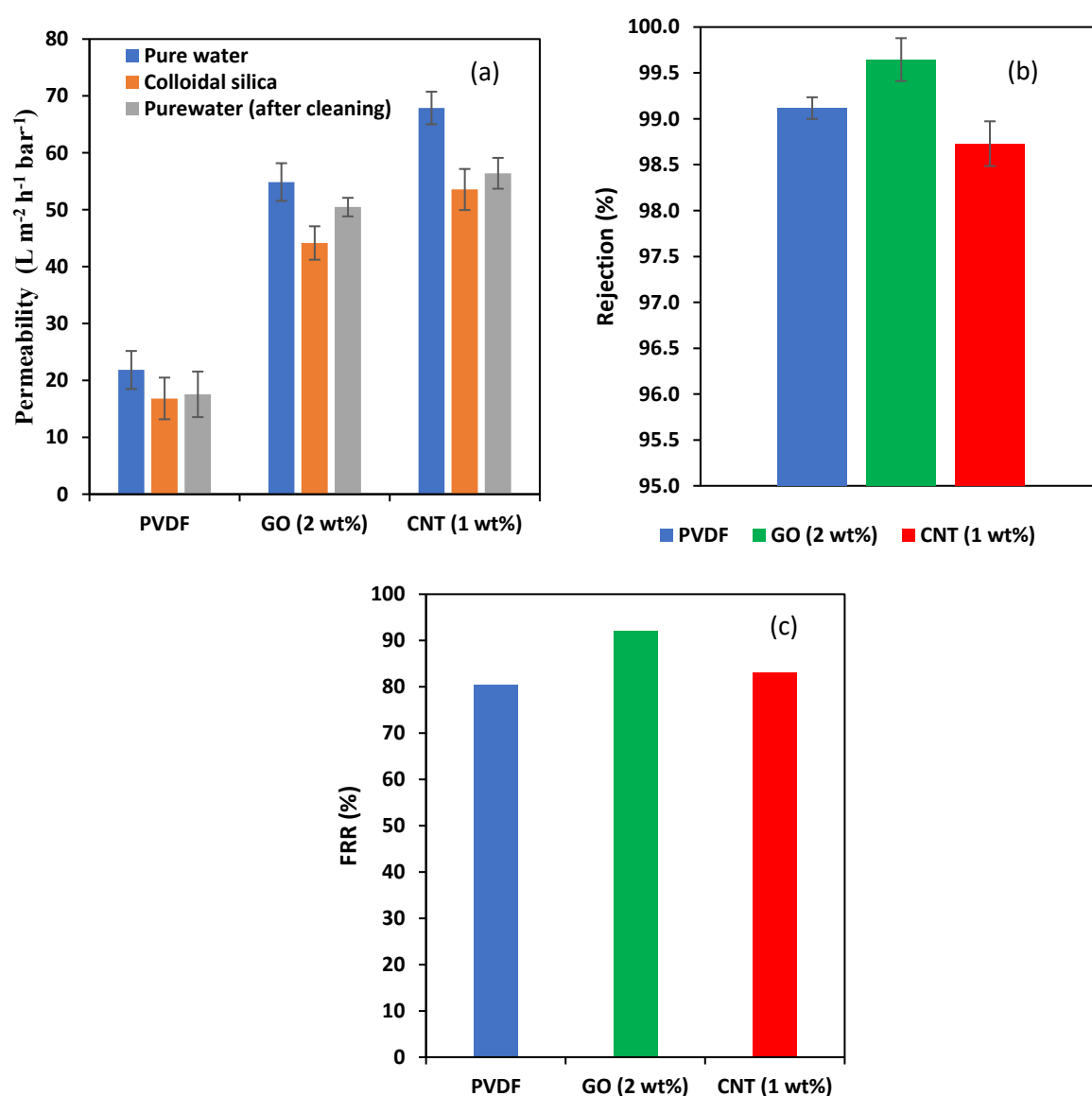
Figure 4.8. (a) permeability, (b) rejection and (c) FRR for colloidal silica solution

Figure 4.8 (b) shows the rejection percentage for colloidal silica, it reveals that GO membrane had the highest rejection (99.64%±0.23), followed by PVDF (99.11%±0.12) and lastly CNT (98.73%±0.24). Impregnation of GO shows to have

improved the rejection of colloidal silica, one possible explanation could be due to the anionic nature of the colloidal silica, which has a slight negative charge that was measured on the Zeta sizer (-10 to -25 mV), aided with the increased zeta potential of the GO membranes, leading to greater electrostatic repulsion. CNT membrane showed a decrease in rejection of colloidal silica, this could be due to the smaller sized colloidal particles being able to pass through the larger pores that were observed in SEM. The GO membrane was also seen to have greater percentage of oxygen as seen in the XPS results as well as oxygen-containing groups seen in the FTIR results, which perhaps help improving the orientation of the probing molecules in the membrane, allowing for better selectivity and higher permeability (Chumakova & Kokorin, 2023). Standard PVDF membranes have a relatively hydrophobic surface, which can lead to fouling and limited rejection of silica, pore size and porosity determine the membranes ability to reject colloidal silica (Park et al., 2015; Sahachaiyunta et al., 2002; Salvador Cob et al., 2014).

FRR for colloidal silica is presented in Figure 4.8 (c). The results show that GO (93%) and CNT (82%) had a better recovery compared to PVDF (77%), which was a similar trend to the BSA solute. The enhanced properties of the GO and CNT membranes ensured that the flux recovery was greater compared to the PVDF. Silica fouling is a major issue with membrane technologies, which can lead to concentration polarization further reducing membrane performance (Sahachaiyunta et al., 2002). Colloidal silica fouling is dependent on size of the particle, as studies have shown smaller particles (35 nm) can have higher fouling rates when longer run times were incorporated (Jang et al., 2022). In the current study, colloidal silica particles of ~38nm was tested at initial concentrations of ~35 mg SiO_2/L, by incorporating GO and CNT the rejection as well as the recovery of the membrane was greatly improved, demonstrating fouling resistance.

The effect of pH on colloidal silica permeability is presented in Figure 4.9 (a), which shows that the colloidal silica permeability increased with increasing pH, for all 3 membranes. The relatively lower permeability in the presence of colloidal silica at lower pH could be explained by the agglomeration of the colloidal particles (isoelectric point pH 2.2) creating larger particles, thus reducing the permeability. At pH above 8, the solubility of silica starts to increase, allowing silica to pass through the membrane, as such, the permeability is seen to increase at higher pHs. This is reflected in the rejection of colloidal silica, presented in Figure 4.9 (b), which shows at pH of 10, rejection of colloidal silica drops drastically for all 3 membranes.
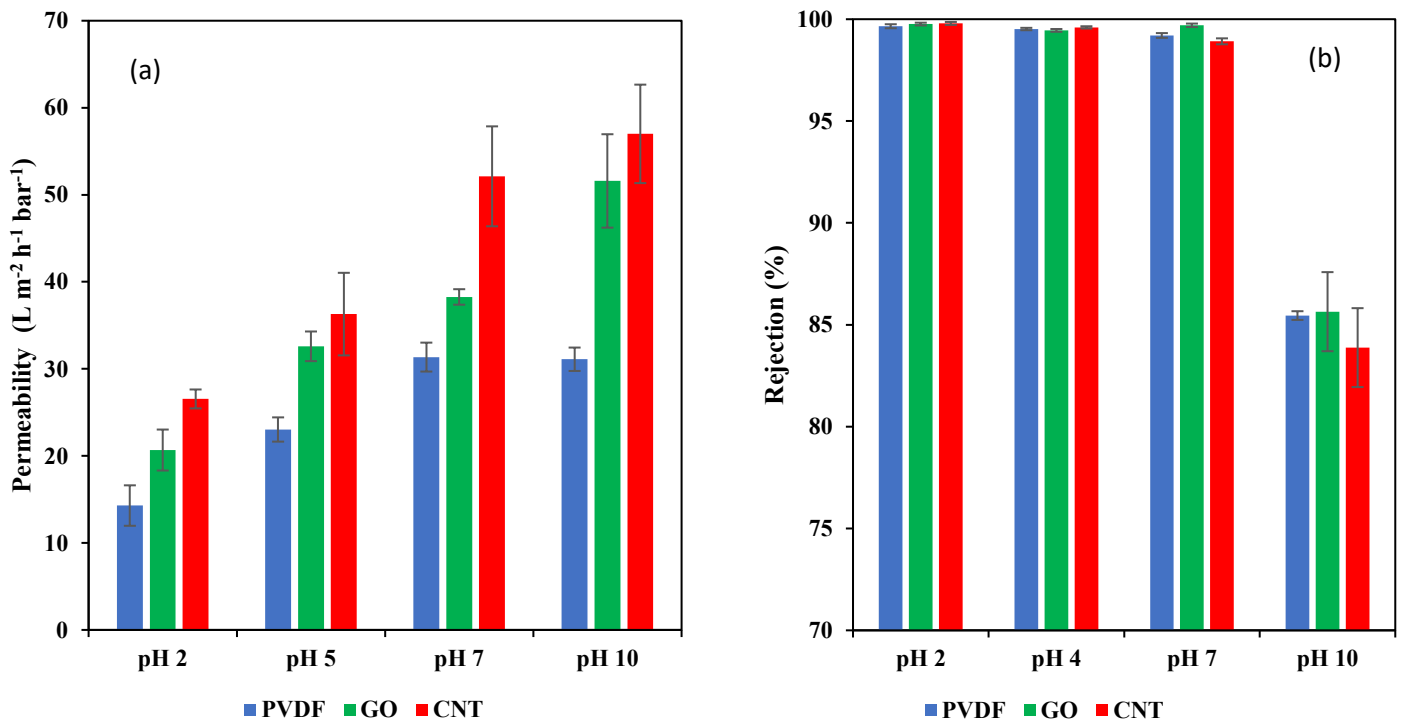
Figure 4.9.Effect of pH on (a) permeability, (b) rejection colloidal silica solution

The 3 membranes were tested with raw water from the river Afan to compare their performance in removing colloidal silica. The key characteristics of water from the river Afan are presented in Table 4.3, which shows a total silica level of 5.23 mg/L. When passed through 0.45 micron nylon filter, 4.87 mg/L of silica remained, which meant 0.36 mg/L was made up of colloidal silica. Figure 10 (a) shows that the membrane permeability followed a similar trend as previously observed in the order of PVDF < GO < CNT. Figure 4.10 (a) also shows that the membrane permeability was reduced form that of pure water when River Afan water was used by 18% for PVDF, 23% for GO and 43% for CNT.

Table 4.3. River Afan water characteristics

Parameter	Value
Total silica (mg SiO_2/L)	5.23
Colloidal silica (mg SiO_2/L)	0.36
TOC (mg/L)	1.7
pH	7.1

Figure 4.10 (b) displays the rejection of colloidal silica. The GO membrane showed the greatest rejection of silica at 30%, followed by CNT at 26% and lastly PVDF which showed a rejection of 19%. The synergistic properties of decreased contact angle (improved hydrophilicity), decreased membrane zeta potential (charge repulsion) and improved porosity, with the addition of GO and CNT, has seemingly played a role in the improved performance of the membrane. GO showed the greatest rejection compared to CNT, which could be due to the smaller pores present and therefore it was able to remove greater levels of colloidal particles in the water.

As seen with the BSA and colloidal silica, the FRR of the membranes followed the same trend, with GO having the highest recovery, followed by CNT and PVDF, seen in Figure 4.10 (c). Due to the nature of surface water, many of the particulate

matter is negatively charged (Gerritsen & Bradley, 1987; Perret et al., 1994). Therefore, the previously discussed principles of zeta potential and hydrophilicity apply to the River Afan particulates, improving the permeability and antifouling of the membranes.

Despite a large portion of colloidal silica particles were removed by the membranes, the total silica concentration remains relatively high. Ultrafiltration membranes alone appear not suited for the removal of silica in water, and that total silica removal would require a hybrid technology.
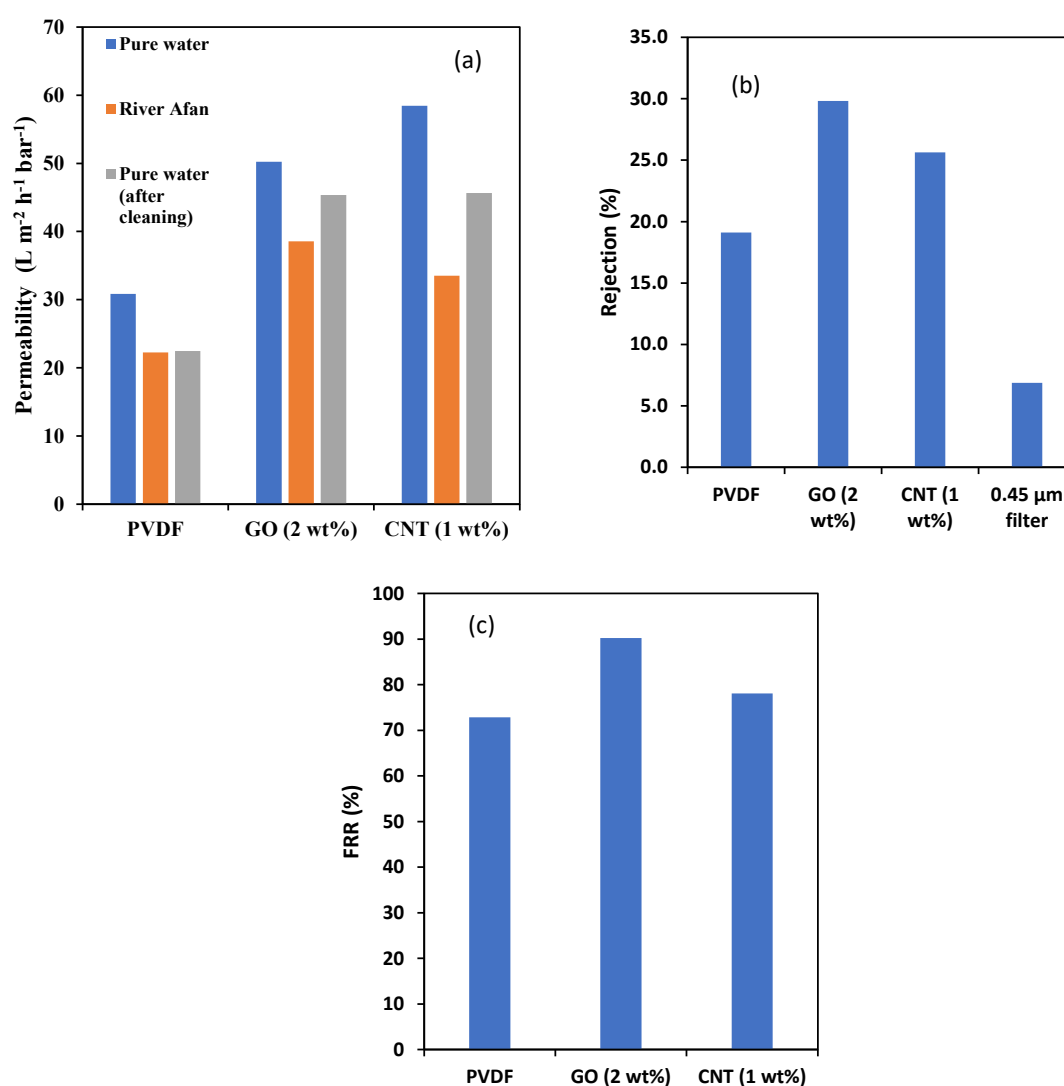
Figure 4.10. (a) Permeability, (b) rejection and (c) FRR for River Afan

4.4. RO membrane implantation at Tata Steel Port Talbot
Given the effectiveness and operational ease of membranes, RO membranes have been implemented at Tata Steel, Port Talbot Margam C (as of 2022). The

membranes are fed by the mixed bed outlets, and go onto the condensate polishers. In this way, the RO system removes all colloidal particles and also reduces the ionic load on the condensate polisher. This can help increase the longevity of the condensate polisher, reducing the regeneration required. Tests for the RO membranes silica removal was conducted via the HACH 8282 method, results are found in Appendices C.

4.5. Conclusions

GO and CNT enhanced PVDF membranes with improved antifouling properties and permeability was successfully produced. The membranes were characterised by FTIR, XPS, SEM. Solute rejection on the membrane was tested with solutions of BSA, colloidal silica and surface water (River Afan). The highlights from this chapter include:

- FTIR data showed similar peaks for the modified (GO and CNT) and unmodified (PVDF) membranes. However, the major difference was with the addition of GO, additional peaks relating to C=O carboxyl and O-H hydroxyl groups were seen, compared to PVDF and CNT membrane.

- XPS data backed this up, revealing that GO membrane had the highest oxygen content (14%) followed by CNT (12%) and PVDF (6%). It also revealed that the fluorine content had drastically decreased with the addition of GO and CNT.

- Membrane porosity increased substantially with the addition of GO and CNT, with an increase of 40% and 29%, respectively compared to PVDF. Pore volumes increased with the addition of 1 wt% CNT but seemed to decrease with the addition of 2 wt% GO.

- Contact angle measurements revealed the addition of GO and CNT reduced the contact angle of water compared to PVDF, indicating improved hydrophilicity of the modified membranes.

- Zeta potential measurements of the membrane surface demonstrated a slightly lower isoelectric point of modified membranes. At pH of 7, GO and CNT modified membranes showed a lower zeta potential compared to PVDF membrane.

- The pure water permeability of the modified membranes showed a significant enhancement, with increases of 141% for GO and 174% for CNT, respectively.

- BSA rejection and flux recovery ratio (FRR) was seen to be improved by the addition of GO and CNT. CNT had the highest permeability, followed by GO and lastly PVDF. Rejection of BSA increased by 10% for GO and 12% for CNT. GO had the highest FRR at 65%, followed by CNT 42% and lastly PVDF at 36%, suggesting that the modified membranes exhibit greater antifouling properties.

- Similar trends of improved permeance and FRR with colloidal silica solution was seen with the modified membranes.

- Effect of pH on colloidal silica was tested for the membranes. Results showed that permeability increased with increasing pH. However, the rejection drastically decreased at pH 10. This was attributed to the increasing solubility of colloidal silica at pH>10.

- River Afan, which is the water source used at Tata Steel, Port Talbot was tested with the membrane to determine the colloidal silica removal. Permeance, colloidal silica rejection and FRR had improved with the modified membranes. Rejection of total silica had improved by 10.7% for GO and 6.5% for CNT. However, total silica remained relatively high, suggesting UF membranes alone are only good at removing the colloidal silica, and that a hybrid technology is required for the removal of total silica.

4.6. References

Ali, I., Bamaga, O. A., Gzara, L., Bassyouni, M., Abdel-Aziz, M. H., Soliman, M. F., Drioli, E., & Albeirutty, M. (2018). Assessment of Blend PVDF Membranes, and the Effect of Polymer Concentration and Blend Composition. *Membranes, 8*(1).

Cerrada, M. L., Arranz-Andrés, J., Caballero-González, A., Blázquez-Blázquez, E., & Pérez, E. (2023). The β Form in PVDF Nanocomposites with Carbon Nanotubes: Structural Features and Properties. *Polymers, 15*(6).

Chang, X., Wang, Z., Quan, S., Xu, Y., Jiang, Z., & Shao, L. (2014). Exploring the synergetic effects of graphene oxide (GO) and polyvinylpyrrodione (PVP) on poly(vinylylidenefluoride) (PVDF) ultrafiltration membrane performance. *Applied Surface Science, 316,* 537-548. https://doi.org/https://doi.org/10.1016/j.apsusc.2014.07.202

Choi, J.-H., Jegal, J., & Kim, W.-N. (2006). Fabrication and characterization of multi-walled carbon nanotubes/polymer blend membranes. *Journal of membrane science, 284*(1), 406-415. https://doi.org/https://doi.org/10.1016/j.memsci.2006.08.013

Chumakova, N., & Kokorin, A. (2023). Graphene Oxide Membranes—Synthesis, Properties, and Applications. *Membranes, 13*(9), 771. https://www.mdpi.com/2077-0375/13/9/771

Duca, M. D., Plosceanu, C. L., & Pop, T. (1998). Surface modifications of polyvinylidene fluoride (PVDF) under rf Ar plasma. *Polymer Degradation and Stability, 61*(1), 65-72. https://doi.org/https://doi.org/10.1016/S0141-3910(97)00130-4

Fan, X., Cai, C., Gao, J., Han, X., & Li, J. (2020). Hydrothermal reduced graphene oxide membranes for dyes removing. *Separation and purification technology, 241,* 116730. https://doi.org/https://doi.org/10.1016/j.seppur.2020.116730

Fologea, D., Ledden, B., McNabb, D. S., & Li, J. (2007). Electrical characterization of protein molecules by a solid-state nanopore. *Applied Physics Letters, 91*(5). https://doi.org/10.1063/1.2767206

Gerritsen, J., & Bradley, S. W. (1987). Electrophoretic mobility of natural particles and cultured organisms in freshwaters1. *Limnology and Oceanography, 32*(5), 1049-1058. https://doi.org/https://doi.org/10.4319/lo.1987.32.5.1049

Gholami, S., Llacuna, J. L., Vatanpour, V., Dehqan, A., Paziresh, S., & Cortina, J. L. (2022). Impact of a new functionalization of multiwalled carbon nanotubes on antifouling and permeability of PVDF nanocomposite membranes for dye wastewater treatment. *Chemosphere, 294, 133699.* https://doi.org/https://doi.org/10.1016/j.chemosphere.2022.133699

Giovambattista, N., Debenedetti, P. G., & Rossky, P. J. (2007). Effect of Surface Polarity on Water Contact Angle and Interfacial Hydration Structure. *The Journal of Physical Chemistry B, 111*(32), 9581-9587. https://doi.org/10.1021/jp071957s

Guillen, G. R., Pan, Y., Li, M., & Hoek, E. M. V. (2011). Preparation and Characterization of Membranes Formed by Nonsolvent Induced Phase Separation: A Review. *Industrial & Engineering Chemistry Research, 50*(7), 3798-3817. https://doi.org/10.1021/ie101928r

Holt, J. K., Park, H. G., Wang, Y., Stadermann, M., Artyukhin, A. B., Grigoropoulos, C. P., Noy, A., & Bakajin, O. (2006). Fast Mass Transport Through Sub-2-Nanometer Carbon Nanotubes. *Science, 312*(5776), 1034-1037. https://doi.org/doi:10.1126/science.1126298

Imamura, R., Silva, A. B., & Gregorio Jr., R. (2008). γ→β Phase transformation induced in poly(vinylidene fluoride) by stretching. *Journal of Applied Polymer Science, 110*(5), 3242-3246. https://doi.org/https://doi.org/10.1002/app.28851

Jang, Y., Lee, J.-G., Fortunato, L., Lee, J., Lee, Y., An, A. K., Ghaffour, N., Lee, S., & Jeong, S. (2022). Colloidal silica fouling mechanism in direct-contact membrane distillation. *Desalination, 527, 115554.* https://doi.org/https://doi.org/10.1016/j.desal.2022.115554

Januário, E. F. D., Vidovix, T. B., Beluci, N. d. C. L., Paixão, R. M., Silva, L. H. B. R. d., Homem, N. C., Bergamasco, R., & Vieira, A. M. S. (2021). Advanced graphene oxide-based membranes as a potential alternative for dyes removal: A review. *Science of The Total Environment, 789*, 147957. https://doi.org/https://doi.org/10.1016/j.scitotenv.2021.147957

Kabir, E., Khatun, M., Nasrin, L., Raihan, M. J., & Rahman, M. (2017). Pure β-phase formation in polyvinylidene fluoride (PVDF)-carbon nanotube composites. *Journal of Physics D: Applied Physics, 50*(16), 163002.

Lin, W., Xiu, Y., Zhu, L., Moon, K.-s., & Wong, C. P. (2008). *Assembling of carbon nanotube structures by chemical anchoring for packaging applications.* https://doi.org/10.1109/ECTC.2008.4550005

Madaeni, S. S., & Mansourpanah, Y. (2004). Chemical cleaning of reverse osmosis membranes fouled by whey. *Desalination, 161*(1), 13-24. https://doi.org/https://doi.org/10.1016/S0011-9164(04)90036-7

Miner, G. (2005). Nanofiltration: principles and applications. *American Water Works Association. Journal, 97*(11), 121.

Mohsenpour, S., Leaper, S., Shokri, J., Alberto, M., & Gorgojo, P. (2022). Effect of graphene oxide in the formation of polymeric asymmetric membranes via phase inversion. *Journal of membrane science, 641*, 119924. https://doi.org/https://doi.org/10.1016/j.memsci.2021.119924

Nallasamy, P., & Mohan, S. (2005). Vibrational spectroscopic characterization of form II poly(vinylidene fluoride). *Indian Journal of Pure and Applied Physics, 43*, 821-827.

Park, S. Y., Choi, S. H., Chung, J. W., & Kwak, S.-Y. (2015). Anti-scaling ultrafiltration/microfiltration (UF/MF) polyvinylidene fluoride (PVDF) membranes with positive surface charges for Ca2+/silica-rich wastewater treatment. *Journal of membrane science, 480*, 122-128. https://doi.org/https://doi.org/10.1016/j.memsci.2015.01.041

Perret, D., Newman, M. E., Nègre, J.-C., Chen, Y., & Buffle, J. (1994). Submicron particles in the rhine river—I. Physico-chemical characterization. *Water Research, 28*(1), 91-106. https://doi.org/https://doi.org/10.1016/0043-1354(94)90123-6

Pishnamazi, M., Koushkbaghi, S., Hosseini, S. S., Darabi, M., Yousefi, A., & Irani, M. (2020). Metal organic framework nanoparticles loaded-PVDF/chitosan nanofibrous ultrafiltration membranes for the removal of BSA protein and Cr(VI) ions. *Journal of Molecular Liquids, 317,* 113934. https://doi.org/https://doi.org/10.1016/j.molliq.2020.113934

Qing, W., Wang, J., Ma, X., Yao, Z., Feng, Y., Shi, X., Liu, F., Wang, P., & Tang, C. Y. (2019). One-step tailoring surface roughness and surface chemistry to prepare superhydrophobic polyvinylidene fluoride (PVDF) membranes for enhanced membrane distillation performances. *Journal of Colloid and Interface Science, 553,* 99-107. https://doi.org/https://doi.org/10.1016/j.jcis.2019.06.011

Ragunath, S., Roy, S., & Mitra, S. (2018). Carbon nanotube immobilized membrane with controlled nanotube incorporation via phase inversion polymerization for membrane distillation based desalination. *Separation and purification technology, 194,* 249-255. https://doi.org/https://doi.org/10.1016/j.seppur.2017.11.053

Sahachaiyunta, P., Koo, T., & Sheikholeslami, R. (2002). Effect of several inorganic species on silica fouling in RO membranes. *Desalination, 144*(1), 373-378. https://doi.org/https://doi.org/10.1016/S0011-9164(02)00346-6

Salvador Cob, S., Hofs, B., Maffezzoni, C., Adamus, J., Siegers, W. G., Cornelissen, E. R., Genceli Güner, F. E., & Witkamp, G. J. (2014). Silica removal to prevent silica scaling in reverse osmosis membranes. *Desalination, 344,* 137-143. https://doi.org/https://doi.org/10.1016/j.desal.2014.03.020

Shukla, N., Shukla, A., Thakur, A., & Choudhary, R. N. (2010). Low temperature ferroelectric behaviour of PVDF based composites. *Indian Journal of Engineering and Materials Sciences, 15.*

Suhartono, J., & Tizaoui, C. (2015). Polyvinylidene fluoride membranes impregnated at optimised content of pristine and functionalised multi-walled carbon nanotubes for improved water permeation, solute rejection and mechanical properties. *Separation and purification technology, 154,* 290-300. https://doi.org/https://doi.org/10.1016/j.seppur.2015.09.009

Surekha, G., Krishnaiah, K. V., Ravi, N., & Suvarna, R. P. (2020). FTIR, Raman and XRD analysis of graphene oxide films prepared by modified Hummers method. Journal of Physics: Conference Series,

Tofighy, M. A., Mohammadi, T., & Sadeghi, M. H. (2021). High-flux PVDF/PVP nanocomposite ultrafiltration membrane incorporated with graphene oxide nanoribbones with improved antifouling properties. *Journal of Applied Polymer Science, 138*(4), 49718. https://doi.org/https://doi.org/10.1002/app.49718

van de Witte, P., Dijkstra, P. J., van den Berg, J. W. A., & Feijen, J. (1996). Phase separation processes in polymer solutions in relation to membrane formation. *Journal of membrane science, 117*(1), 1-31. https://doi.org/https://doi.org/10.1016/0376-7388(96)00088-9

van den Berg, G. B., & Smolders, C. A. (1990). Flux decline in ultrafiltration processes. *Desalination, 77*, 101-133. https://doi.org/https://doi.org/10.1016/0011-9164(90)85023-4

Vu, D. L., Le, C. D., Vo, C. P., & Ahn, K. K. (2021). Surface polarity tuning through epitaxial growth on polyvinylidene fluoride membranes for enhanced performance of liquid-solid triboelectric nanogenerator. *Composites Part B: Engineering, 223*, 109135. https://doi.org/https://doi.org/10.1016/j.compositesb.2021.109135

Wang, Q., Wang, X., Wang, Z., Huang, J., & Wang, Y. (2013). PVDF membranes with simultaneously enhanced permeability and selectivity by breaking the tradeoff effect via atomic layer deposition of TiO_2. *Journal of membrane science, 442*, 57-64. https://doi.org/https://doi.org/10.1016/j.memsci.2013.04.026

Wu, H., Tang, B., & Wu, P. (2010). Novel ultrafiltration membranes prepared from a multi-walled carbon nanotubes/polymer composite. *Journal of membrane science, 362*(1), 374-383. https://doi.org/https://doi.org/10.1016/j.memsci.2010.06.064

Yang, T., Liu, L., Liu, J.-w., Chen, M.-L., & Wang, J.-H. (2012). Cyanobacterium metallothionein decorated graphene oxide nanosheets for highly selective

adsorption of ultra-trace cadmium. *J. Mater. Chem.*, 22, 21909-21916. https://doi.org/10.1039/C2JM34712A

Yang, Z., Sun, P.-F., Li, X., Gan, B., Wang, L., Song, X., Park, H.-D., & Tang, C. Y. (2020). A critical review on thin-film nanocomposite membranes with interlayered structure: mechanisms, recent developments, and environmental applications. *Environmental Science & Technology*, 54(24), 15563-15583.

Yuan, X.-T., Xu, C.-X., Geng, H.-Z., Ji, Q., Wang, L., He, B., Jiang, Y., Kong, J., & Li, J. (2020). Multifunctional PVDF/CNT/GO mixed matrix membranes for ultrafiltration and fouling detection. *Journal of Hazardous Materials*, *384*, 120978. https://doi.org/https://doi.org/10.1016/j.jhazmat.2019.120978

Zhang, Q., Cui, Z., & Li, W. (2020). High permeability poly(vinylidene fluoride) ultrafiltration membrane doped with polydopamine modified TiO2 nanoparticles. *Chinese Journal of Chemical Engineering*, 28(12), 3152-3158. https://doi.org/https://doi.org/10.1016/j.cjche.2020.08.026

Zhao, C., Xu, X., Chen, J., & Yang, F. (2013). Effect of graphene oxide concentration on the morphologies and antifouling properties of PVDF ultrafiltration membranes. *Journal of Environmental Chemical Engineering*, *1*(3), 349-354. https://doi.org/https://doi.org/10.1016/j.jece.2013.05.014

5. Ion exchange for the removal of soluble silica

5.1. Introduction

Silica content of water is very critical to the operation of high pressure steam boiler systems as it is volatile enough to carry over to the vapour partition and can deposit on turbine blades (Ghosh, 1988). Ion exchange resin is a well-established technology which can be used for the demineralisation of water to pre-treat boiler feed water. At Tata steel, Port Talbot, the boiler feed water goes through 3 major ion exchange processes, which includes the cation, anion and mixed bed exchangers. A common challenge across all applications of ion exchange is related to selectivity, in which the removal of a target contaminant is reduced due to the presence of competing ions in water (Barrer & Klinowski, 1974; Muhammad et al., 2019). This can restrict applications for silica removal due to its chemistry. Dissolved silica in water is present as orthosilicic acid (H_4SiO_4), which is a weak acid that does not ionise well and therefore it is, hard to remove with using ion exchange. Silica removal by ion exchange typically requires a strong base anionic resin in the hydroxide form, which is then regenerated with caustic soda (Inc., 2014; Sik Ali et al., 2004).

Recent studies have demonstrated that transition metal oxides, including those of iron, copper, and zirconium, can selectively adsorb anionic pollutants like arsenate and phosphate (Acelas et al., 2015; Cumbal & Sengupta; Kociołek-Balawejder et al., 2017; Padungthon et al., 2014). Disadvantage of these metal oxides is that they are mechanically weak and as a result cause excessive pressure drop on fixed beds. However, dispersing these metal oxide nanoparticles in support material such as ion exchange resin has shown to enhance their mechanical properties (Zhang et al., 2008). Additionally, phosphate ions being strong bidentate ligands, can readily form inner-sphere complexes with transitional metals such as iron (Goldberg & Sposito, 1985). Competing ions such as phosphate, nitrate and sulphate can only form outer sphere complexes, which results in them competing with silica for the ion exchange sites. For example, the metal oxide component of a iron impregnated resin was found to be selective towards phosphate, which increases its selectivity and its overall exchange

capacity towards phosphates (Cross et al., 2009; T Nur et al., 2014; Yoon et al., 2014).

FerrIX A33E by Purolite, a commercially available ion exchange resin developed for arsenic removal, contains iron oxide nanoparticles. However, there is no data from studies on its effectiveness for removing silica, particularly in the presence of competing ions such as phosphates and nitrates. In addition, the few studies that tackled phosphates with FerrIX A33E reported discrepancies in the resin capacity and its regeneration behaviour as well as the effects of the operating conditions on resin exchange properties and column performance are not well studied (T. Nur et al., 2014). Therefore, this study was developed to evaluate the removal of silica as well as competing ions such as phosphate by FerrIX A33E and a common ion exchange A400 focusing on ion exchange capacity, kinetics, and breakthrough experiments in a batch and fixed-bed column semi-continuous modes. Common and newly adapted mathematical models were used to predict the isotherms, exchange kinetics, and column breakthrough curves. The results reported in this study enhance understanding of the performance of FerrIX A33E for silica removal and provide useful information for design and scaling up of the ion exchange process.

5.2. Materials and Methods

5.2.1. Chemicals and reagents

Analytical grade sodium metasilicate nonahydrate ($Na_2SiO_3.9H_2O$), sodium phosphate monohydrate ($NaH_2PO_4.H_2O$powder (Acros Organics, UK), Sodium sodium chloride (NaCl) powder, (Sigma Alrich, UK), and sodium nitrate (NaNO3) powder (Sigma Aldrich, UK) were used in this study. The iron impregnated FerrIX A33E and A400 anion exchange resins was provided by (Purolite, USA), both particle size ranged from 300-1200 μm. Microscope images of the FerrIX resin can be found in Appendices B.

5.2.2. Analysis

Analysis of silica and phosphate concentrations was conducted using a microwave plasma atomic emission spectrometer (Agilent 4200 MP-AES). The concentration of the anions chloride and nitrate was analysed using an ion

chromatograph (Thermo Scientific Dionex Integrion HPIC) fitted with a Dionex IonPac AS29-Fast-4μm analytical column and a Dionex IonPac AG13A-5μm guard column. The eluent used was the Dionex AS14A (8.0 mM sodium carbonate, 1.0mM sodium bicarbonate) with a set flowrate of 0.5 mL/min. Calibration curves for silica was prepared using HACH silica standard solution 10.0 ±0.1 mg/L as SiO_2, which was diluted with DI water. Calibration standard for chloride, nitrate and phosphate was prepared, by creating stock solutions using the analytical grade reagents (Calibrations curves can be found in Appendices A).

The BET surface area analysis was conducted with a NOVA 2000E, with nitrogen gas and liquid nitrogen. NovaWin software was used for the analysis of the results. Initially the sample was degassed with a vacuum pump and heated with a mantle pocket to 100°C for 3 hours. The samples were weighed before and after the degassing process. Following on from the degassing, a nitrogen adsorption/desorption cycle was run and recorded at -196°C with the use of liquid nitrogen.

5.2.3. Adsorption isotherms

The isotherm experiments were carried out at room temperature (20±20C) using aqueous samples (40 mL) placed in 50mL-plastic sample tubes and agitated for 24h using a 12-position rotating mixer (Stuart SB3 rotator) set at 40 rpm. Silica uptake onto the resin was calculated by Equation (5.1), which was derived from mass balances on the liquid and resin phases assuming that any change in phosphate mass in the liquid phase was due to the resin uptake.

$$q_e = V \times \frac{(C_o - C_e)}{m_{IX}} \qquad (5.1)$$

Where q_e is the phosphate solute uptake onto the resin (mg P/g), V is the volume of solution (L), C_o C_o and C_e are the initial and equilibrium concentrations (mg P/L), and m_{IX} is the mass of the ion exchange resin (g). This was repeated with multicomponent stock solutions containing, silica, phosphate and nitrate.

5.2.4. Column experiments

Dynamic semi-batch column ion exchange experiments were carried out using an ion exchange experimental rig (CE300, G.U.N.T, Germany); its layout is shown in Figure 5.1. The column internal diameter was 21.2 mm and the total column height was 400 mm. The column was run in a down-flow mode and samples at the column exit were collected at regular intervals of time. The breakthrough curve was obtained by plotting the exit concentration versus time. Flowrates, column height and inlet concentrations were varied.
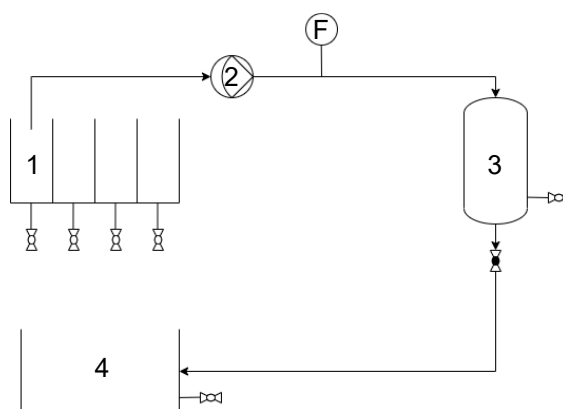
Figure 5.1. Schematic diagrams of fixed-bed column studies: 1 -collecting tank, 2 – diaphragm pump, 3 – Anion exchange column, 4 – waste tank, F – flowmeter.

5.2.5. Data analysis models

5.2.5.1. Isotherm models

Table 5.1. Isotherm model equations and their parameters for phosphate ion exchange onto FerrIX A33E resin

Model	Equation	
Langmuir	$$q_e = \frac{q_m K_L C_e}{1 + K_L C_e}$$ $$Linear\ form: \frac{1}{q_e} = \frac{1}{q_m K_L C_e} + \frac{1}{q_m}$$	(5.2)
Freundlich	$$q_e = K_f C_e^{\frac{1}{n}}$$ $$Linear\ form: \log(q_e) = \log(K_f) + \frac{1}{n}\log(C_e)$$	(5.3)

Dubinin-Radushkevich	$$q_e = q_m \exp\left(-\beta \varepsilon^2\right)$$ $$\varepsilon = RT ln(1 + \frac{1}{C_e})$$ *Linear form:* $\ln(q_e) = \ln(q_m) - \beta \varepsilon^2$	(5.4) (5.5)
Redlich-Peterson	$$q_e = \frac{K_R C_e}{1 + a_R C_e{}^\beta}$$	(5.6)

Ion exchange batch equilibria isotherms was modelled using various isotherm models including the Langmuir, Freundlich, Dubinin-Radushkevhich and Redlich-Peterson models. These isotherm models can help describe the resin properties and ion exchange mechanisms. A summary of the equations can be found in Table 5.1.

The Langmuir isotherm model is a model that assumes the adsorption occurs on a finite number of localized sites, the adsorption layer is a monolayer and the sites are all homogenous (Ayawei et al., 2017; Misak, 1993). Equation 2 represents the Langmuir model, where q_e (mg/g) is the ion concentration in the resin phase at equilibrium, C_e (mg/L) is the ion concentration on the solution phase at equilibrium, q_m (mg/g) is the maximum adsorption capacity and K_L (L/mg) is the Langmuir isotherm constant. When rearranged into a linearized format, Equation (5.2) above the constants K_L and q_m can be calculated by plotting C_e/q_e vs C_e (Alyüz & Veli, 2009).

The Freundlich Isotherm model is an empirical model which can be applied to multilayer adsorption, which bases its assumptions relating to the energetic surface heterogeneity (Appel, 1973). Where K_f (L/mg) is the Freundlich constant, which represents adsorption capacity and n is the empirical constant which represents adsorption capacity. The Freundlich isotherm constants K_f and n can be identified by linearizing Eequation (5.3) above and plotting *Ce* vs *ln(qe)* (A.O et al., 2012; Appel, 1973).

The Dubinin-Radushkevich isotherm model is an empirical model which was formulated for the adsorption process for a pore filling mechanism and is generally applied to express adsorption on both homogenous and heterogenous surfaces (Dawodu et al., 2012). Where β (mol^2 kJ^{-2}) is a constant related to the adsorption energy and ε (kJ mol^{-1}) is the adsorption potential. The adsorption energy found in Equation 5.4 where R (8.314 J/mol K) is the universal gas constant, and T (K) is the absolute temperature. The values of q_m and β can be found by linearizing the above Equation (5.4), and plotting $ln(q_e)$ vs ε^2 (A.O et al., 2012).

The Redlich-Peterson isotherm model is a three-parameter model, which combines both the Langmuir and Freundlich models, therefore the mechanism of adsorption is mixed and does not follow an ideal monolayer adsorption (Belhachemi & Addoun, 2011; Wu et al., 2010). Where K_R and a_R are the Redlich-Peterson isotherm constants (L/mg) and β is the exponent that lies between 0 and 1, for which when the value of β is equal to 1, the above Equation (5.6) reduces to the Langmuir model (Ayawei et al., 2017).

5.2.5.2. Kinetic models

Table 5.2. Kinetic model equations used in phosphate experiments

Model	Equation	
Intraparticle diffusion	$$q_t = k_i . t^{0.5} + \theta$$	(5.7)
Elovich	$$q_t = \left(\frac{1}{b}\right) ln(ab) + \left(\frac{1}{b}\right) ln\,(t)$$	(5.8)
First-order reversible	$$ln[1 - U(t)] = -kt$$ $$U(t) = \frac{C_{Ao} - C_A}{C_{Ao} - C_{Ae}}$$	(5.9) (5.10)

A summary of kinetic equations used can be found in Table 5.2. The intraparticle diffusion model was used to explore to possibility of the intraparticle diffusion mechanism within the resin (Pan et al., 2017; Sowmya & Meenakshi, 2013). Equation 5.7 where t (min) is the time, q_t (mg/g) is the amount adsorbed at time t, k_i (mg/(g.min$^{0.5}$)) is the intraparticle diffusion rate constant and θ (mg/g) is the constant related to the thickness of the boundary layer. The larger the value of θ, the greater the boundary layer. If a plot of q_t vs $t^{0.5}$ is a straight line, then the sorption process is controlled by intraparticle diffusion only. If the plot displays two or more linear plots then, two or more mechanisms affect the adsorption process (Zarrabi et al., 2014).

The Elovich model (Equation 5.8) is typically used to study the kinetics of chemisorption of gases on to a solid surface (Juang & Chen, 1997). Where q_t (mg/g) is the amount adsorbed at time t, a (mg/ (g.h)) is the initial adsorption rate and b (g/mg) is related the surface coverage and activation energy for chemisorption. The values of a and b can be calculated by plotting q_t vs $ln(t)$ (Cheung et al., 2000; Pan et al., 2017).

The first order reversible reaction model (Equation 5.9) is based on solution concentration, to determine the rates of reaction (Bhattacharya & Venkobachar, 1984), where U(t) is the fractional attainment of equilibrium, k (s^{-1}) is the overall rate constant, t (s) is time, C_{Ao} is the initial concentration of A in solution (mg/L), C_A is the concentration of A in solution at any time (mg/L) and C_{Ae} is the equilibrium concentration of A in solution (mg/L). By plotting ln[1-U(t)] vs t, the overall rate constant can be found (Bhattacharya & Venkobachar, 1984; Chabani et al., 2006).

The particle diffusion model (Equation 11) is based on the Nernst-Plank equation. The results of the model are expressed in terms of the fractional attainment of equilibrium $U(\tau)$ with τ being a dimensionless time parameter. α is the mobility ratio (D_a/D_b), r_o is the particle radius, D_a and D_b are the inter diffusion coefficients of ions a and b, respectively and t is time. The functions $f_1(\alpha)$, $f_2(\alpha)$ and $f_3(\alpha)$ are dependent on the mobility ratio, and thus have different equations (Khan & Khan, 2010; Plesset et al., 1958).

Table 5.3. Mathematical models of the breakthrough curves

Model	Equation	
Bohart-Adams	$$\frac{C_t}{C_o} = \frac{e^\alpha}{(e^\beta - 1 + e^\alpha)}$$	(5.11)
	$$\beta = \frac{k_{BA}\rho_P q_0 Z}{v}\left(\frac{1-\varepsilon}{\varepsilon}\right)$$	(5.12)
	$$\alpha = k_{BA} C_o\left(t - \frac{Z}{v}\right)$$	(5.13)
Thomas	$$\ln\left(\frac{C_o}{C_t} - 1\right) = \frac{k_{Th}q_{ads}m}{Q} - k_{Th}C_o t$$	(5.14)
Clark	$$ln\frac{C_t}{C_o} = \frac{1}{(1 + Ae^{-\theta t})^{1/n-1}}$$	(5.15)
	$$A = \left(\frac{C_o^{n-1}}{C_b^{n-1}} - 1\right)e^{\theta t_b}$$	(5.16)
B-A n Order	$$\frac{c}{c_0} = 1 \Big/ \left[1 + na_0^{1-n}c_0^{n-1}\left(\left[\frac{1 + (n-1)k_n a_0 c_0^{n-1}x}{1 + (n-1)k_n a_0^{n-1}c_0 t}\right]^{\frac{1}{n-1}} - \left[\frac{1}{1 + (n-1)k_n a_0^{n-1}c_0 t}\right]^{\frac{1}{n-1}}\right)^{\frac{1}{n}}\right]$$	(5.17)
B-A Fractal	$$\frac{c}{c_0} = \frac{\exp\left(\frac{1}{1-h}k_{BA,0}t^{1-h}c_0\right)}{\exp\left(\frac{k_{BA,0}t^h a_0 x}{u}\right) + \exp\left(\frac{1}{1-h}k_{BA,0}t^{1-h}c_0\right) - 1}$$	(5.18)

A summary of breakthrough equations used can be found in Table 5.3. Bohart-Adams model assumes that the rate of reaction is proportional to the fraction of the sorbent capacity remaining and the concentration of the sorbate in the solution phase (Bohart & Adams, 1920; Karpowicz et al., 1995). Neglecting axial dispersion, the model is represented in Equation 5.16, in which C_o and C_t are the influent and effluent concentrations of phosphate solute at time t (mg L^{-1}), k_{BA} is the Bohart-Adams constant (cm^3 mg^{-1} s^{-1}), ρ_P is the apparent adsorbent density (g cm^{-3}), q_o is the sorption capacity per unit mass of adsorbent (mg g^{-1}), Z is bed depth (cm), v is the interstitial velocity (cm s^{-1}) and ε is the column void fraction. The variables in the equation were calculated using Non-linear regression method.

The Thomas model is based on assumptions that the process follows a Langmuir isotherm with no axial dispersion and also assumes that the rate obeys that of a second-order reversible reaction kinetics (Thomas, 1944). Equation 5.19 where C_o and C_t are the influent and effluent concentrations of phosphate solute at time t (mg L^{-1}), m is the mass of adsorbent (g), Q is the volumetric flow rate (mL min^{-1}), k_{Th} is the Thomas rate constant (L mg^{-1} min^{-1}) and q_{ads} is the equilibrium uptake of phosphate per g of resin. By plotting t vs ln(C_o/C_t -1) a straight line is obtained which is used to calculate the variables k_{Th} and q_{ads}.

The Clark model assumes that the process follows a Freundlich isotherm and uses the mass transfer concept to predict the breakthrough (Clark, 1987; Hu et al., 2020). Equation 5.20 where k_{cl} and n are the mass transfer coefficient (1/min) and Freundlich constant, which was determined earlier during the batch isotherm experiments. t_b and C_b are the time and outlet concentration of at breakthrough point.

The last two models used were modified Bohart-Adams models, the n order B-A and Fractal B-A models (Equation 5.22 and 5.23), respectively. Breakthrough curves are often asymmetric for the adsorption of contaminants in water, even for single solutes. In order to describe asymmetric breakthrough curves, modified versions of the Bohart-Adams model were used. For the n- order model, it is assumed that the rate of reaction is proportional to n-power of the concentration

of the adsorbate and that of the residual capacity. The fractal model is based on the interaction of energetic and geometric heterogeneity which leads to a fractal like kinetics (Hu et al., 2021).

5.3. Results and discussion
5.3.1. Resin properties

The particle size distribution of the dry FerrIX A33E resin was determined by passing a representative sample through a series of standard sieves. Figure 5.2 (a) shows the percent of the sample retained by the specified sieves and 5.2 (b) the cryogenic nitrogen adsorption/desorption isotherms. The data matches with the data provided by the manufacturer which presents particle size range between 0.3 – 1.2 mm. The uniformity coefficient of the resin, d_{60}/d_{10}, was found equal to 1.36, indicating that the resin particles have unform sizes as also observed by the
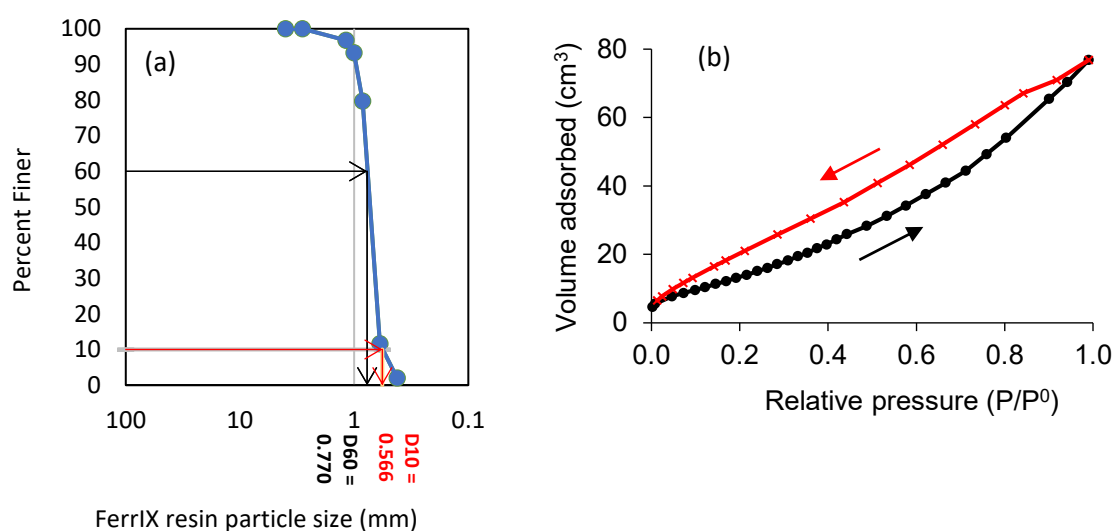
Figure 5.2. (a) FerrIX A33E resin particle size distribution; (b) cryogenic nitrogen adsorption/desorption isotherms on FerrIX A33E resin

microscopic images (Appendices B).

The A400 resin provided by Purolite, is a polystyrenic gel, strong base anion resin, typically used in the industrial water for demineralization. Visually, the resin is visually takes the form of faded yellow spherical beads. Its , with a particle size that ranges from 300 to - 1200 μm and its total capacity of is 1.3 eq/L, according to the Purolite data sheet (Purolite, 2024).

5.3.2. Silica removal isotherm experiments

Batch equilibria experiments of silica onto FerrIX and A400 resin was were conducted. The experimental data was then modelled to using the various isotherm models including Langmuir, Freundlich, Dubinin-Radushkevich and Redlich-Peterson models. A summary of each model is can be found in Table 5.1. Isotherms help describe the capacity of interaction between liquid and solid phases in the ion exchange system. Results of the models for A400 (OH$^-$ form), FerrIX (Cl$^-$ form) and FerrIX (OH$^-$ form) are presented in Figure 5.3 (a), (b) and (c) and model parameter values in Table 5.4, respectively.

Figure 5.3 (a) A400 (OH$^-$ form) shows that Langmuir (R^2=0.99) model had the best fit. The Langmuir model assumes that the adsorption occurs at specific homogenous sites within the adsorbent, that forms a monolayer. This suggests no multilayer or complex surface interactions are occurring with the gel A400 anion exchange resin, with a finite number of exchanging sites. The maximum adsorption capacity calculated by the Langmuir model was 107.5 mg/g, indicating a significant capacity to adsorb the solute. The Redlich-Peterson also fits well the experimental data (R^2=0.96), suggesting that while the primary mechanism could be monolayer adsorption, there may still be some heterogenous adsorption sites. The poor fit of the Freundlich model (R^2=0.57) may indicate that the resin is not heterogeneous. Poor fitting of the D-R model (R^2=0.44) demonstrates that micropore filling is not a dominant mechanism. The Freundlich and D-R models predicted the uptake at low equilibrium concentration (C$_e$ < 20 mg/L), however, deviates at higher concentrations.

Figure 5.3 (b) for the FerrIX resin (Cl$^-$ form) shows the best fit with Freundlich (R^2=0.99) and Redlich-Peterson (R^2=0.99) isotherms. Freundlich isotherm signifies a heterogenous sites within the adsorbent, evidencing that the iron particles impregnated in the resin introduces additional adsorption mechanisms other than ion exchange, such as surface complexation and physical adsorption sites. The Freundlich models n value of 5.52, which indicates a strong adsorption favourable at high concentrations. The Redlich-Peterson model provides a particularly good fit, indicating that the adsorption process combines

characteristics of both the Langmuir model's monolayer adsorption and the Freundlich model's heterogeneity, making it highly versatile for adsorbing different solutes.

Figure 5.3 (c) displays the FerrIX resin (OH$^-$ form), Langmuir model provides a good fit (R^2 = 0.94), demonstrating that a significant portion of the adsorption process follows monolayer adsorption, with a moderate adsorption capacity of 50.25 mg/g. The fit of the Freundlich model is also strong (R^2 = 0.92), suggesting that heterogeneous adsorption sites are present, although the heterogeneity is less pronounced compared to FerrIX (Cl$^-$ form) since the n value (2.191) is much lower than that of FerrIX (Cl$^-$ form).

Overall, the A400 gel resin has a much higher capacity compared to the macro porous FerrIX resin. A400 (OH⁻ form) shows strong monolayer adsorption on a relatively homogeneous surface, with a high adsorption capacity. FerrIX in the hydroxide form has a higher capacity than the chloride form.
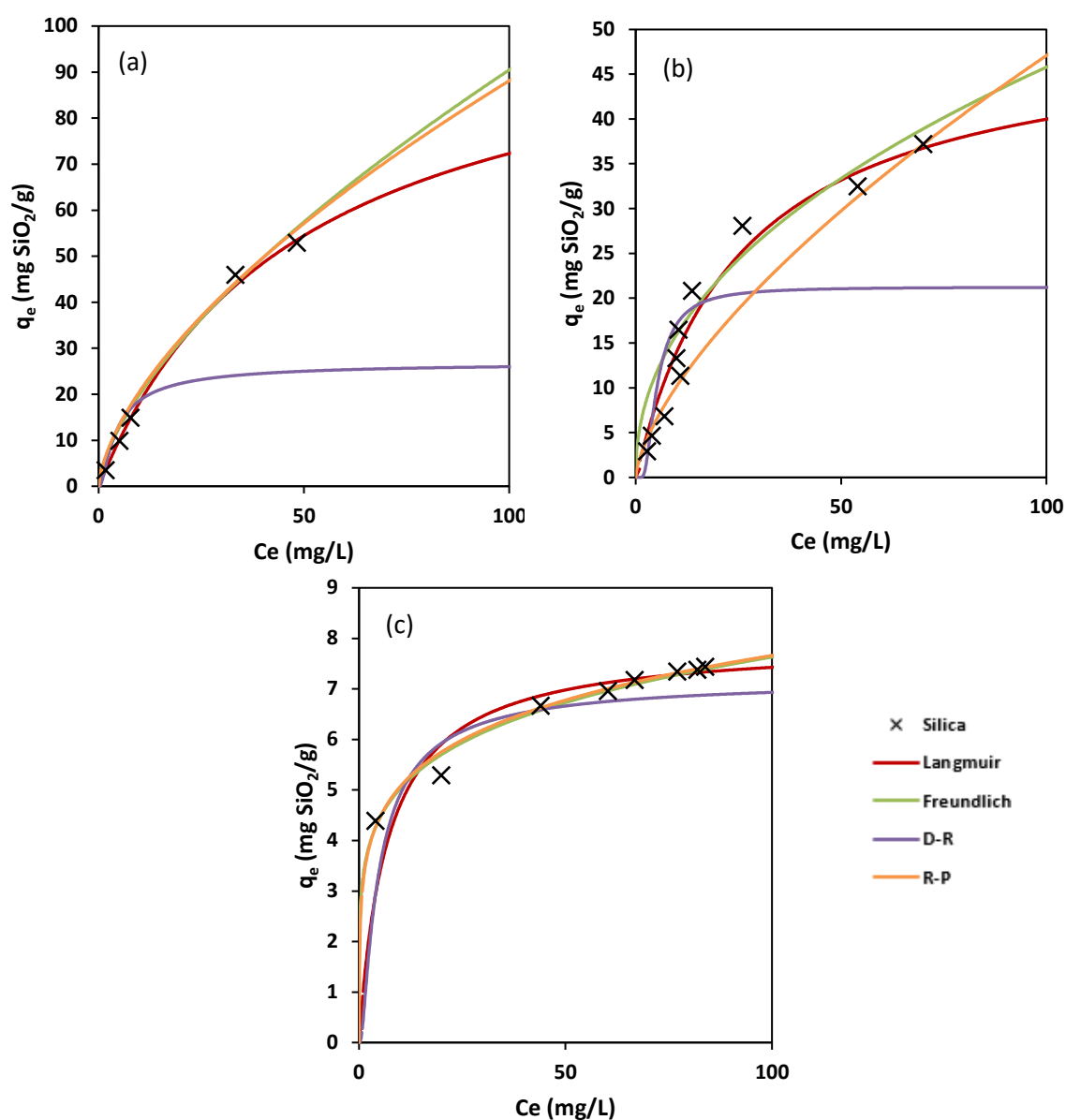

Figure 5.3. Isotherm models of silica for (a) A400 resin (hydroxide form) (b) FerrIX resin (hydroxide form) and (c) FerrIX resin (chloride form)

Table 5.4. Isotherm model parameters

Resin	Model	Model parameters	R^2
A400 (OH⁻ Form)	Langmuir	q_{max} = 107.5 mg/g ; K_L=0.021	0.98
	Freundlich	K_F=2.50 (L/mg) ; n = 1.21	0.57
	D-R	β=1.69 (mol²/kJ²) ; q_m=32.3 (mg/g)	0.44
	R-P	K_R = 1231 (L/mg) ; a_R=257 (L^β/mg^β) ; β=0.36 (-)	0.96
FerrIX (Cl- form)	Langmuir	q_{max} = 7.93 mg/g ; K_L=0.15	0.98
	Freundlich	K_F= 3.31 (L/mg) ; n = 5.52	0.99
	D-R	β=1.62 (mol²/kJ²) ; q_m=7.21 (mg/g)	0.97
	R-P	K_R = 1091 (L/mg) ; a_R=327.5 (L^β/mg^β) ; β=0.81 (-)	0.99
FerrIX (OH- form)	Langmuir	q_{max} = 50.25 mg/g ; K_L=0.039	0.94
	Freundlich	K_F=5.6 (L/mg) ; n = 2.191	0.92
	D-R	β=3.86 (mol²/kJ²) ; q_m=21.25 (mg/g)	0.76
	R-P	K_R = 41.97 (L/mg) ; a_R=19.9 (L^β/mg^β) ; β=0.32 (-)	0.42

5.3.3. Silica removal in fixed bed columns

5.3.3.1. Kinetic models

The kinetics of silica removal in fixed beds of FerrIX resin in both chloride and hydroxide forms were determined. Integration of the area under the breakthrough curves gives the amount of silica adsorbed onto the resin at a given time, *t*. Figure 5.4 and 5.5 (a), (b) and (c) shows the kinetics of adsorption for FerrIX in the chloride and hydroxide form, respectively. The results were modelled using various kinetic models including Intraparticle, Elovich and First-order reversible models. The equations of these models are summarised in Table 5.2. The results showed that the adsorption kinetics was much faster at high concentrations (300 mg/L) compared to lower (100 mg/L). To uptake (q_e) 10 mg/g of silica took 20 minutes at inlet concentration of C_o of 300 mg/L, whereas the same amount took 190 minutes for C_o 100 mg/L.

Figure 5.4 (b) and (c) shows the results when the bed height was increased while C_o and flowrate was kept at 100 mg/L and 60 mL/min, respectively. By increasing the bed height, the empty bed contact time (EBCT) was increased from 0.6 to 1 minute. Figure 5.4 (a) shows that at high concentrations the intraparticle kinetics model had the best fit. The first order reversible model had a good fit initially, however, deviates from the data after ~20 minutes. The first order reversible model typically governs the initial stage of adsorption from the bulk solution to the external surface of the adsorbent. At later stages, intraparticle diffusion becomes important as the external surface of the adsorbent is saturated. Both model fittings also indicate the heterogenous nature of the adsorbent, with the iron nanoparticles playing a significant role in the adsorption process.

Fig 5.4 (b), when the concentration was decreased, showed Elovlich had the best fit, in which the Elovlich is typically used to describe chemisorption, where the rate of adsorption decreases over time due to surface heterogeneity or a decrease in active sites available.

Fig 5.5 (c), showed interesting results. Intraparticle model had the best fit initially, however, after 50 minutes, the experimental data followed the first order reversible model. When EBCT is increased, the adsorbent had more time to interact with the adsorbates, leading to intraparticle diffusion becoming the dominant rate-limiting step. Additionally, increasing the EBCT typically results in a reduced concentration gradient, as more adsorbate is removed by the adsorbent, and as more adsorbate is removed, the lower the gradient of concentration. This could be due to it accounting for surface heterogeneity and its flexibility and adapting of either film diffusion or particle diffusion rate limiting steps.

Figure 5.4. Kinetic models of silica for FerrIX resin (chloride form) for (a) z=5 cm, C_0 =300 mg/L, (b) z=5 cm, C_0 =100 mg/L and (c) z=15 cm, C_0 =100 mg/L

Figure 5.5 (a), (b) and (c) shows the kinetic results of the FerrIX resin in the hydroxide form. Overall, it was determined that the adsorption kinetics of the hydroxide form was much faster compared to the chloride form. Fig 5.5 (a) At high concentrations, the first order reversible model had the best fit. This could be due to the size of the hydroxide ions, which are more mobile compared to the chloride ions in Fig 5.4 (a) (intraparticle model).

The first-order reversible models are often more suitable for describing adsorption kinetics at high concentrations due to the dominance of film diffusion. At high concentrations, the concentration gradient between the bulk fluid and the adsorbent surface is more pronounced. This leads to a higher driving force for mass transfer across the external boundary layer, making film diffusion the dominant rate-limiting step. At reduced concentrations, again, the first order reversible model had the best fit, unlike the chloride form. In this case, film diffusion could become the dominant rate-limiting step. Fig 5.5 (c), showed that when EBCT was increased, first order reversible model again had the best fit.
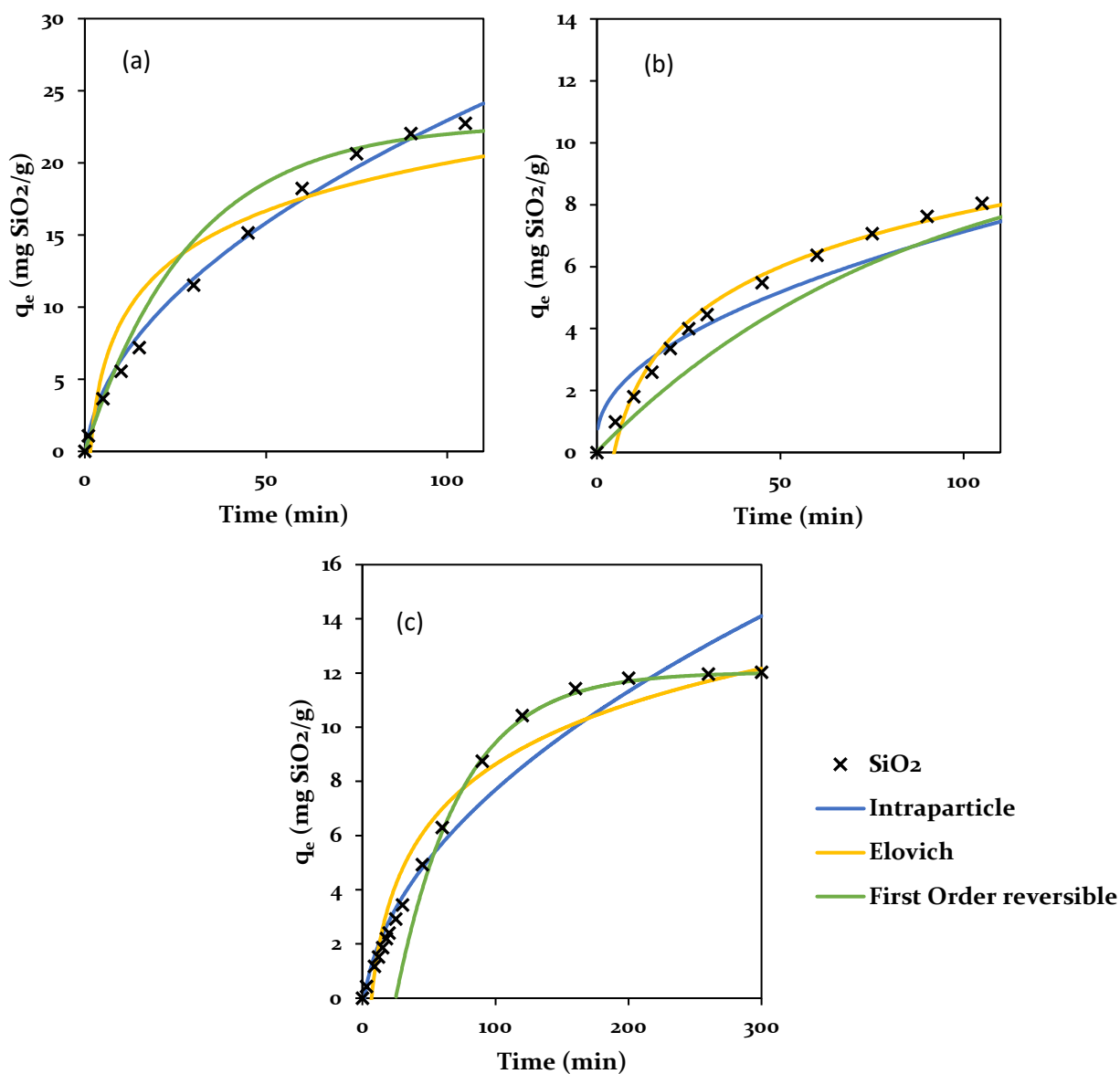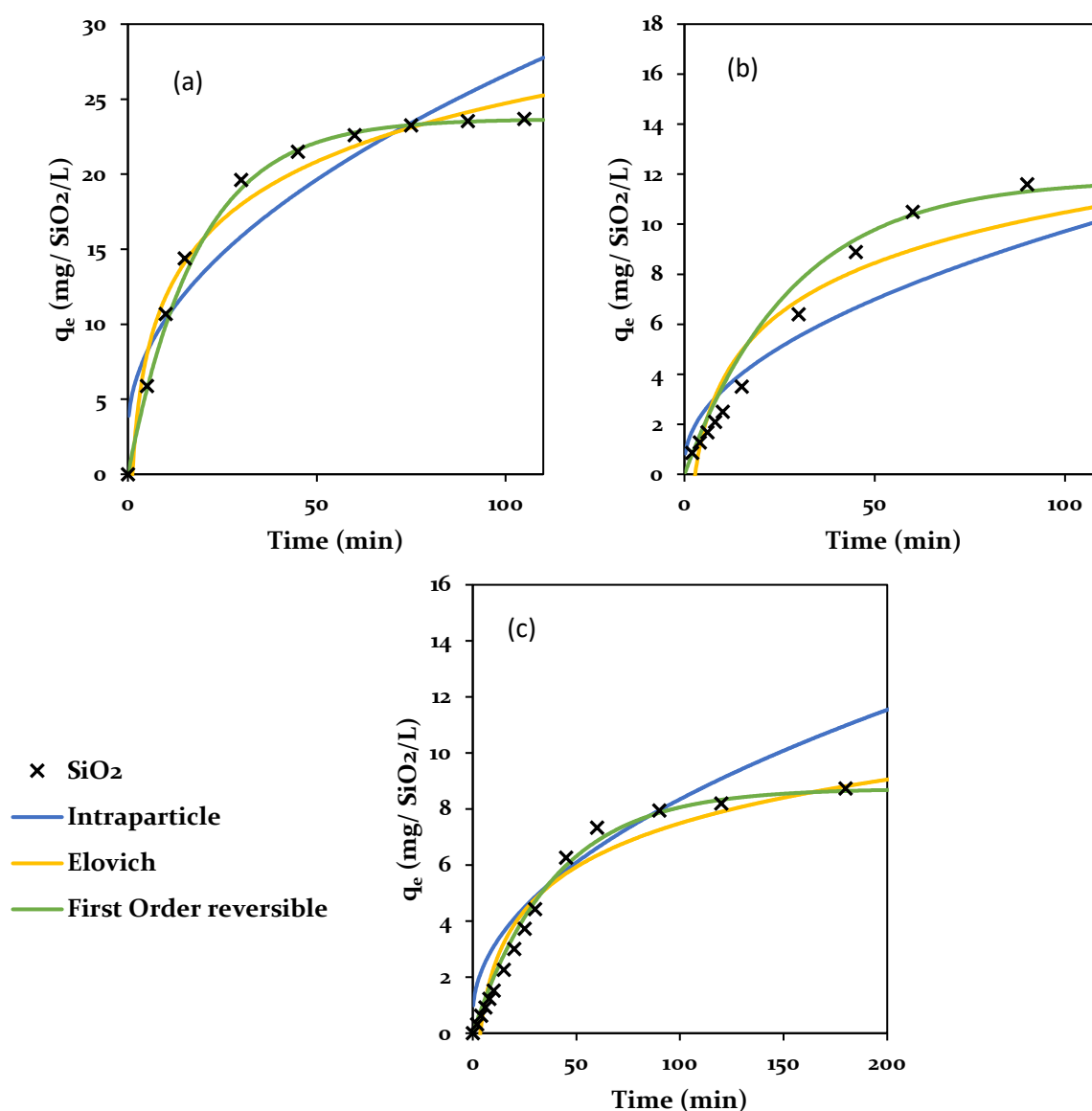

Figure 5.5. Kinetic models of silica for FerrIX resin (hydroxide form) for (a) z=5 cm, C_0 =300 mg/L, (b) z=5 cm, C_0 =100 mg/L and (c) z=15 cm, C_0 =100 mg/L
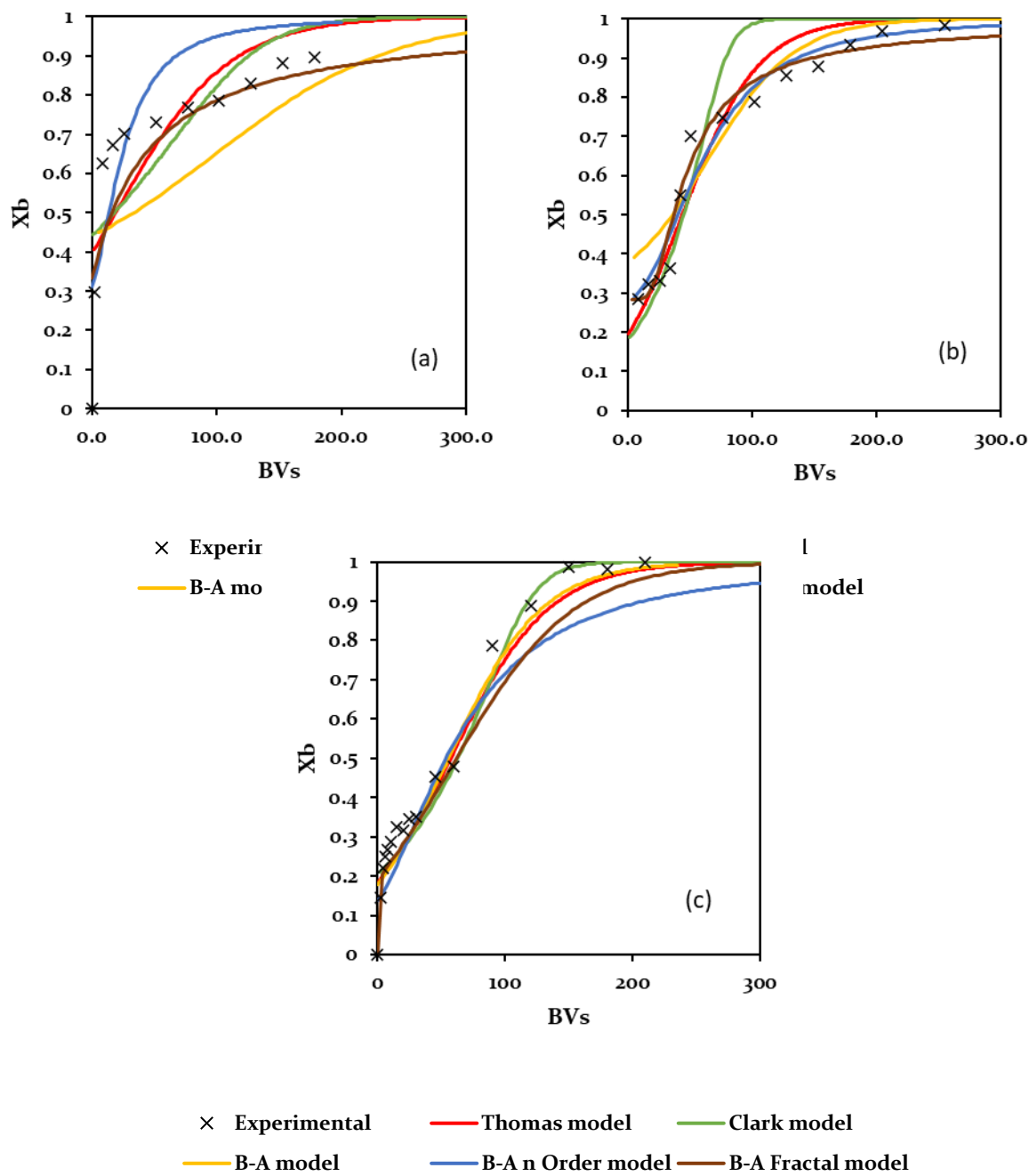
Figure 5.6. Breakthrough models of silica for FerrIX resin (chloride form) for (a) z=5 cm, C_0 =300 mg/L, (b) z=5 cm, C_0 =100 mg/L and (c) z=15 cm, C_0 =100 mg/L
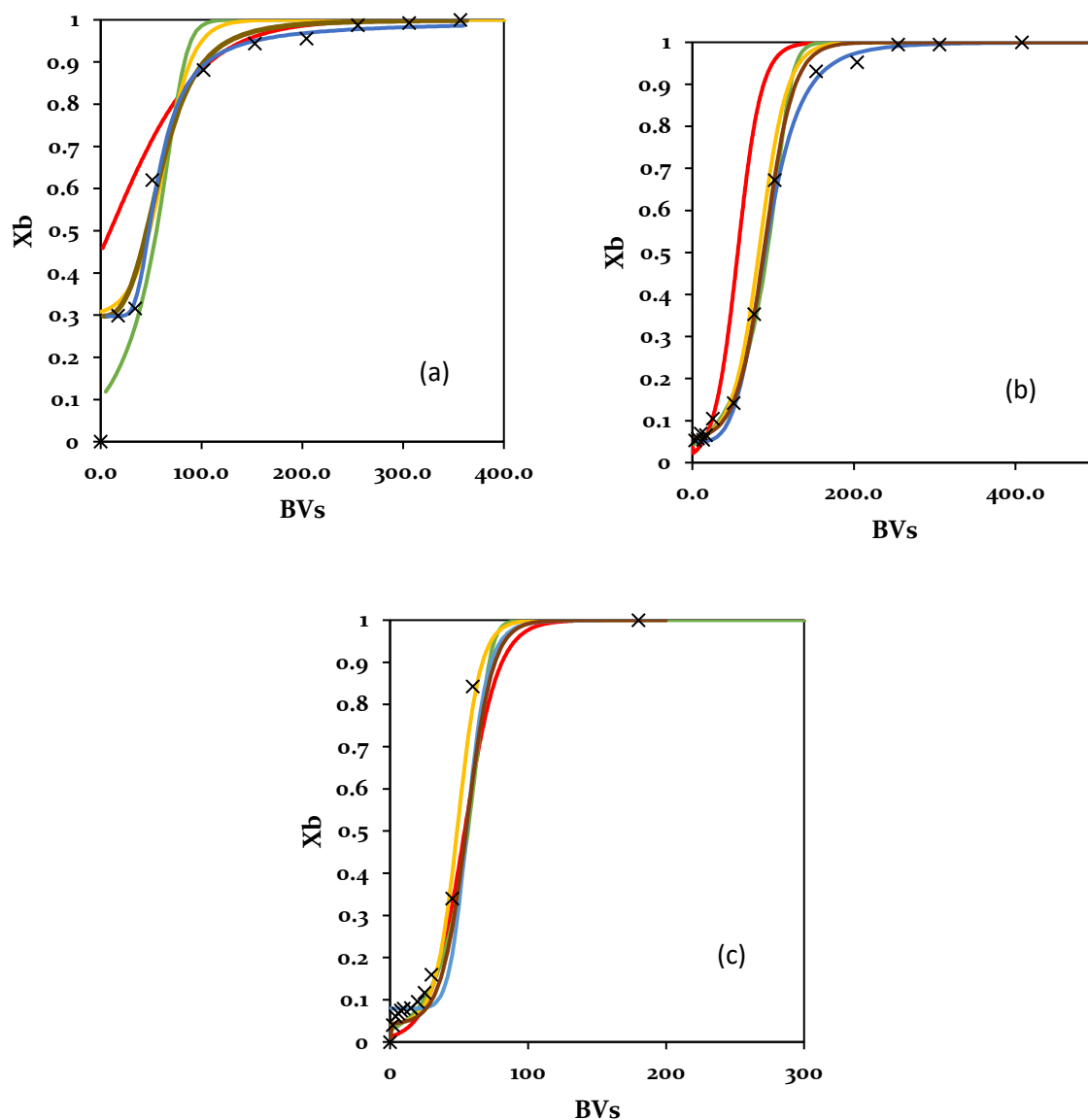
The successful design of an ion exchange column requires precise predictions of the breakthrough of the contaminant effluent occurring during the operation at a given time. Thus, the uptake of silica by the resin FerrIX A33E was studied in column settings and the results are presented in the form of breakthrough curves (Figures 5.6 and 5.7). In these curves, the ratio of effluent to influent silica concentrations in solution ($x_b = C_{eff}/C_{inlet}$) versus time (t) was plotted. The parameters that were adjusted to study their effects on the breakthrough curves

included the height of the bed, the inlet flowrate, and the concentration of silica of the inlet solution (C_{inlet}). The breakthrough curves were then modelled using the Bohart-Adams, Thomas, Clark and two versions of a modified Bohart-Adams model, which included the n-order and fractal B-A models respectively. The kinetic models used earlier describe the adsorption rate and mechanism over, typically in batch systems. The breakthrough models are used in continuous systems for column studies, used to describe how an adsorbate moves through a fixed bed. A summary of the breakthrough curve model parameters is presented in Table 5.5.

Figures 5.6 and 5.7 (a), (b) and (c) represent the breakthrough curve of the FerrIX resin in the chloride and hydroxide form, respectively. Figure 5.6 (a) represents high concentration (300 mg/L) at 5 cm bed height, Figure 5.6 (b) is low concentration (100 mg/L) at 5 cm bed height and Figure 5.6 (c) is low concentration at 15 cm bed height.

The models at high concentrations struggled to predict the experimental data when resin was in the chloride form. Breakthrough curve models are used to describe the adsorption process in fixed bed columns. However, these models have assumptions and limitations making them less effective at predicting breakthrough behaviour under certain conditions such as high concentrations. When the resin was in the hydroxide form, the models predicted well the experimental data, with B-A n order and B-A fractal models having the best fit. This could be due to the fact that the kinetics, as demonstrated earlier, was faster compared to the chloride form. This is due to the hydroxide ion having a lower affinity, smaller size and better diffusion properties.

All breakthrough curve models showed a better fit when the concentrations were reduced, reflecting improved alignment with their underlying assumptions. However, even at lower concentrations, the chloride form of the ion exchange resin continued to exhibit poorer performance compared to the hydroxide form. This discrepancy is likely due to the larger size and stronger hydration of chloride ions, which slow down the ion exchange process and introduce greater mass transfer resistance (Yu et al., 2023). In contrast, the smaller and less hydrated

hydroxide ions maintained faster diffusion and exchange rates, leading to more predictable behaviour that more closely followed the model assumptions.

Thomas model

The Thomas model provides insights into the adsorption kinetics and capacity through its rate constant K_{TH} and maximum adsorption capacity Q_o. For Cl^- resin, the highest K_{TH} value (6.81×10^{-4} L/mg/min) was observed at an conditions of 100 mg/L and a bed height of 5 cm, indicating fast adsorption kinetics under these conditions. In comparison, OH^- resin exhibited an even higher rate constant (9.19×10^{-4} L/mg/min) at the same initial concentration but with a bed height of 15 cm, highlighting the resin's boosted adsorption kinetics when the solute had more time to interact with the resin due to the increased bed height.

The Thomas model showed that for all 3 conditions, the rate constant was greater with the hydroxide form. This indicates that OH^- resin adsorbs solute faster than Cl^- resin, especially at lower concentrations and higher bed heights. The maximum adsorption capacity for the Thomas model indicated that at higher concentrations, the resin could adsorb more solute (Q_o = 15.39 Cl^- form, Q_o = 12.30 OH^- form).

The R^2 values for the Thomas model ranged from 0.77 to 0.99, indicating a generally good fit between the experimental data and the model predictions. The lower R^2 values were observed at higher initial concentrations, likely due to limitations of the model at high solute loads.

Clark Model

The Clark model showed a substantially higher A value, for the hydroxide form of the resin when compared to chloride, which indicates a much higher adsorption potential for the hydroxide form. This suggests that OH^- resin can achieve a higher degree of adsorption under the same conditions. The adsorption rate constant *r* was generally higher for OH^- resin at bed hight of 15 cm and C_o=100 mg/L (r=0.26) meaning adsorption occurs faster with a longer bed height.

Conversely, for Cl⁻ resin under the same conditions *r* was much lower (r=0.06), indicating slower adsorption.

R^2 values for the Clark model ranged from 0.82 to 0.97, again indicating a good fit for most of the experimental conditions. The best fits were observed for OH⁻ resin, indicating that the Clark model may better describe the kinetics of OH⁻ resin in these systems.

Bohart-Adams

The Bohart-Adams model provides a further insight into the adsorption process through the rate constant K_{BA} and adsorption capacity Q_o. The highest rate constant was (K_{BA} = 0.020 L/mg/min) was recorded for OH⁻ resin at bed height of 15 cm and C_o of 100 mg/L. These results line up with findings of the Thomas and Clark model regarding the faster kinetics of the OH- form resin.

The R^2 values for the Bohart-Adams model were lower compared to the Thomas and Clark models, ranging from 0.49 to 0.96, indicating that the fit was not as strong in some conditions. The lower R^2 values suggest that this model may not fully capture the complexity of the system, particularly at higher solute concentrations.

B-A n order

The analysis of the data in relation to the n-order Bohart-Adams model reveals that it provides an improved fit for asymmetric breakthrough curves compared to the traditional Bohart-Adams model. The model's flexibility, provided by the adjustable reaction order *n*, allows it to account for complex adsorption behaviours such as non-linear decay in both adsorbate concentration and adsorbent capacity. The reaction order *n* was also higher for Cl⁻ resins compared to OH⁻, under the same conditions, indicating non-linear adsorption kinetics. For OH⁻ resin, k_n and *n* values were generally lower, indicating simpler kinetics.

The lower *n* values for OH⁻ resin suggest that the adsorption process for OH⁻ resin follows closer to first-order kinetics.

B-A Fractal

Fractal Bohart-Adams model demonstrated the model's robustness in capturing the complex, diffusion-limited adsorption behaviours on heterogeneous surfaces. The fractal Bohart-Adams model performed especially well in cases where diffusion played a significant role in the adsorption process. For example, in the condition of 100 mg/L, OH⁻ resin, and 15 cm bed height, the model yielded an R^2=0.89 with a small fractal exponent h=0.02, indicating that diffusion was a controlling factor, and the adsorbent surface exhibited substantial heterogeneity. The rate constant k_{BA} was highest for OH⁻ resin (12.00 L mg⁻¹ min⁻¹) at C_0=300 mg/L, indicating fast adsorption kinetics on this relatively simple surface. For Cl⁻ resin, the k_{BA} values were lower, suggesting slower adsorption (Anbazhagan et al., 2021).

Table 5.5. Breakthrough model parameters for silica removal

Conditions				Thomas Model			Clark Model			Bohart Adams			B-A n order				B-A Fractal			
C_o (mg/L)	Q (mL/min)	Resin form	Z (cm)	KTH (L/mg/min)	Q_o (mg/g)	R_2	A (-)	r (min-1)	R_2	KBA	Q_o	R_2	k_n (Ln mg-nmin-1)	a_o (mg/L)	n (-)	R_2	k_{BA} (L mg-1 min(h-1))	a_o (mg L-1)	h (-)	R_2
300	60	Cl-	5	1.26×10^{-4}	15.39	0.77	345.54	0.36	0.98	0.0023	62.00	0.49	5.9×10^{-8}	3.57×10^8	1.48	0.49	3.1×10^{-6}	3.11×10^6	0.48	0.49
100	60	Cl-	5	5.75×10^{-4}	5.78	0.93	2497.99	0.18	0.82	0.013	10.93	0.62	4.9×10^{-2}	8.37×10^6	1.42	0.60	2.5×10^1	7.13×10^1	0.99	0.60
100	60	Cl-	15	2.95×10^{-4}	7.80	0.96	1285.94	0.06	0.91	0.0045	16.90	0.96	66.0	5.74×10^6	1.52	0.86	2.7×10^{-4}	1.66×10^4	0.02	0.86
300	60	OH-	5	6.49×10^{-4}	12.30	0.96	2.94×10^4	0.55	0.94	0.015	25.60	0.62	5.0×10^{-2}	3.91×10^5	1.28	0.62	1.2×10^1	2.71×10^1	1.00	0.62
100	60	OH-	5	6.81×10^{-4}	9.00	0.99	1.84×10^6	0.21	0.93	0.015	41.97	0.90	5.2×10^{-2}	1.38×10^5	1.22	0.88	1.4×10^{-3}	1.85×10^4	0.10	0.88
100	60	OH-	15	9.19×10^{-4}	7.35	0.95	9.53×10^6	0.26	0.97	0.020	12.61	0.87	66.0	2.38×10^4	1.12	0.89	1.2×10^{-3}	1.25×10^4	0.00	0.89

5.3.4. Effect of multicomponent on ion exchange

5.3.4.1. Isotherms

The efficiency of an ion exchange system depends on several factors such as the exchange capacity, amount of ion exchange resin, contact time, concentration of counterion and more. An important aspect in understanding the ion exchange process is the impact of competing ions, which are known to reduce the effective
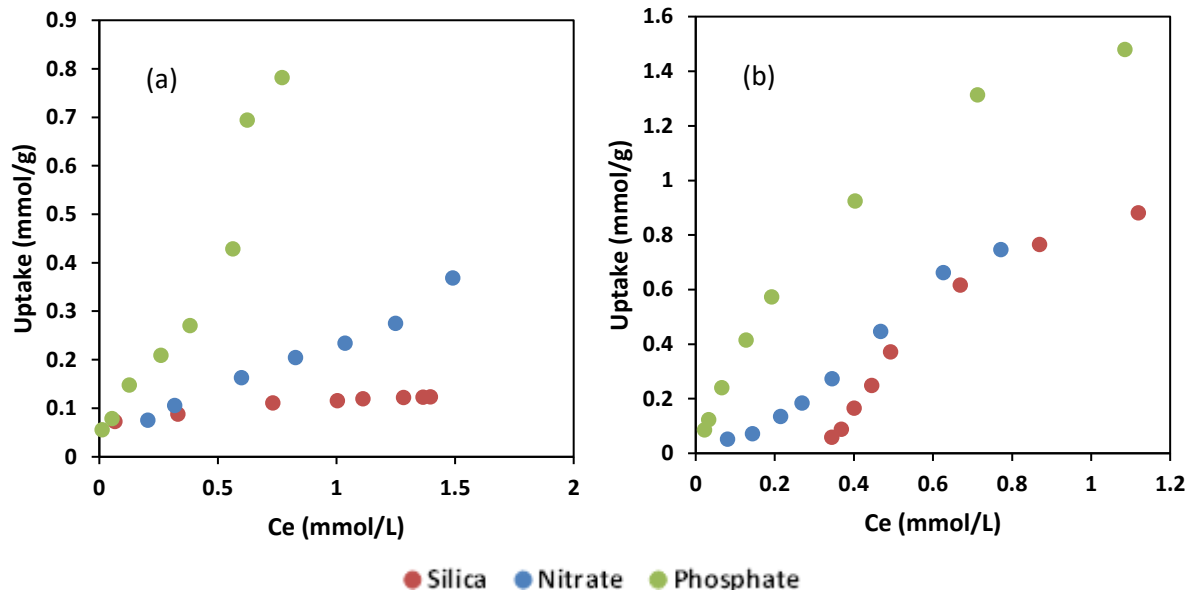

Figure 5.9. Individual isotherm of silica, nitrate and phosphate for (a) FerrIX (b) A400
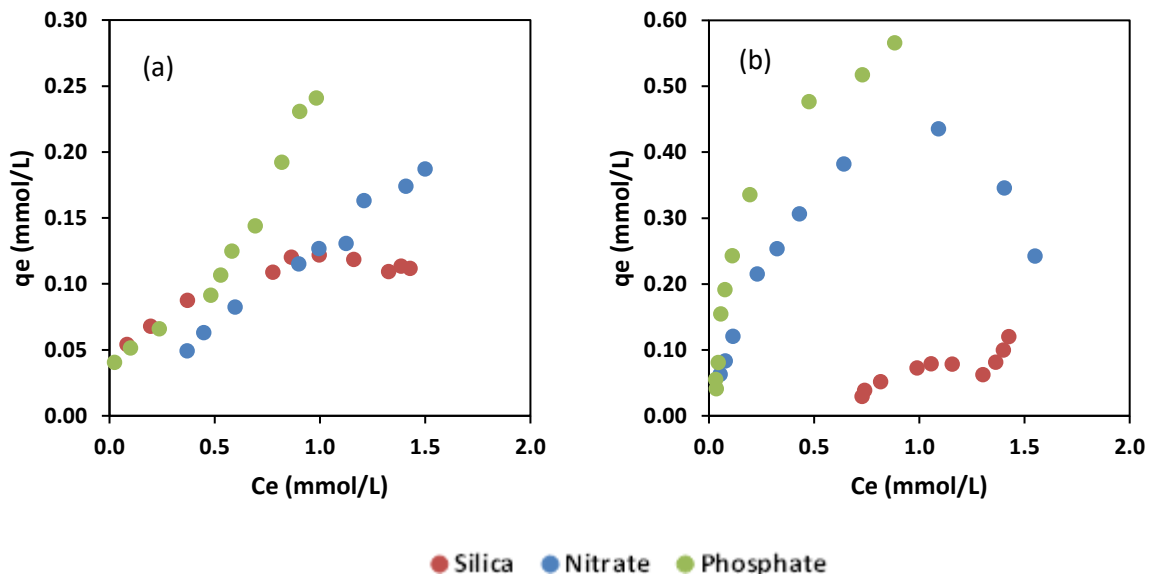

Figure 5.10. Multicomponent isotherms of silica, nitrate and phosphate for (a) FerrIX (b) A400

capacity of the resin. The capacity of silica, in a multicomponent system dramatically decreases compared to a mono component system, as seen in Figures 5.9 and 5.10, for the FerrIX A33E resin and A400 resin. For all isotherms, the initial concentrations of silica, nitrate and phosphate were 1.7, 1.6 and 1.1 mmol/L.

Figure 5.9 (a) adsorption isotherm results of the FerrIX showed that phosphate had the highest uptake among all 3 species, with a maximum adsorption capacity of 0.8 mmol/g. Adsorption increased linearly at low concentrations to level off at high concentrations, suggesting saturation of available adsorption sites. Nitrate uptake had a similar pattern, with lower maximum adsorption capacity (0.4 mmol/g). The nitrate isotherm indicated moderate affinity for nitrate, but lower than that of phosphate. Silica exhibited the lowest adsorption capacity, at <0.2 mmol/g across the concentrations.

Figure 5.9(b) showed a similar trend to that of the A400 resin, with phosphate having a maximum adsorption capacity of 1.4 mmol/g, significantly higher than FerrIX resin. The nitrate adsorption capacity reached a maximum of 0.8 mmol/g. As with the FerrIX resin, silica showed the lowest adsorption capacity at low equilibrium concentrations. However, at higher concentrations, silica showed higher adsorption than nitrate. The uptake of silica did not start occurring until concentrations above 0.2 mmol/L. With the FerrIX adsorption of silica occurred at lower concentrations (0.02 mmol/L).

Figure 5.10(a) and (b) depict and provide insight to the multicomponent competitive adsorption isotherms for FerrIX and A400. In the multicomponent system, the adsorption capacity of phosphate on FerrIX is reduced compared to the single-component system. The maximum uptake of phosphate in the presence of competing ions is approximately 0.25 mmol/g, suggesting that competitive effects from nitrate and silica significantly inhibit phosphate adsorption. Similar trend was observed with nitrate (0.15 mmol/g) indicating the presence of competitive ions, which limits the availability of adsorption sites for nitrate and phosphate. Silica uptake remains relatively constant in the multicomponent system, with a maximum capacity of around 0.1 mmol/g.

In the multicomponent system for A400 (Figure 5.10(b)), phosphate again exhibits the highest uptake, with a maximum of around 0.5 mmol/g. However, similar to FerrIX, the presence of competing ions leads to a reduction in phosphate adsorption compared to the single-component system. This reduction is less pronounced for A400, suggesting that A400 may have better resistance to competitive effects than FerrIX for phosphate removal.

5.3.5. Breakthrough curves

Figure 5.11 (a) displays the breakthrough curves of phosphate and silica as mono component systems and (b) as a two- component system, with the FerrIX A33E resin. Both breakthrough curves were set at bed height of 10cm, flowrate of 60 mL/min and concentration of silica and phosphate of 150 mg/L and 100 mg/L, respectively. From Figure 5.11 (a) the breakthrough fraction of 0.5 of silica, occurs at around 15-18 minutes, whereas for phosphate it occurs at around the 20-25 minute mark. Comparing the two- component system shows that silica breakthrough fraction of 0.5 occurs much quicker between 2-3 minutes, whereas phosphate breakthrough occurs again at around 20-25 minutes.

These results show that competing ions in mixtures, drastically reduce the ion exchange capability in removing silica, in terms of selectivity and capacity. Ion exchange resin such as the FerrIX A33E, which has the inclusion of ferric, have shown to increase selectivity of phosphate due to strong ligand attractions which can form inner sphere complexes through Lewis-acid base and electrostatic interaction (An et al., 2014; Pan et al., 2009). Being able to reduce the competing ions, such as phosphate, may allow enhanced silica removal via ion exchange in

the anion exchanger and condensate polishing stages of the water treatment process.
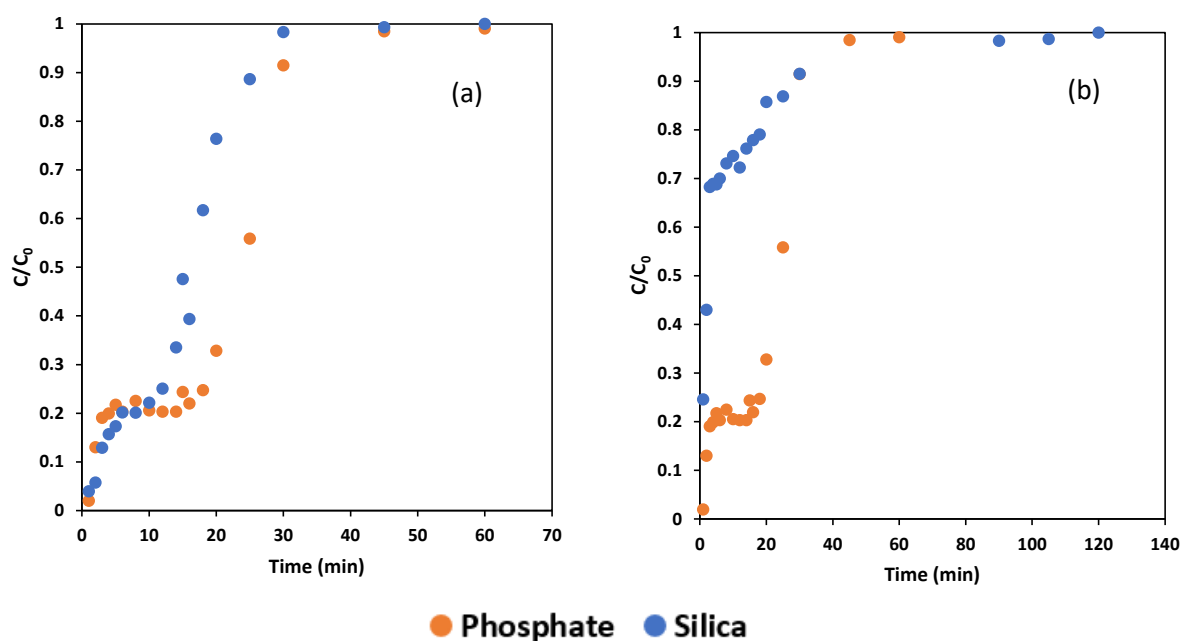

Figure 5.11. (a) Individual and (b) multicomponent breakthroughs of phosphate and silica

Following the observation that phosphate exhibited a strong affinity for FerrIX resin in both the equilibrium and kinetic studies, further experiments were designed to explore the possibility of selectively removing phosphate using FerrIX, thereby reducing the competition for adsorption sites in a mixed-ion system. The goal of these experiments was to enhance the adsorption of silica on A400 by first pre-removing phosphate, which had previously shown to dominate the adsorption process and limit silica uptake. By selectively adsorbing and removing phosphate with FerrIX, it was hypothesized that the available sites on A400 would be less competitive, allowing for an increased adsorption of silica. This approach aimed to optimize the use of both resins for improved contaminant ions removal efficiency, potentially creating a sequential treatment process that maximizes silica uptake after phosphate is removed.

5.3.6. Assessing the performance of FerrIX A33E in removing phosphate
5.3.6.1. Adsorption isotherms

Batch ion exchange equilibria experiments of phosphate onto the FerrIX A33E resin was conducted. The experimental data was then modelled to various

isotherm models including the Langmuir, Freundlich, Modified Langmuir, Dubinin-Radushkevich and Redlich-Peterson models. Isotherms help describe the capacity of interaction between liquid and solid phases in the ion exchange system.

As presented by Figure 5.12, the Freundlich and Redlich-Peterson models fit the experimental data best. Models such as the Freundlich, assumes that adsorption takes place on a heterogenous surface, which can be used for multilayer adsorption. The heterogeneity of the ion exchange resin could arise from the presence of iron and other contaminants on the resin. The Redlich-Peterson isotherm presents a unique approach to adsorption, blending elements from both the Langmuir and Freundlich isotherms. Consequently, its adsorption mechanism deviates from the ideal monolayer characteristics typically observed. Langmuir model assumes that adsorption occurs at specific binding sites that are localised on the adsorbent surface and that all sites are identical. Dubinin-Radushkevich models the mechanism of adsorption as the filling of pores.
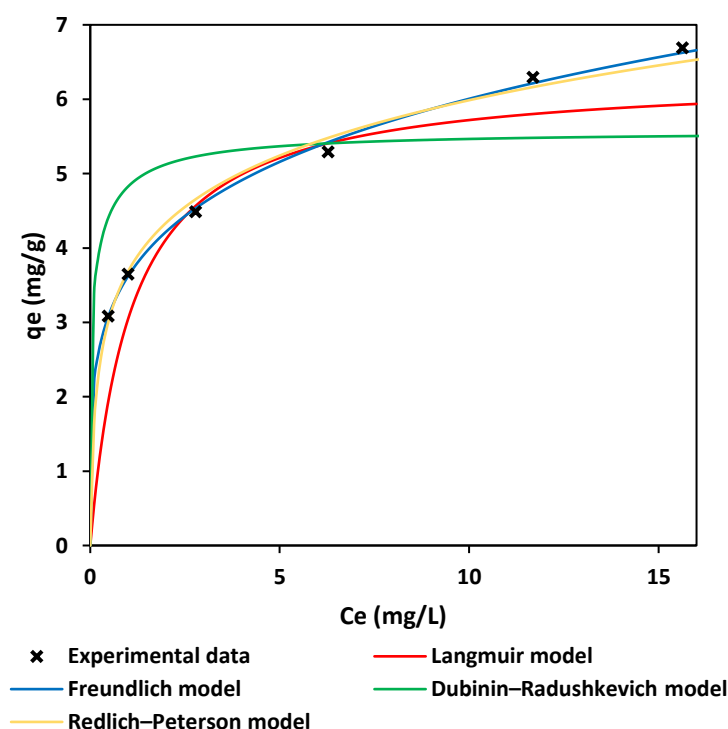

Figure 5.12. Isotherm models for the adsorption of phosphate onto FerrIX A33E resin (T=20ºC)

The results suggest that the adsorption mechanism is unique and does not follow the ideal monolayer adsorption characteristics expected from ion exchange. This could be due to the presence of ferric nanoparticles within the resin. As mentioned earlier, the removal of phosphate with the FerrIX A33E can also occur due to complexation of phosphates on iron oxide nanoparticles. This means that in addition to ion exchange mechanisms via quaternary amine groups, selective sorption/complexation by ferric oxides also play a key role in adsorption mechanisms. Equations (5.19) and (5.20), describe the ion exchange mechanism, whereas, equations (5.21) and (5.22) describe the sorption/complexation.

$-NR_4^+Cl^- + H_2PO_4^- \leftrightarrow -NR_4.H_2PO_4 + Cl^-$	(5.19)
$2(-NR_4^+Cl^-) + HPO_4^{2-} \leftrightarrow (-NR_4)_2.HPO_4 + 2Cl^-$	(5.20)
$(\equiv FeOH_2^+) + H_2PO_4^- \leftrightarrow (\equiv FeOH_2^+).H_2PO_4$	(5.21)
$2(\equiv FeOH_2^+) + HPO_4^{2-} \leftrightarrow (2(\equiv FeOH_2^+)).HPO_4$	(5.22)

Kinetic studies help determine contact time required for the ion exchange resin to reach equilibrium in solution. Batch studies implementing variable mixing speeds, produces high and low turbulence surrounding the resin particle. High mixing speeds produce high turbulence, which reduces the mass transfer resistance of the liquid film, external to the resin, making the rate limiting step to become intraparticle diffusion. The experimental data was modelled using various kinetic models including First-order reversible, Elovich, and particle diffusion models.
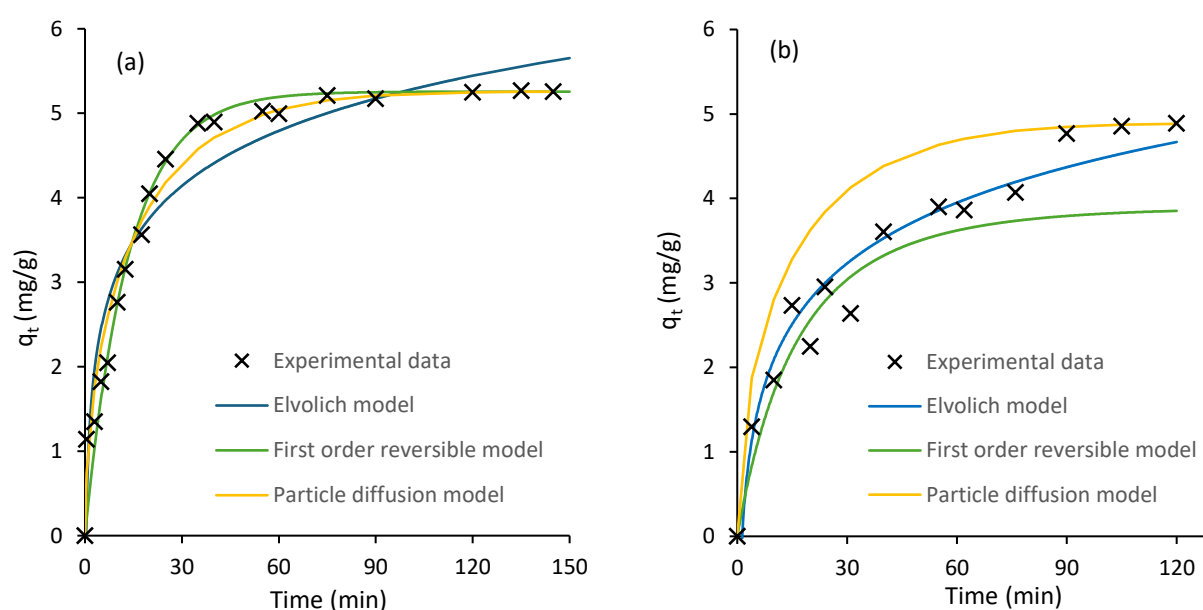

Figure 5.13. Kinetic models for the adsorption of phosphate onto FerrIX A33E resin at different mixing speeds (a) 150 rpm, (b) 30 rpm

Results from the kinetics experiments are displayed in Figures 5.13 (a) and (b). Results showed that after 50 minutes of high-speed mixing (150 rpm) equilibrium had been reached, whereas 90 minutes was required for low-speed mixing (30 rpm). The data fitting with the kinetic models showed that at high speeds, the first-order reversible and particle diffusion models had the best fit, while the Elovlich model was sufficient for both high and low mixing speeds.

These results show that mixing speeds has an affect on the kinetics mechanisms by which mass transfer takes place. Typically, in ion exchange resin, the rate controlling step is either controlled by film or intraparticle diffusion. In this

instance, it means that particle diffusion becomes the rate limiting step, which is reflected in the particle diffusion model having a better fit at high mixing speed. At low mixing speed, the first order model described the initial data (t<30 mins), which is in line with the linear rate model describing external film resistance. Besides mixing speed effects, film diffusion typically controls the rate determining step when the liquid phase concentration is low, or resin exchange capacity is high. Overall, the Elovich model fits best at low speeds, which is one of the most useful models for describing activated chemical adsorption. The Elovich model involves chemical adsorption and assumes that the rate of adsorption decreases exponentially with time due to an increase in surface coverage. The applicability of the Elovich model to the kinetics further supports that chemical reactions are involved in the uptake of phosphate with FerrIX A33E resin on a heterogenous surface as demonstrated by the isotherm studies and the suggested mechanisms.
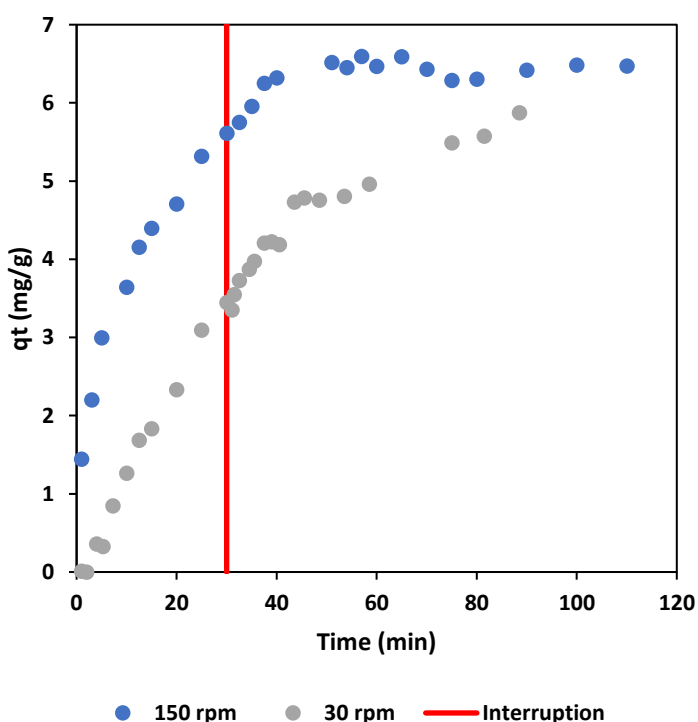
5.3.6.3. Interruption test

Figure 5.14. Interruption test at mixing speeds 30 and 150 rpm

One of the simplest techniques to determine the rate limiting step (i.e. particle or film diffusion) is the interruption test. During the sorption kinetics experiments, the resin was removed from the solution for 120 minutes, before being placed back. When the ion exchange process is controlled by particle diffusion, the concentration gradient is created inside the resin, which then level out when supply of fresh ions from the solution is interrupted. Once placed back into the solution the rate immediately is greater prior to the interruption. In the case of film diffusion, the amount of ion distributed in the film at the moment of interruption is almost undetectable, meaning that no concentration gradient in the resin exist. Thus, the interruption does not affect the process and the rate before and after the interruption is practically the same. Figure 5.14 shows that after the interruption, there was no major change in uptake of ions within the resin, indicating that film diffusion is the rate limiting step for both low and high mixing speeds. This result is also supported by the fact that the uptake rate was higher at higher mixing speed.

5.3.6.4.   Regeneration

To avoid the use of acids, typically used for regenerating similar ion exchange to FerrIX A33E, 5% sodium chloride at 30 mL min^{-1} flow rate was used as a regenerant in this study. The resin bed length was 10 cm. Ion exchange/regeneration cycles were repeated three times after the first ion exchange step in virgin resin. The ion exchange cycle conditions were 100 mg L^{-1}
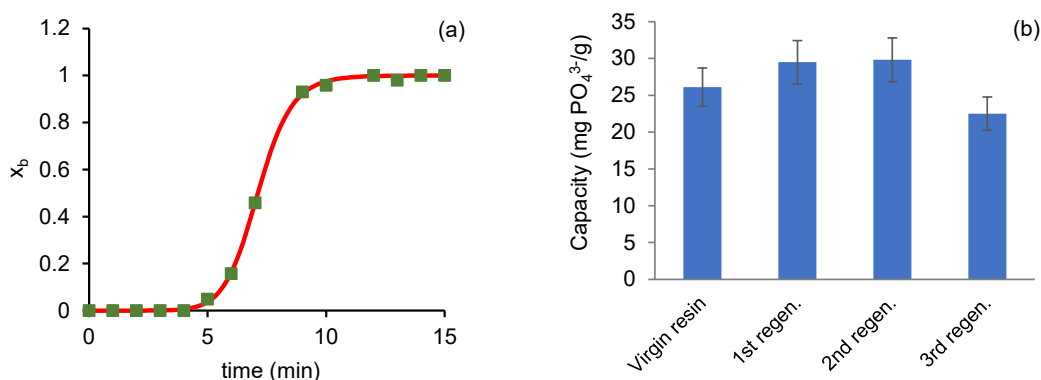

Figure 5.15. . (a) Breakthrough curve for the regeneration of the resin with 5% sodium chloride solution (symbols experimental data, continuous red curve is model fitting with f-BAM with parameters: h=0.271; k$_{BA,0}$=0.035 L.mg.minh-1; a$_0$= 965.4 mg/L), (b) effect of regeneration cycles

of phosphate at a flowrate of 60 mL min^{-1}. Figure 5.15 (a) shows that the breakthrough of the chloride ions occurred at around 5 minutes, while the resin was fully regenerated at around 10 minutes. Figure 11(a) also displays excellent fitting of the experimental data with Bohart-Adams Fractal model. For any loading breakthrough curve, it is possible to calculate the average composition of the resin in the bed and to estimate the total capacity of the resin by integrating the area above the breakthrough curve (Slater, 1991) . The change of resin capacity, calculated by integration of breakthrough curves, after successive regeneration steps is shown in Figure 5.15 (b). The average capacity of the resin after the first regeneration has slightly increased from the virgin resin, indicating that more exchange sites could possibly be made available for exchange following the first use of the virgin resin. The first and the second regeneration runs show very similar capacities, but after the third regeneration cycle, the average resin capacity has slightly decreased by ~14%, though it remained within the experimental error of the resin capacity. This indicates that FerrIX A33E could successfully be used as an ion exchange for the removal of phosphates from water to sustainably protect the aquatic environment from the harmful effects of phosphates.

5.4. Conclusions

This chapter provided an in depth exploration of ion exchange processes, in particular the challenges and mechanisms involved in silica removal. The study emphasized the significance of competing ions such as phosphate, nitrate, and chloride in influencing the effectiveness of silica removal, especially in multicomponent systems. It was observed that the presence of these competing ions reduces the efficiency of conventional ion exchange resins for silica, highlighting the need for more selective materials. The main findings of this chapter are:

- The comparison of FerrIX A33E resin in its chloride (Cl^-) and hydroxide (OH^-) forms demonstrated the different behaviours of these forms in silica removal. The hydroxide form exhibited faster kinetics and higher efficiency in silica adsorption. This was largely due to its improved diffusion properties.

- Isotherm and kinetic models applied throughout the chapter highlighted the complex adsorption mechanisms at play. The Redlich-Peterson and Freundlich models provided the best fit for understanding the heterogeneous nature of the resin.

- Models such as Bohart-Adams, Thomas, and Clark were useful in predicting breakthrough curves in column studies. However, modified models such as the Bohart-Adams n-order and fractal models proved superior in capturing the asymmetric behaviour of adsorption, particularly for the hydroxide form of FerrIX resin.

- The First-order reversible model and the Elovich model described the adsorption kinetics well under varying conditions, especially at high and low mixing speeds. These models were instrumental in revealing the rate-limiting steps of the process.

- Competitive isotherms revealed that phosphate consistently exhibited the highest adsorption capacity compared to nitrate and silica. In a multicomponent system, the adsorption of phosphate decreased significantly due to competition with other ions.

- FerrIX A33E resin exhibits superior phosphate removal, which suggests that selectively removing phosphate can improve the uptake of silica in a multicomponent system.

5.5. References

A.O, D., Olalekan, A., Olatunya, A., & Dada, A. O. (2012). Langmuir, Freundlich, Temkin and Dubinin–Radushkevich Isotherms Studies of Equilibrium Sorption of Zn 2+ Unto Phosphoric Acid Modified Rice Husk. *J. Appl. Chem., 3,* 38-45. https://doi.org/10.9790/5736-0313845

Acelas, N. Y., Martin, B. D., López, D., & Jefferson, B. (2015). Selective removal of phosphate from wastewater using hydrated metal oxides dispersed within anionic exchange media. *Chemosphere, 119,* 1353-1360. https://doi.org/https://doi.org/10.1016/j.chemosphere.2014.02.024

Alyüz, B., & Veli, S. (2009). Kinetics and equilibrium studies for the removal of nickel and zinc from aqueous solutions by ion exchange resins. *Journal of Hazardous Materials, 167*(1), 482-488. https://doi.org/https://doi.org/10.1016/j.jhazmat.2009.01.006

An, B., Jung, K.-Y., Zhao, D., Lee, S.-H., & Choi, J.-W. (2014). Preparation and characterization of polymeric ligand exchanger based on chitosan hydrogel for selective removal of phosphate. *Reactive and Functional Polymers, 85,* 45-53. https://doi.org/https://doi.org/10.1016/j.reactfunctpolym.2014.10.003

Anbazhagan, S., Thiruvengadam, V., & Sukeri, A. (2021). An Amberlite IRA-400 Cl– ion-exchange resin modified with Prosopis juliflora seeds as an efficient Pb2+ adsorbent: adsorption, kinetics, thermodynamics, and computational modeling studies by density functional theory [10.1039/D0RA10128A]. *RSC advances, 11*(8), 4478-4488. https://doi.org/10.1039/D0RA10128A

Appel, J. (1973). Freundlich's adsorption isotherm. *Surface Science, 39*(1), 237-244. https://doi.org/https://doi.org/10.1016/0039-6028(73)90105-2

Ayawei, N., Ebelegi, A. N., & Wankasi, D. (2017). Modelling and interpretation of adsorption isotherms. *Journal of Chemistry, 2017.*

Barrer, R. M., & Klinowski, J. (1974). Ion-exchange selectivity and electrolyte concentration [10.1039/F19747002080]. *Journal of the Chemical Society,*

Faraday Transactions 1: Physical Chemistry in Condensed Phases, 70(0), 2080-2091. https://doi.org/10.1039/F19747002080

Belhachemi, M., & Addoun, F. (2011). Comparative adsorption isotherms and modeling of methylene blue onto activated carbons. *Applied Water Science, 1*(3), 111-117. https://doi.org/10.1007/s13201-011-0014-1

Bhattacharya, A. K., & Venkobachar, C. (1984). Removal of Cadmium (II) by Low Cost Adsorbents. *Journal of Environmental Engineering, 110*(1), 110-122. https://doi.org/doi:10.1061/(ASCE)0733-9372(1984)110:1(110)

Bohart, G. S., & Adams, E. Q. (1920). SOME ASPECTS OF THE BEHAVIOR OF CHARCOAL WITH RESPECT TO CHLORINE.1. *Journal of the American Chemical Society, 42*(3), 523-544. https://doi.org/10.1021/ja01448a018

Chabani, M., Amrane, A., & Bensmaili, A. (2006). Kinetic modelling of the adsorption of nitrates by ion exchange resin. *Chemical engineering journal, 125*(2), 111-117.

Cheung, C. W., Porter, J. F., & McKay, G. (2000). Elovich equation and modified second-order equation for sorption of cadmium ions onto bone char. *Journal of Chemical Technology & Biotechnology, 75*(11), 963-970. https://doi.org/10.1002/1097-4660(200011)75:11<963::aid-jctb302>3.0.co;2-z

Clark, R. M. (1987). Evaluating the cost and performance of field-scale granular activated carbon systems. *Environmental Science & Technology, 21*(6), 573-580. https://doi.org/10.1021/es00160a008

Cross, K. M., Lu, Y., Zheng, T., Zhan, J., McPherson, G., & John, V. (2009). Water decontamination using iron and iron oxide nanoparticles. In *Nanotechnology Applications for Clean Water* (pp. 347-364). Elsevier.

Cumbal, L., & Sengupta, A. K. Arsenic removal using polymer-supported hydrated iron(III) oxide nanoparticles: role of donnan membrane effect. (0013-936X (Print)).

Dawodu, F., Akpomie, G., & Abuh, M. (2012). Equilibrium isotherm studies on the batch sorption of Copper (II) ions from aqueous solution onto Nsu clay. *International Journal of Scientific & Engineering Research, 3*(12), 1-7.

Ghosh, P. (1988). Silica in boiler water. *Anti-Corrosion Methods and Materials, 35*(10), 8-14. https://doi.org/10.1108/eb020697

Goldberg, S., & Sposito, G. (1985). On the mechanism of specific phosphate adsorption by hydroxylated mineral surfaces: A review. *Communications in Soil Science and Plant Analysis, 16*(8), 801-821. https://doi.org/10.1080/00103628509367646

Hu, Q., Liu, H., Zhang, Z., & Pei, X. (2020). Development of fractal-like Clark model in a fixed-bed column. *Separation and purification technology, 251*, 117396. https://doi.org/https://doi.org/10.1016/j.seppur.2020.117396

Hu, Q., Pang, S., Wang, D., Yang, Y., & Liu, H. (2021). Deeper Insights into the Bohart–Adams Model in a Fixed-Bed Column. *The Journal of Physical Chemistry B, 125*(30), 8494-8501. https://doi.org/10.1021/acs.jpcb.1c03378

Inc., P. M. R. (2014). BEHAVIOR OF SILICA IN ION EXCHANGE AND OTHER SYSTEMS.

Juang, R.-S., & Chen, M.-L. (1997). Application of the Elovich Equation to the Kinetics of Metal Sorption with Solvent-Impregnated Resins. *Industrial & Engineering Chemistry Research, 36*(3), 813-820. https://doi.org/10.1021/ie960351f

Karpowicz, F., Hearn, J., & Wilkinson, M. C. (1995). The quantitative use of the Bohart-Adams equation to describe effluent vapour profiles from filter beds. *Carbon, 33*(11), 1573-1583. https://doi.org/https://doi.org/10.1016/0008-6223(95)00119-X

Khan, A., & Khan, A. (2010). Ion-exchange studies on poly-o-anisidine Sn(IV) phosphate nano composite and its application as Cd(II) ion-selective membrane electrode. *Central European Journal of Chemistry, 8*, 396-408. https://doi.org/10.2478/s11532-010-0002-6

Kociołek-Balawejder, E., Stanisławska, E., & Ciechanowska, A. (2017). Iron(III) (hydr)oxide loaded anion exchange hybrid polymers obtained via tetrachloroferrate ionic form—Synthesis optimization and characterization. *Journal of Environmental Chemical Engineering, 5*(4), 3354-3361. https://doi.org/https://doi.org/10.1016/j.jece.2017.06.043

Misak, N. Z. (1993). Langmuir isotherm and its application in ion-exchange reactions. *Reactive Polymers, 21*(1), 53-64. https://doi.org/https://doi.org/10.1016/0923-1137(93)90054-J

Muhammad, A., Soares, A., & Jefferson, B. (2019). The impact of background wastewater constituents on the selectivity and capacity of a hybrid ion exchange resin for phosphorus removal from wastewater. *Chemosphere, 224*, 494-501. https://doi.org/https://doi.org/10.1016/j.chemosphere.2019.01.085

Nur, T., Johir, M., Loganathan, P., Nguyen, T., Vigneswaran, S., & Kandasamy, J. (2014). Phosphate removal from water using an iron oxide impregnated strong base anion exchange resin. *Journal of Industrial and Engineering Chemistry, 20*(4), 1301-1307.

Nur, T., Shim, W. G., Johir, M. A. H., Vigneswaran, S., & Kandasamy, J. (2014). Modelling of phosphorus removal by ion-exchange resin (Purolite FerrIX A33E) in fixed-bed column experiments. *Desalination and Water Treatment, 52*(4-6), 784-790. https://doi.org/10.1080/19443994.2013.827298

Padungthon, S., Li, J., German, M., & SenGupta, A. (2014). Hybrid Anion Exchanger with Dispersed Zirconium Oxide Nanoparticles: A Durable and Reusable Fluoride-Selective Sorbent. *Environmental Engineering Science, 31*, 360-372. https://doi.org/10.1089/ees.2013.0412

Pan, B., Wu, J., Pan, B., Lv, L., Zhang, W., Xiao, L., Wang, X., Tao, X., & Zheng, S. (2009). Development of polymer-based nanosized hydrated ferric oxides (HFOs) for enhanced phosphate removal from waste effluents. *Water Research, 43*(17), 4421-4429. https://doi.org/https://doi.org/10.1016/j.watres.2009.06.055

Pan, M., Lin, X., Xie, J., & Huang, X. (2017). Kinetic, equilibrium and thermodynamic studies for phosphate adsorption on aluminum hydroxide modified palygorskite nano-composites. *RSC advances, 7*(8), 4492-4500.

Plesset, M., Helfferich, F., & Franklin, J. (1958). Ion exchange kinetics. A nonlinear diffusion problem. II. Particle diffusion controlled exchange of univalent and bivalent ions. *The journal of chemical physics, 29*(5), 1064-1069.

Purolite. (2024). *A400 Product Data Sheet*

Sik Ali, M. B., Hamrouni, B., Bouguecha, S., & Dhahbi, M. (2004). Silica removal using ion-exchange resins. *Desalination, 167*, 273-279. https://doi.org/https://doi.org/10.1016/j.desal.2004.06.136

Slater, M. J. (1991). Chapter 3 - Kinetics of ion exchange in solution. In M. J. Slater (Ed.), *Principles of Ion Exchange Technology* (pp. 18-28). Butterworth-Heinemann. https://doi.org/https://doi.org/10.1016/B978-0-7506-1115-2.50010-7

Sowmya, A., & Meenakshi, S. (2013). Removal of nitrate and phosphate anions from aqueous solutions using strong base anion exchange resin. *Desalination and Water Treatment, 51*(37-39), 7145-7156. https://doi.org/10.1080/19443994.2013.771286

Thomas, H. C. (1944). Heterogeneous Ion Exchange in a Flowing System. *Journal of the American Chemical Society, 66*(10), 1664-1666. https://doi.org/10.1021/ja01238a017

Wu, F.-C., Liu, B.-L., Wu, K.-T., & Tseng, R.-L. (2010). A new linear form analysis of Redlich–Peterson isotherm equation for the adsorptions of dyes. *Chemical engineering journal, 162*(1), 21-27. https://doi.org/https://doi.org/10.1016/j.cej.2010.03.006

Yoon, S.-Y., Lee, C.-G., Park, J.-A., Kim, J.-H., Kim, S.-B., Lee, S.-H., & Choi, J.-W. (2014). Kinetic, equilibrium and thermodynamic studies for phosphate adsorption to magnetic iron oxide nanoparticles. *Chemical engineering journal, 236*, 341-347.

Yu, J., Li, M., & Jin, Z. (2023). Exploration of saturated transport of ion concentration differences in C–S–H channels. *Materials and Structures, 57*(1), 8. https://doi.org/10.1617/s11527-023-02272-z

Zarrabi, M., Soori, M. M., Noori Sepehr, M., Amrane, A., Borji, S., & Ghaffari, H. R. (2014). Removal of phosphorus by ion-exchange resins: Equilibrium,

kinetic and thermodynamic studies. *Environmental Engineering and Management Journal*.

Zhang, Q., Pan, B., Chen, X., Zhang, W., Pan, B., Zhang, Q., Lv, L., & Zhao, X. S. (2008). Preparation of polymer-supported hydrated ferric oxide based on Donnan membrane effect and its application for arsenic removal. *Science in China Series B: Chemistry*, *51*(4), 379-385. https://doi.org/10.1007/s11426-007-0117-6

6. Evaluation of Hybrid Technologies in removing colloidal silica

6.1. Introduction

Traditional water treatment methods, such as coagulation, sedimentation and filtration have been the cornerstone of water treatment for decades. However, the complexities of modern contaminants and a resource-constrained world have necessitated for more sophisticated solutions. In this context, hybrid technologies provide a significant innovation. Combining various physical, chemical and biological processes allows these integrated methods to leverage the strength of individual systems while compensating for their weaknesses. This synergy enhances the efficiency and cost-effectiveness of water treatment processes.

The removal of colloidal silica is a prevalent and challenging task in boiler feed water treatment. Due to its small size and stability, colloidal silica poses significant challenges for conventional water treatment methods. This chapter explores the effectiveness of various hybrid technologies in the removal of colloidal silica, focusing on the integration of an oxidation treatment (ozone) with ion exchange, membrane filtration, and coagulation processes.

The structure of and chemistry at liquid-solid interfaces is a prominent mechanism in the removal of contaminants from water by a number of technologies such as membrane and ion exchange (Zaera, 2012). In water, the silica-water interface is charged due to protonation/deprotonation reactions of surface bound hydroxyl groups (Duval et al., 2002; Iler). As the isoelectric point of silica is pH 2-3, the surface is typically negatively charged (Parks, 1965). Ozone is a powerful oxidant which is known to effect functional groups on many material surfaces (Dabasinskaite et al., 2021; Lai et al., 2024; Osbeck et al., 2011). By studying the effects ozone has on colloidal silica surface chemistry, combination with other technologies could lead to increased silica removal efficiency.

Recent developments on hybrid technologies have shown promising opportunities at removing colloidal silica. One such technology is the use of advanced oxidation processes (AOPs) based on ozone combined with UV. The combined use of ozone and UV radiation at 185 nm wavelength was found to invert colloidal silica into dissolved silica (Johanes Wibowo, 1997). Thus, by taking advantage of converting colloidal silica to dissolved silica, an ion exchange step could be used to completely remove silica. Use of ozone has also shown to contribute to colloidal particle destabilization, especially for particles coated with natural organic matter, through various mechanisms including oxidation of organic coatings, disruption of electrostatic repulsion and breakdown of organic matter into smaller fragments (Chandrakanth & Amy, 1996; Chheda & Grasso, 1994). Studies have shown the improvement of combined UV/ozone with ion exchange to improve decomposition of iron products that were adsorbed using ion exchange (Wada et al., 2005). The use of ozone on silica has shown to increase the oxygen containing functional groups on the surface of the structure, which was proved with FTIR and XPS, improving the interfacial interactions between the silicone substrate and a membrane (Kang et al., 2018). Other studies have demonstrated how ozone can be used to regenerate silica-based zeolites by influencing surface phenomena on the silica. Specifically, ozone aids in the removal of adsorbed organic pollutants from the surface, effectively restoring the adsorption capacity of the zeolites. (Reungoat et al., 2007).

Further research, which investigated a hybrid process consisting of ozone and membrane filtration, was able to show that an ozonated solution of humic acid was able to reduce membrane fouling, avoiding the need for cleaning the membrane (Schlichter et al., 2003). Combination of PACl coagulant with UF membranes, was shown to form stable cake layer on the membrane, negating the fouling impact it had on the membrane (Yu et al., 2021) .

Despite the potential benefits that AOPs could bring to the removal of silica in water, research studies in this area are scarce. Thus, this chapter aimed at delving into studying hybrid technologies based on advanced oxidation and separations to address this gap of knowledge. The effects of ozone on colloidal silica zeta

potential and particle size was first studied via a bench scale reactor. The ozonated colloidal silica solutions was then treated using ion exchange and membrane technologies. Additionally, the coagulation of colloidal silica with aluminium and titanium in Chapter 3, was then combined with membrane technology to evaluate membrane fouling and silica rejection.

6.2. Materials and Methods

6.2.1. Chemicals and reagents

For colloidal silica solution preparation refer to Chapter 3.

6.2.2. Analysis

The analysis of total silica (SiO_2) was performed by microwave plasma atomic emission spectrometer (4200 MP-AES) (Agilent technologies, UK) equipped with a standard torch. Prior to measurement, the instrument was calibrated using a silica standard solution, 50 mg/L as SiO_2 (HACH, UK).

Particle size and zeta potential of the colloidal silica was measured using a ZetaSizer Nano equipped with universal 'dip' cell (Malvern instruments, UK).

6.2.3. Experimental set up

6.2.3.1. Ozone experiments

Ozone was generated by a BMT Messtechnik 803 Ozone Generator (BMT-Messtechnik, Germany) from compressed oxygen cylinder (BOC, UK). The ozone gas concentration was set using a power dial on the ozone generator and its value was measured using a BMT Messtechnik 963 Ozone Analyser (BMT-Messtechnik, Germany). The ozone was directed through a glass sinter gas diffuser into a reactor containing approximately 400 mL of solution at 35 mg SiO_2/L colloidal silica, which was stirred using a magnetic stirrer (40 rpm). From the reactor, the ozone was redirected towards the ozone destructor (sodium aluminosilicate) before being exhausted in a fume hood. Gas flow was controlled using a variable-area-gas flow meter fitted with a needle throttle valve. Gas flowrate was around 480 mL/min, with the ozone gas concentration at approximately 70 g/m^3 at normal temperature and pressure (NTP: 20°C and 1

atm). All experiments were conducted at room temperature of 20 ±1°C for 10, 30 and 60 minutes. To remove any residual ozone, samples were exposed to a gentle stream of air for about 5 minutes before analysis.

6.2.3.2.Ozone/ ion exchange

A 40 mL of the ozonated solution was placed in 50 mL- plastic sample tube containing varying masses of ion exchange resin after being exposed to a gentle air stream to remove any residual ozone. The solutions with ion exchange resin were then agitated using a 12-position rotating mixer (Stuart SB3 rotator) set at 40 rpm. Silica uptake of the resin was then calculated with the equation below:

$$q_e = V \times \frac{(C_o - C_e)}{m_{IX}} \tag{6.1}$$

Where q_e is the phosphate uptake onto the resin at equilibrium (mg/g), V is the volume of solution (L), C_o and C_e are the initial and equilibrium concentrations (mg/L), and m_{IX} is the mass of the ion exchange resin (g).

6.2.3.3.Ozone/membrane

The ozonated solution was passed through PVDF, PVDF/GO and PVDF/CNT membranes in a recirculating cross flow filtration unit (CFU). A GA series pump, powered by DP-415.A AC driver with a min speed of 500 RPM and max of 9000 RPM (Micropump, USA) was used to pump the solution. The unit was equipped with a flowmeter and two digital WIKA DG-10-E pressure gauges, for transmembrane pressure (TMP) measurements. The following equation was used for TMP measurements:

$$TMP = \left(\frac{P_F + P_R}{2}\right) - P_p \tag{6.2}$$

Where, P_F is the pressure of the feed (bar), P_R is the pressure of the retentate, and P_p is the pressure of the permeate (bar). The permeate was collected in a plastic beaker and its mass was continuously measured using an analytical balance connected to a PC which recorded the data using a software (SmartLux Simple Data Logger). The flux was calculated with the following equation:

$$J = \frac{m}{\rho At} \qquad (6.3)$$

Where J is the membrane flux (L/m²h), m is the mass of permeate collected (kg), ρ is water density (kg/L), A is the effective area of the membrane (m²) and t is the time for permeate collection. The permeability of the membrane was calculated by dividing the flux by the TMP.

To evaluate the flux recovery of the membrane, the flux recovery ratio (FRR) is used as an indicator of the membrane's antifouling performance. It represents the ability of the membrane to restore its water permeability after being exposed to fouling conditions. The FRR is defined as follows:

$$FRR \ (\%) = \frac{J_{w2}}{J_{w1}} \times 100 \qquad (6.4)$$

FRR (%) is the Flux Recovery Ratio, expressed as a percentage. It quantifies how much of the membrane's original water flux is recovered after cleaning. J_{w1} is the initial pure water flux before the membrane is exposed to the fouling solution (L/m²·h), J_{w2} is the pure water flux measured after the cleaning procedure (L/m²·h) (e.g., after ozonated solution and flipping of the membrane). A higher FRR indicates better antifouling performance.

6.2.3.4. Coagulation/membrane

Coagulation experiments discussed in Chapter 3 were conducted using alum and titanium, at larger volumes of 1 L. Once the coagulated samples had settled, 500 mL of solution was decanted into the membrane cross flow unit tank. The experiment was then run as discussed above.

6.3. Results and discussion

6.3.1. Effect of ozone on colloidal silica

The effect of ozonation on colloidal silica zeta potential and particle size was studied. The colloidal silica was ozonated at durations of 10, 30 and 60 minutes. From Figure 6.1 which shows the results from the ozonation experiments, it can be seen that un-ozonated colloidal silica has a zeta potential of around -15 mV.

When ozonated, the zeta potential of the solution was seen to decrease, to -23 mV and -26 mV, after 10 and 30 minutes of ozonation, respectively. However, longer ozonation showed a slight increase to -21 mV. These reductions in zeta potential could be due to any impurities that were found on the surface of the silica being destroyed or perhaps due to the silane groups (Si-H) on the surface of silica being converted into silanol (Si-OH) bonds, that was reported by Spialter et al (Spialter et al., 1971). Initially the ozone treatment can generate silanol groups on the silica surface. These silanol groups can dissociate to from silicate ions (SiO-) contributing to the increased negative surface charge. Ozone can also cause siloxane bond cleavage (Si-O-Si) in the silica network, causing structural changes of the particle. In addition, it was demonstrated that ozonating colloidal silica increased oxygen containing functional groups on silica surfaces (Kang et al., 2018), which would also explain the decrease in zeta potential observed in our study. Once the ozone causes surface saturation of silanol groups, mechanisms such as oxidative coupling or dehydration reaction can facilitate the formation of siloxane groups thus increasing the surface charge (Egitto & Matienzo, 2006; Wang et al., 2017; Xu et al., 2018) as observed in our study when ozonation was applied for long time (60 minutes). The increase in zeta potential seen at 60 minutes could also be due to a drop in pH (Table 6.1). Table 1 shows that the pH of the silica solution decreased as the ozonation time increased to reach 5.93 from an initial value of 7.75, which could explain the increase in zeta potential observed since at lower pH the silanol groups are expected to be less ionized (Schwarz et al., 1984). The effect of ozonation on the size of the colloidal silica was insignificant (Table 1).
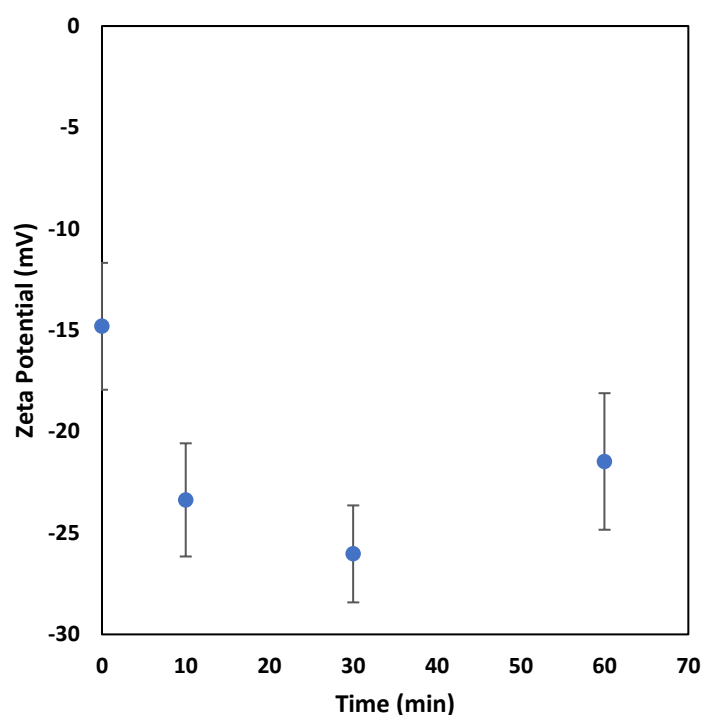
Figure 6.1. Effect of ozonation time on the zeta potential of colloidal silica (Ozone gas concentration =70 g/m3 NTP)

Table 6.1. effect of ozonation on colloidal silica size and pH of the solution

Sample	Size (nm)	pH
Colloidal silica	38.9	7.75
C.S ozonated 10 mins	39.6	6.82
C.S ozonated 30 mins	39.2	6.43
C.S ozonated 60 mins	39.0	5.93

6.3.2. Effect of peroxone on colloidal silica

The ozone experiments with colloidal silica were repeated in the presence of hydrogen peroxide (i.e. peroxone process) (Merényi et al., 2010; Xu & Goddard). The peroxone process is a commonly used advanced oxidation process for water treatment since it produces strong oxidants (hydroxyl radicals) (Tizaoui et al., 2007; Wang et al., 2018; Wu & Englehardt, 2015). The results shown in Table 2

indicate that the introduction of hydrogen peroxide had minimal effect on colloidal silica size as was observed when only ozone was used. However, hydrogen peroxide showed a significant effect on zeta potential which increased from -17.90mV to -14.30 and -2.64 mV at ozone to hydrogen peroxide ratios of 1:1 and 1:2, respectively. The peroxone is known to be more efficient than ozone in generating hydroxyl radicals which can lead to faster degradation rates (Cruz-Alcalde et al., 2020; Freese et al., 1999; Meshref et al., 2017). Thus, the highly reactive hydroxyl radicals generated by the peroxone process oxidize the surface of the colloidal silica particles, converting the silanol groups into siloxane groups as discussed for the case of ozone but at much faster rates. Due to this, the surface saturation of silanol groups occurs much faster, reducing the surface charge. These findings demonstrate that oxidation of colloidal silica has potential to be exploited for enhancing the efficiency of other silica removal technologies.

Table 6.2. Effect of peroxone on colloidal silica size and zeta potential (ozonation time=30 min)

Sample	Size (nm)	Zeta potential (mV)
Colloidal Silica	40.9	-17.90
Ozone:H_2O_2 (1:1)	39.4	-14.30
Ozone:H_2O_2 (1:2)	39.4	-2.64
Ozone only	40.1	-25.67

6.3.3. Ozone and ion exchange

Figure 6.2 presents adsorption isotherms comparing un-ozonated and ozonated colloidal silica at initial SiO_2 concentrations of (a) 38 mg/L and (b) 150 mg/L. The application of ozone clearly enhanced the adsorption capacity of the ion exchange resin, as reflected by the increased values of qe in both cases— particularly at higher concentrations.

This improvement is attributed to the ozone-induced reduction in the surface charge of colloidal silica (as shown previously in Figure 6.1, with 30 minutes of ozonation). The decrease in negative surface charge enhances electrostatic interactions between the silica particles and the positively charged functional groups on the ion exchange resin, facilitating greater adsorption.

The effect was especially pronounced at higher silica concentrations (Figure 6.2b), suggesting that ozone treatment becomes increasingly beneficial as the colloidal load increases. This supports the hypothesis that ozonation can serve as a pre-treatment step to improve ion exchange performance in high-silica waters, such as those encountered in power plant or industrial boiler systems.
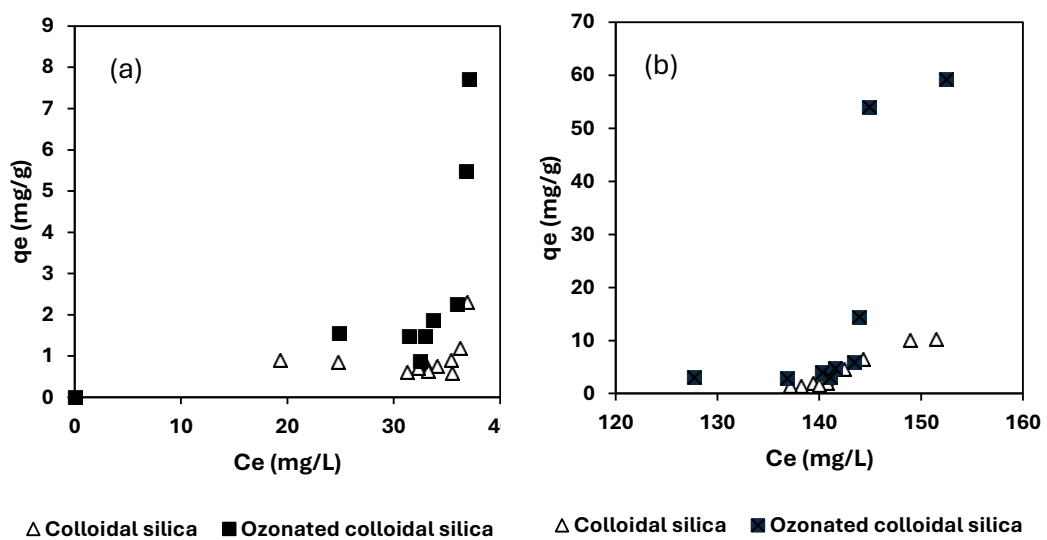

△ Colloidal silica ■ Ozonated colloidal silica   △ Colloidal silica ■ Ozonated colloidal silica

Figure 6.2. Adsorption isotherm of ozonated and un-ozonated colloidal silica at initial SiO_2 concentrations of (a) 38 mg/L and (b) 150 mg /L (Gas flowrate was around 480 mL/min, with the ozone gas concentration at approximately 70 g/m³ at normal temperature and pressure (NTP: 20ºC and 1atm), duration 30 minutes)

6.3.4. Ozone and membrane

Figure 6.3 shows the permeance permeability of the pure water flux before and after cleaning and ozonated colloidal silica (30 minute ozonation), Figure 6.4 shows the flux recovery ratio. Overall, the permeability followed the order of PVDF<GO<CNT, as seen in Chapter 3. However, the pure water permeability flux after cleaning was greater than the initial cleaning, this was consistent with all membranes. This could be due to the cleaning of the membrane removed any
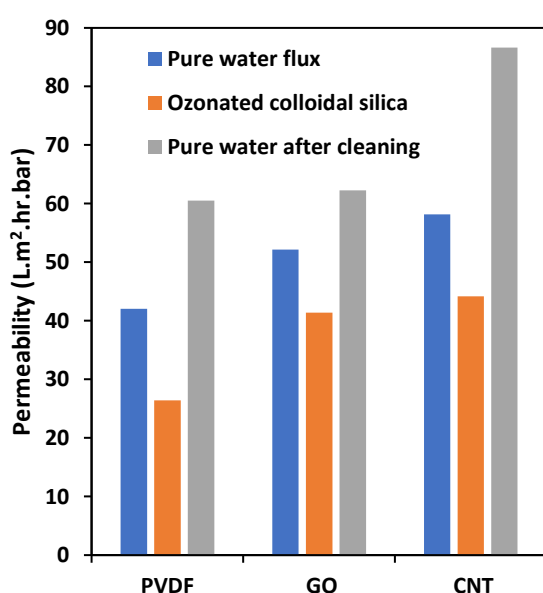

Figure 6.5. Permeability of PVDF, GO and CNT of ozonated colloidal silica
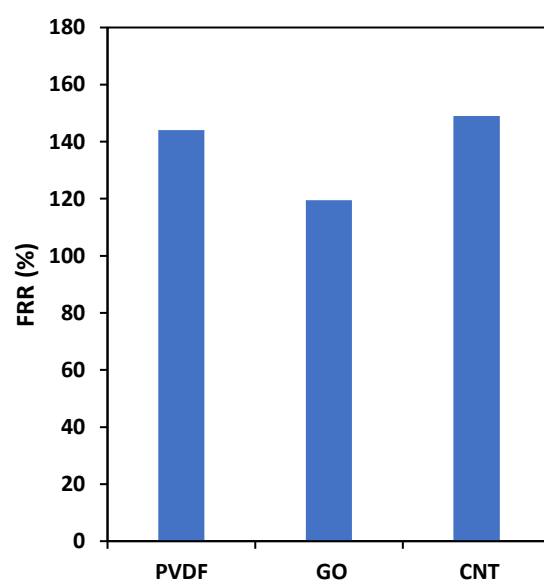
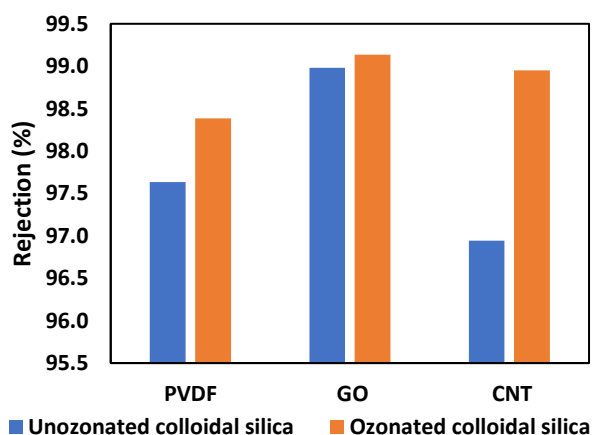Figure 6.5. Flux recovery ratio of PVDF, GO, and CNT ozonated colloidal silica after cleaning

Figure 6.5. Rejection of ozonated and un-ozonated colloidal silica

residual fouling from the virgin membrane. Other unlikely reasons could be the oxidative cleaning of the membrane, as residual ozone was removed prior to membrane use. Surface conditioning of the membrane by passing the ozonated colloidal silica may have occurred, modifying the surface properties of the membrane, subsequently enhancing its performance.

The rejection of ozonated and un-ozonated colloidal silica for all 3 membranes is presented in Figure 6.5. Results indicate that rejection of colloidal silica is improved by the ozonation process. This is predominantly seen in the CNT membrane, where rejection improved from 97.2 to 99%. The enhanced surface zeta potential of the ozonated colloidal silica has boosted the electrostatic repulsion between the silica particles and the membrane surface. The increased repulsion prevents the silica particles approaching and passing through the membrane pores effectively, thereby improving their rejection. This is further supported by Table 6.3, which presents the concentration of silica that was present in the cleaned solution. When the membranes were washed after having ozonated colloidal silica pass through, the observed concentration of residual particles was greater due to the weaker attachment of these particles to the membrane surface. The increased negative surface charge seems to have resulted in weaker van der Waals forces, consequently silica particles adhere less strongly to the membrane surface. Subsequently during the cleaning step, these particles are more easily dissolved and removed, leading to higher concentration of silica in the wash water. This improved detachment shows the effectiveness of ozonation in reducing fouling and maintaining membrane performance.

Table 6.3. Permeate of un-ozonated and ozonated solutions when cleaning with pure water

Membrane type	Permeate un-ozonated silica after cleaning (mg SiO_2/L)	Permeate ozonated silica after cleaning (mg SiO_2/L)
PVDF	0.26	0.41
GO (2 wt%)	0.52	0.82
CNT (1 wt%)	0.71	1.01

6.3.5. Coagulation and membrane

Following the results of Chapter 3, the two most effective coagulants found were alum and titanium in the removal of colloidal silica. These coagulants were tested with membranes (PVDF, GO, and CNT) as hybrid technologies. Table 6.4 shows the parameters of the jar test for titanium, while Table 6.5 shows the results of the coagulation/membrane hybrid experiments. The permeability of the membranes is presented in Figure 6.6, where PWF is the pure water flux.

Table 6.4. Parameters for titanium coagulation before membranes

Parameter	Value
Coagulant type	Titanium
Dosage (mg/L)	15
Volume reactor (L)	1
pH	6
Initial silica concentration (mg/L)	31.46

Table 6.5. Results of titanium coagulated membrane solution

Sample	Silica (after coagulation and settlement)	Permeate silica (after membrane)	Permeate silica (from backwash cleaning)	Residual Ti (after coagulation)	Residual Ti (after membrane)	FRR (%)
PVDF	10.09	1.42	0.9	0.67	0.06	87.0
GO	9.79	0.01	1.72	0.65	0.00	94.3
CNT	9.83	0.13	1.54	0.54	0.01	95.3
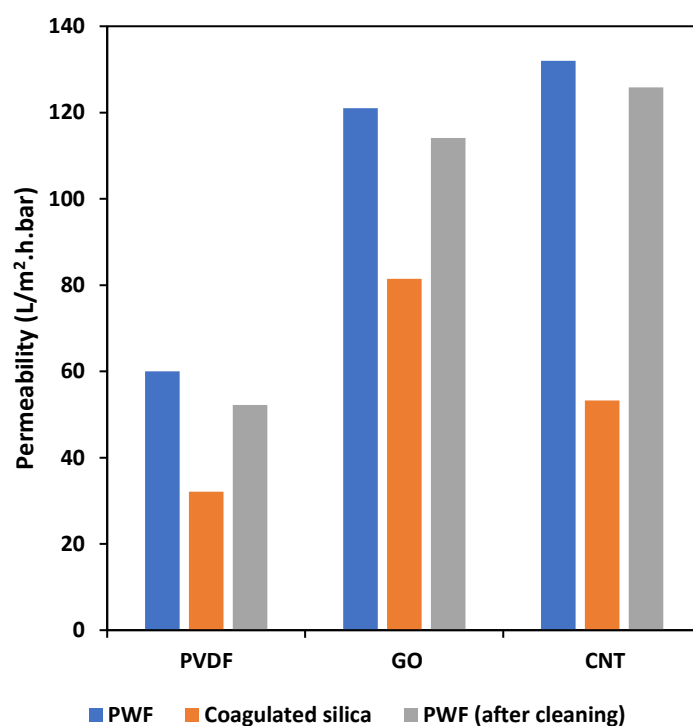
Figure 6.6. Permeability of titanium coagulated solution.

Table 6.5 reveals that following coagulation and settlement process, GO membrane had the greatest rejection of silica, followed by CNT and PVDF. After cleaning of the membrane, the silica that was removed in the cleaning, was much greater in all membranes compared to the ozonated silica. This is likely due to the larger flocs that are formed in the coagulation process, meaning fewer smaller particles can penetrate and block the membrane within its pore structure. These larger flocs that are deposited on the membrane surface form a thicker but more porous cake layer. This porous structure allows for more water to pass through easier compared to the compact dense layer formed with smaller particles. Additionally, the coagulation and settlement process removed a large portion of the fouling load meaning that the membrane is less likely to experience severe fouling. This is reflected in the flux recovery seen in the membranes. Membranes which had not been pretreated with coagulant seen in Chapter 4, had a significantly lower FRR compared to Table 6.5. Additionally, the membranes were able to remove most of the residual titanium that was found in the coagulated solution.

Table 6.6. Parameters for alum coagulation before membranes

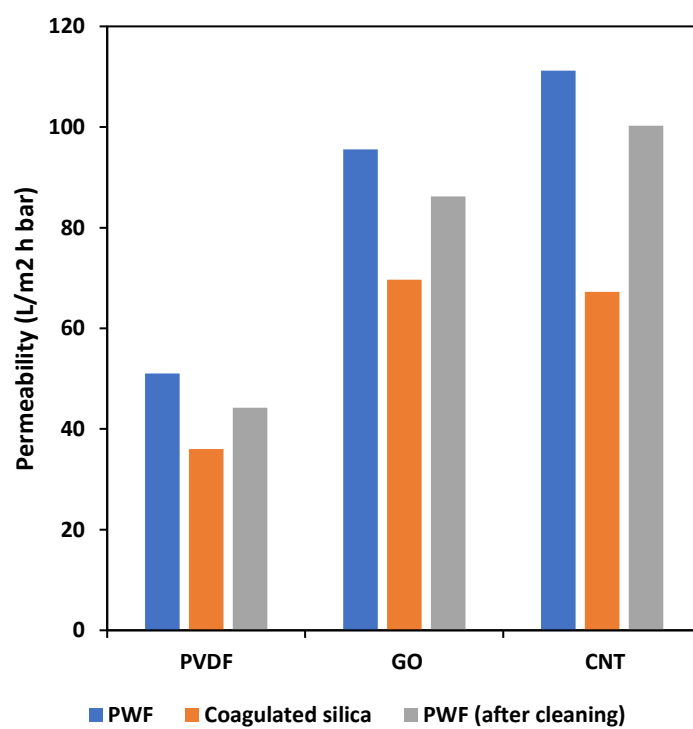| Parameter	Value
Coagulant type	Alum
Dosage (mg/L)	15
Volume reactor (L)	1
pH	6
Initial silica concentration (mg/L)	30.65

Figure 6.7. Permeability of alum coagulated solution

Table 6.7. Results of alum coagulated silica solution

Sample	Silica (after coagulation and settlement)	Permeate silica (after membrane)	Permeate silica (from cleaning)	Residual Al (after coagulation)	Residual Al (after membrane)	FRR (%)
PVDF	6.55	0.81	0.17	0.49	0.09	86.8
GO	5.24	0.05	0.18	0.56	0.02	90.3
CNT	7.17	0.23	0.23	0.44	0.06	90.1

Table 6.6 shows the parameters of the jar test for Alum. Table 6.7 shows the results of the experiments of the alum coagulation/membrane hybrid and the permeability of the membrane results are presented in Figure 6.7. The results follow a similar trend that was seen with titanium coagulant. The major differences seen with the alum coagulant was that the permeate during cleaning contained significantly less silica compared to titanium coagulant. As seen in previous chapters, the titanium coagulant was seen to produce denser flocs, this can reduce the likelihood of flocs penetrating the membrane and causing blockage of the pores, allowing for better cake formation. This is reflected in the FRR of the membranes where pretreatment with titanium was able to achieve 94-95% with GO and CNT membranes whereas alum was able to achieve 90%. Cake layers formed by smaller particles is much more compact compared to that formed by larger ones, which imply that smaller particles have higher specific cake resistance (Chomiak et al., 2013; Lin et al., 2011).

Overall, the use of a coagulation pretreatment before membrane application showed improved solute rejection and flux recovery. It was also effective at removing residual aluminium and titanium that could remain in solution after coagulation.

Compared to ozone/membrane hybrid systems, the use of coagulation/membrane showed to improve the rejection of silica. However, that

is offset by reduced permeability. Both of these attributes can be credited to the cake layer formation on the membrane. The disadvantage of using coagulation/membrane would be the increased backwashes required to return the permeability of the membrane, however, that would be offset by the increased removal of silica.

6.4. Conclusions

This chapter presented the evaluation of various hybrid technologies for the removal of colloidal silica, with a focus on ozone, ion exchange, membrane and coagulation. A summary of the findings are as follows:

- Effectiveness of ozone treatment:
    - Ozone treatment on colloidal silica significantly altered the zeta potential of the particles. This change enhances the electrostatic interactions, which could then be applied and combined with subsequent technologies
    - Ozone effect on particle size of the colloidal silica was minimal, suggesting that ozone primarily affects the surface chemistry
- Ozone and ion exchange integration:
    - The integration of ozone-treated colloidal silica with ion exchange resins demonstrated improved silica uptake. The increased negative charge of the surface allowed for better electrostatic attraction between silica and ion exchange resin.
- Ozone and membrane filtration:
    - Ozone treated silica improved the rejection rates of colloidal silica of all membranes (PVDF, GO, and CNT). The enhanced zeta potential increased repulsion between silica particles and membrane surfaces, reducing fouling and improving filtration efficiency.
    - Flux recovery ratios were higher for membranes with ozonated colloidal silica compared to untreated samples, indicating reduced irreversible fouling.

- Coagulation and membrane filtration:
  - Pretreatment of coagulation with alum and titanium before membrane filtration proved effective in improving silica rejection and mitigating membrane fouling
  - Titanium coagulant that formed denser flocs, resulted in fewer smaller particles blocking the membrane pores, leading to improved membrane performance and higher flux ratio recoveries compared to alum.
  - Filtered coagulated samples demonstrated effectiveness of removing residual aluminium and titanium.

Overall, the use of hybrid technologies combining ozone treatment with ion exchange, and membrane filtration, along with coagulation pre-treatment, has shown substantial improvements in the removal efficiency of colloidal silica. These findings highlight the potential for employing these integrated approaches in water treatment and other applications requiring the efficient removal of colloidal particles.

6.5. References

Chandrakanth, M. S., & Amy, G. L. (1996). Effects of Ozone on the Colloidal Stability and Aggregation of Particles Coated with Natural Organic Matter. *Environmental Science & Technology*, *30*(2), 431-443. https://doi.org/10.1021/es9500567

Chheda, P., & Grasso, D. (1994). Surface Thermodynamics of Ozone-Induced Particle Destabilization. *Langmuir*, *10*(4), 1044-1053. https://doi.org/10.1021/la00016a016

Chomiak, A., Mimoso, J., Koetzsch, S., Sinnet, B., Pronk, W., Derlon, N., & Morgenroth, E. (2013). Biofilm formation and permeate quality improvement in Gravity Driven Membrane ultrafiltration. *Water Supply*, *14*(2), 274-282. https://doi.org/10.2166/ws.2013.197

Cruz-Alcalde, A., Esplugas, S., & Sans, C. (2020). Continuous versus single H2O2 addition in peroxone process: Performance improvement and modelling in wastewater effluents. *Journal of Hazardous Materials*, *387*, 121993. https://doi.org/https://doi.org/10.1016/j.jhazmat.2019.121993

Dabasinskaite, L., Krugly, E., Baniukaitiene, O., Martuzevicius, D., Ciuzas, D., Jankauskaite, L., Aukstikalne, L., & Usas, A. (2021). The Effect of Ozone Treatment on the Physicochemical Properties and Biocompatibility of Electrospun Poly(ε)caprolactone Scaffolds. *Pharmaceutics*, *13*(8).

Duval, Y., Mielczarski, J. A., Pokrovsky, O. S., Mielczarski, E., & Ehrhardt, J. J. (2002). Evidence of the Existence of Three Types of Species at the Quartz–Aqueous Solution Interface at pH 0–10: XPS Surface Group Quantification and Surface Complexation Modeling. *The Journal of Physical Chemistry B*, *106*(11), 2937-2945. https://doi.org/10.1021/jp012818s

Egitto, F. D., & Matienzo, L. J. (2006). Transformation of Poly(dimethylsiloxane) into thin surface films of SiOx by UV/Ozone treatment. Part I: Factors affecting modification. *Journal of Materials Science*, *41*(19), 6362-6373. https://doi.org/10.1007/s10853-006-0712-5

Freese, S. D., Nozaic, D., Pryor, M. J., Trollip, D. L., & Smith, R. A. (1999). Comparison of ozone and hydrogen peroxide/ozone for the treatment of

eutrophic water. *Water Science and Technology, 39*(10-11), 325-328. https://doi.org/10.2166/wst.1999.0675

Iler, R. K. Chemistry of Silica - Solubility, Polymerization, Colloid and Surface Properties and Biochemistry. In: John Wiley & Sons.

Johanes Wibowo, F. S., David Blackford. (1997). Measuring and removing dissolved and colloidal silica in ultrapure water. In *Ultrapure Fluids*.

Kang, M. J., Jin, F. L., & Park, S. J. Influence of Ozone-Treated Silica Nanoparticles on Mechanical Interfacial Behavior and Thermal Stability of Silicone Composites. (1533-4880 (Print)).

Lai, J., Huangfu, Z., Xiao, J., Wang, Z., Liu, Y., Li, C., Li, F., Jia, Y., Wang, Q., Qi, F., Ikhlaq, A., Kumirska, J., Siedlecka, E., & Ismailova, O. (2024). Synergistic effect by supported activated carbon between functional groups and metal oxygen vacancies: Enhancing Ibuprofen degradation by improving ozone mass transfer [10.1039/D4EW00244J]. *Environmental Science: Water Research & Technology*. https://doi.org/10.1039/D4EW00244J

Lin, H. J., Gao, W. J., Leung, K. T., & Liao, B. Q. (2011). Characteristics of different fractions of microbial flocs and their role in membrane fouling. *Water Science and Technology, 63*(2), 262-269. https://doi.org/10.2166/wst.2011.047

Merényi, G., Lind, J., Naumov, S., & Sonntag, C. v. (2010). Reaction of Ozone with Hydrogen Peroxide (Peroxone Process): A Revision of Current Mechanistic Concepts Based on Thermokinetic and Quantum-Chemical Considerations. *Environmental Science & Technology, 44*(9), 3505-3507. https://doi.org/10.1021/es100277d

Meshref, M. N. A., Klamerth, N., Islam, M. S., McPhedran, K. N., & Gamal El-Din, M. (2017). Understanding the similarities and differences between ozone and peroxone in the degradation of naphthenic acids: Comparative performance for potential treatment. *Chemosphere, 180*, 149-159. https://doi.org/https://doi.org/10.1016/j.chemosphere.2017.03.113

Osbeck, S., Bradley, P. R., Liu, C., & Ward, S. (2011). Effect of an ultraviolet/ozone treatment on the surface texture and functional groups on

polyacrylonitrile carbon fibres. *Carbon, 49,* 4322-4330. https://doi.org/10.1016/j.carbon.2011.06.005

Parks, G. A. (1965). The Isoelectric Points of Solid Oxides, Solid Hydroxides, and Aqueous Hydroxo Complex Systems. *Chemical Reviews, 65*(2), 177-198. https://doi.org/10.1021/cr60234a002

Reungoat, J., Pic, J. S., Manéro, M. H., & Debellefontaine, H. (2007). Adsorption of Nitrobenzene from Water onto High Silica Zeolites and Regeneration by Ozone. *Separation Science and Technology, 42*(7), 1447-1463. https://doi.org/10.1080/01496390701289948

Schlichter, B., Mavrov, V., & Chmiel, H. (2003). Study of a hybrid process combining ozonation and membrane filtration — filtration of model solutions. *Desalination, 156*(1), 257-265. https://doi.org/https://doi.org/10.1016/S0011-9164(03)00348-5

Schwarz, J. A., Driscoll, C. T., & Bhanot, A. K. (1984). The zero point of charge of silica—alumina oxide suspensions. *Journal of Colloid and Interface Science, 97*(1), 55-61. https://doi.org/https://doi.org/10.1016/0021-9797(84)90274-1

Spialter, L., Pazdernik, L., Bernstein, S., Swansiger, W. A., Buell, G. R., & Freeburger, M. E. (1971). Mechanism of the reaction of ozone with the silicon-hydrogen bond. *Journal of the American Chemical Society, 93*(22), 5682-5686. https://doi.org/10.1021/ja00751a018

Tizaoui, C., Bouselmi, L., Mansouri, L., & Ghrabi, A. (2007). Landfill leachate treatment with ozone and ozone/hydrogen peroxide systems. *Journal of Hazardous Materials, 140*(1), 316-324. https://doi.org/https://doi.org/10.1016/j.jhazmat.2006.09.023

Wada, H., Yanaga, K., Kuroda, Y., Hanela, S., & Hirayama, Y. (2005). Recycling of Wastewater Containing Iron-Complex Cyanides Using UV Photodecomposition and UV Ozone Oxidation in Combination with an Ion-Exchange Resin Method. *Bulletin of the Chemical Society of Japan, 78*(3), 512-518. https://doi.org/10.1246/bcsj.78.512

Wang, C., Wang, Y., Tian, Y., Wang, C., & Suga, T. (2017). Room-temperature direct bonding of silicon and quartz glass wafers. *Applied Physics Letters*, *110*(22), 221602. https://doi.org/10.1063/1.4985130

Wang, H., Zhan, J., Yao, W., Wang, B., Deng, S., Huang, J., Yu, G., & Wang, Y. (2018). Comparison of pharmaceutical abatement in various water matrices by conventional ozonation, peroxone (O3/H2O2), and an electro-peroxone process. *Water Research*, *130*, 127-138. https://doi.org/https://doi.org/10.1016/j.watres.2017.11.054

Wu, T., & Englehardt, J. D. (2015). Peroxone mineralization of chemical oxygen demand for direct potable water reuse: Kinetics and process control. *Water Research, 73*, 362-372.

Xu, J., Wang, C., Wang, T., Wang, Y., Kang, Q., Liu, Y., & Tian, Y. (2018). Mechanisms for low-temperature direct bonding of Si/Si and quartz/quartz via VUV/O3 activation [10.1039/C7RA13095C]. *RSC advances, 8*(21), 11528-11535. https://doi.org/10.1039/C7RA13095C

Xu, X., & Goddard, W. A., 3rd. Peroxone chemistry: formation of H2O3 and ring-(HO2)(HO3) from O3/H2O2. (0027-8424 (Print)).

Yu, C., Gao, B., Shen, X., Bu, F., Jin, B., & Yue, Q. (2021). Impacts of composite flocculant in coagulation/ultrafiltration hybrid process for treatment of humic acid water: the role of basicity. *Environmental Technology, 42*(18), 2856-2869. https://doi.org/10.1080/09593330.2020.1716856

Zaera, F. (2012). Probing Liquid/Solid Interfaces at the Molecular Level. *Chemical Reviews, 112*(5), 2920-2986. https://doi.org/10.1021/cr2002068

7. Conclusions and recommendations for future work

This thesis aimed to address the persistent challenge of silica removal from boiler feedwater systems at Tata Steel, Port Talbot. Both the presence of colloidal and soluble silica has been identified as a significant contaminant leading to scaling, fouling and corrosion, which adversely affect the efficiency and longevity of critical equipment including boilers and steam turbines. The research explored a range of treatment technologies to improve silica removal, focusing on optimisation of coagulants, advanced membrane enhancements, ion exchange and hybrid approaches integrating multiple techniques. The key findings are as follows:

Optimisation of coagulant

- o The study investigated various coagulants, including conventional options such as alum and ferric, alongside novel alternatives such as titanium and zirconium based coagulants.
- o Titanium and alum proved highly effective in removing colloidal silica, both achieving removal efficiencies exceeding 90%. At optimal dosages of 2.7 mg Al/L for alum and 4.4 mg Ti/L for titanium, significant differences in performance characteristics were observed. Titanium produced larger and denser flocs compared to alum and demonstrated a broader effective dosage range. However, alum exhibited superior performance within a pH range of 6-8, while titanium showed optimal silica removal in a slightly more acidic environment, with a pH range of 4-6.
- o Testing on River Afan water reaffirmed that alum and titanium were the most effective coagulants, with titanium demonstrating superior performance by achieving total organic carbon (TOC) removal rates exceeding 80%.

Advanced membrane technology:

- PVDF membrane matrices enhanced with graphene oxide and carbon nanotubes showed increased porosity, hydrophilicity and a more negative surface zeta potential.

- Performance testing revealed enhanced pure water permeability, with increases of 141% for GO and 171% for CNTs, respectively. Rejection of colloidal silica and BSA was conformed to the following the order, GO>CNT>PVDF.

- Testing of River Afan demonstrated the effectiveness of the modified membranes in removing colloidal silica. The enhanced membranes showed improved permeability, colloidal silica rejection, and flux recovery ratio (FRR). Notably, the rejection of total silica increased by 10.7% with graphene oxide (GO) modification and 6.5% with carbon nanotube (CNT) modification. Despite these improvements, the residual total silica levels remained relatively high, indicating that ultrafiltration (UF) membranes alone are only effective primarily for colloidal silica removal.

Iron impregnated ion exchange resin:

o A comparison of FerrIX A33E resin in its chloride (Cl^-) and hydroxide (OH^-) forms revealed distinct differences in their silica removal performance. The hydroxide form showed significantly faster kinetics and higher adsorption efficiency, attributed primarily to enhanced diffusion properties.

o The Redlich-Peterson and Freundlich isotherm models provided the best fit for understanding the heterogeneous nature of the resin. Models like Bohart-Adams, Thomas, and Clark effectively predicted breakthrough curves in column studies. However, modified approaches, including the n-order Bohart-Adams and

fractal models, demonstrated superior accuracy, particularly in capturing the asymmetric adsorption behaviour observed with the hydroxide form of FerrIX resin.

- o Multicomponent isotherm analysis revealed a significant decline in silica uptake in the presence of competing ions like nitrate and phosphate. However, the FerrIX A33E resin demonstrated strong selectivity for phosphate removal, indicating that pre-selective removal of phosphate could enhance silica adsorption efficiency in a multicomponent downstream ion exchange system.

Hybrid water treatment technologies:

- 30 minutes of ozone treatment (ozone gas concentration at approximately 70 g/m^3 at normal temperature and pressure (NTP: 0°C and 1atm)) on colloidal silica significantly altered the zeta potential of the particles, reducing zeta potential from -15 to -26 mV.

- The integration of ozone-treated colloidal silica with ion exchange resins demonstrated improved silica uptake. The increased negative charge of the surface allowed for better electrostatic attraction between silica and ion exchange resin.

- Ozone-treated silica significantly improved colloidal silica rejection across all membrane types (PVDF, GO, and CNT). The enhanced zeta potential increased the electrostatic repulsion between silica particles and the membrane surfaces, effectively reducing fouling and boosting overall filtration efficiency.

- Pre-treating with alum and titanium coagulants prior to membrane filtration effectively enhanced silica rejection and significantly reduced membrane fouling.
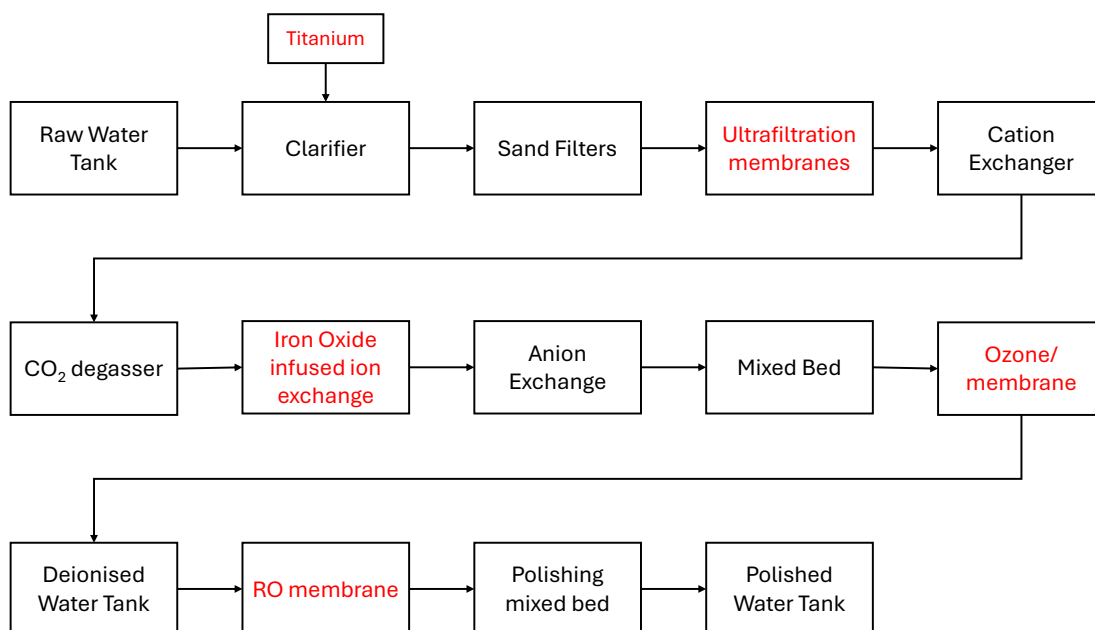
Figure 7.1. New technologies potential implementation BFD

Figure 7.1 shows the potential location of the new technologies that could be placed in the existing plant.

7.1. Recommendations and future work

Building on the findings of this thesis, several avenues for further research have been identified:

- Pilot testing of titanium coagulant and its viability.
- Pilot testing for silica removal in hybrid systems: To validate the long-term performance of hybrid treatment systems, a large-scale pilot plant that combines coagulation and advanced oxidation/membrane technologies is recommended. Operating this system over an extended period at varying water sources would allow for a better understanding of the interactions between silica, coagulants, and the modified membranes. Such testing would also help determine the optimal operating conditions for silica removal and the impact of varying pH and organic content on overall efficiency.
- Evaluation of the membrane modification scalability: The enhanced permeance permeability and fouling resistance achieved with GO- and CNT-modified PVDF membranes should be tested on a larger scale. A comprehensive pilot study can assess whether these nanomaterial

176

modifications retain their performance benefits in a real-world setting, particularly under varying colloidal silica concentrations. The study should also examine long-term fouling behaviour and the maintenance requirements for these modified membranes.

- Exploration of Multi-Component Adsorption Dynamics in Modified Resins: The reduced silica uptake observed in the presence of competing ions, such as phosphate and nitrate, highlights the need for detailed multi-component isotherm studies. By exploring different concentrations of these ions, the selectivity and binding mechanisms of modified resins can be better understood. This would help optimize resin formulations and operational strategies to enhance silica capture in complex water matrices.

These further investigations would build upon the foundational results of this study, contributing to the development of more efficient, scalable, and resilient water treatment technologies tailored to complex industrial requirements.

A. Appendices – Calibration curves
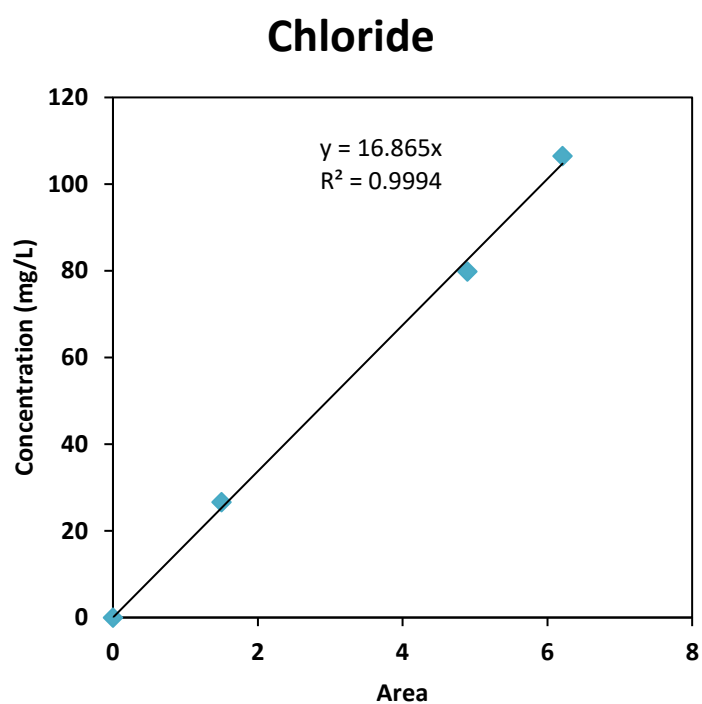
Chloride

Figure A.1. High performance ion chromatography calibration for chloride
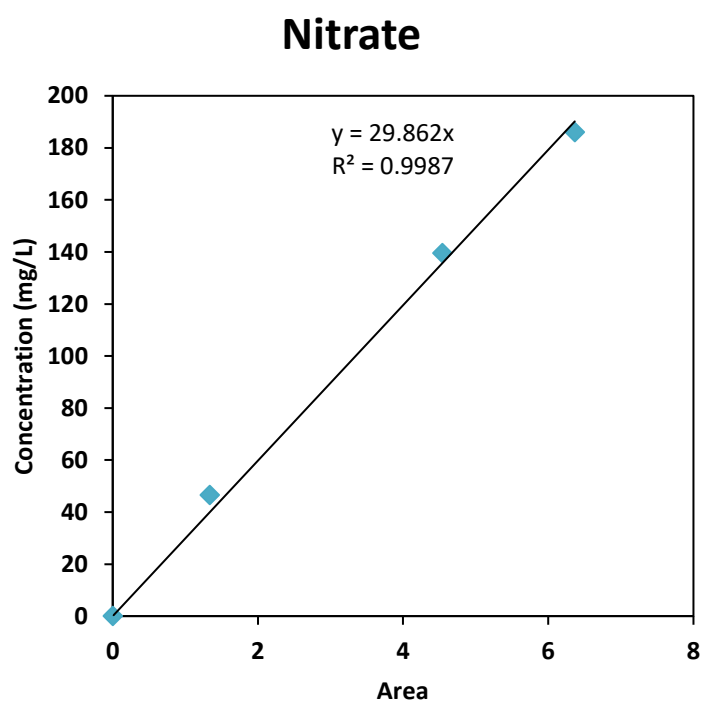
Nitrate

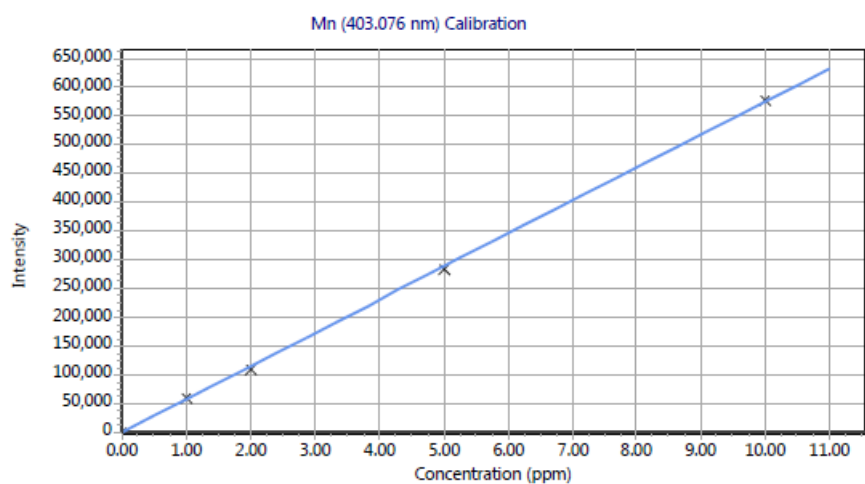*Figure A.2. High performance ion chromatography calibration for nitrate*

Sulfate

y = 24.589x
R² = 0.9995
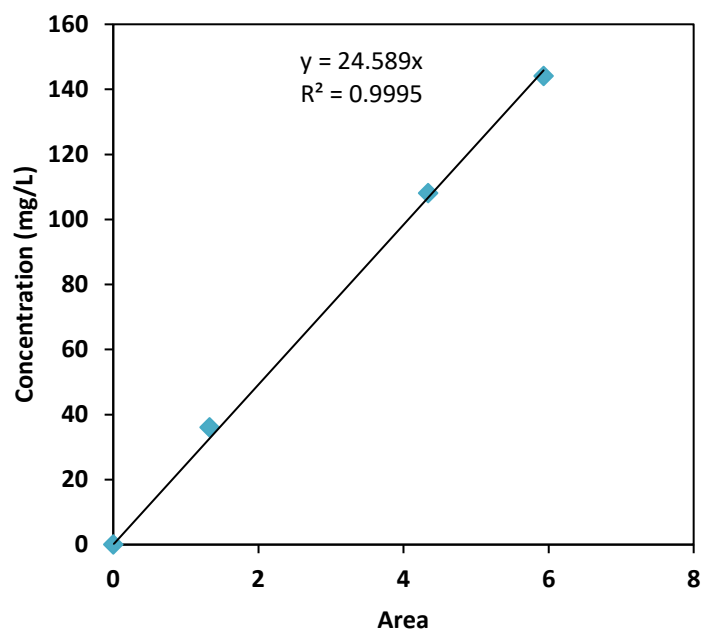
Figure A.3. High performance ion chromatography calibration for sulphate

Phosphate

y = 71.879x
R² = 0.9982
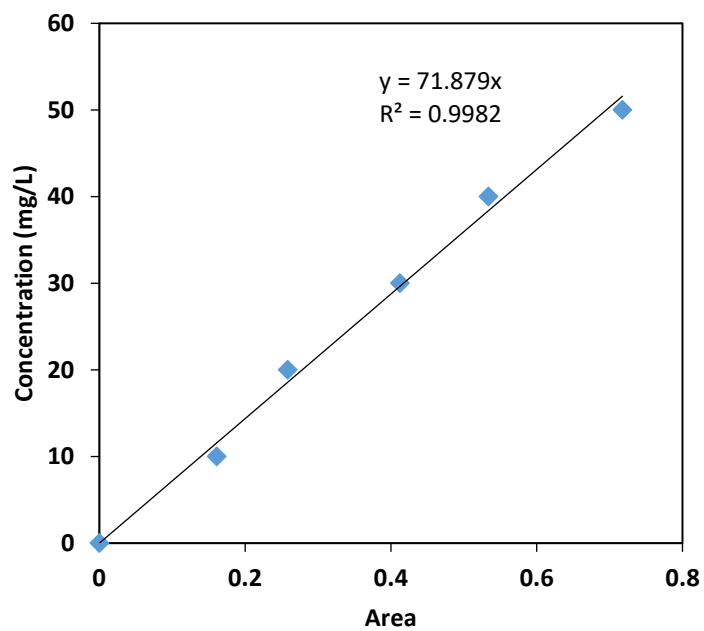
Figure A.4. High performance ion chromatography calibration for phosphate

Figure A.5. MP-AES calibration curve for manganese
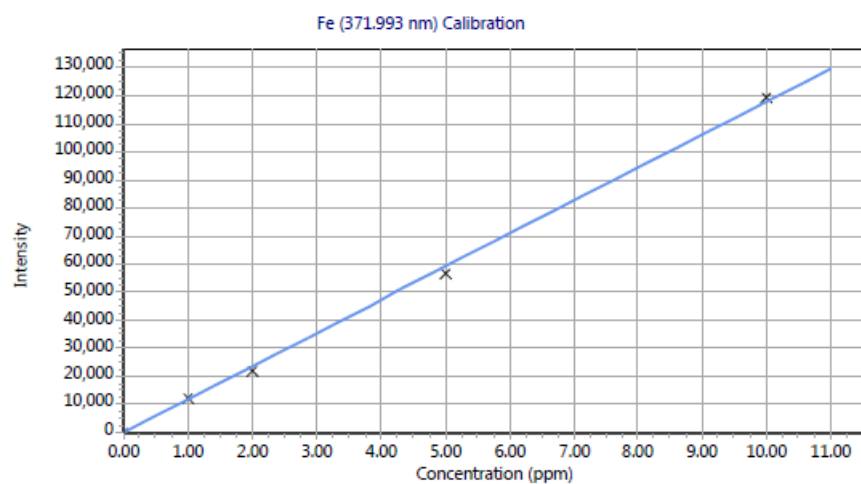
Figure A.4. MP-AES calibration curve for iron
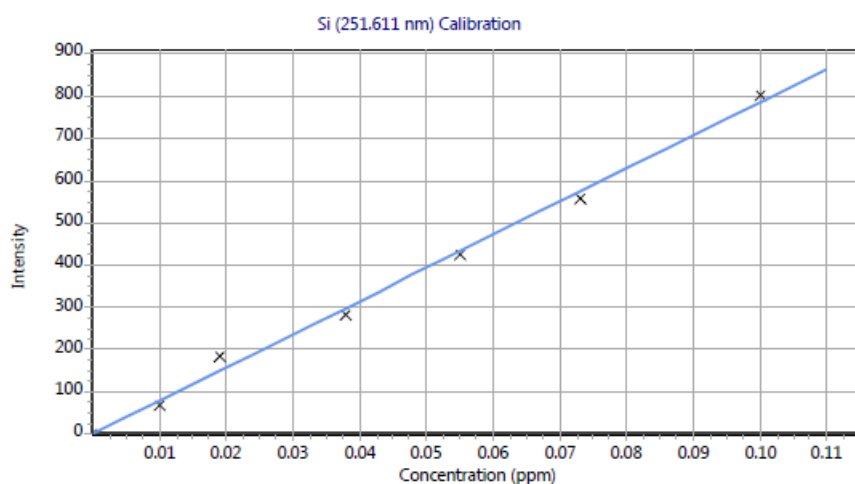
Figure A.3. MP-AES calibration curve for silica
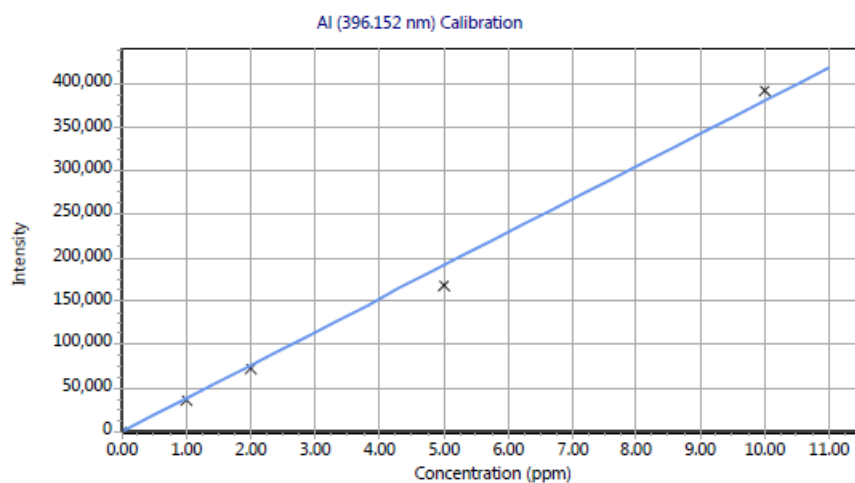
Figure A.6. MP-AES calibration curve for aluminium

B. Appendices – FerrIX resin
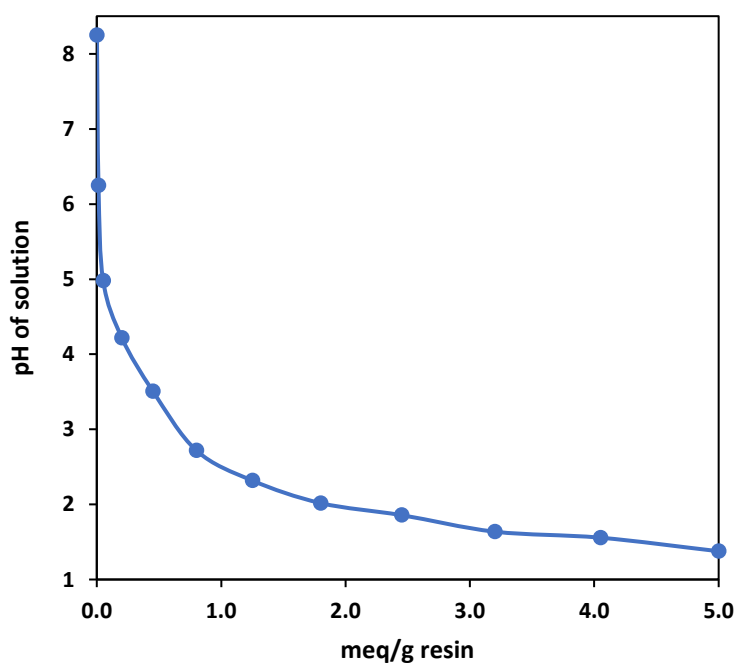
Figure B.1 pH titration curve for FerrIX A33E resin

Table B.1. FerrIX A33E bulk density

Vol (mL)	Mass total (g)	Mass of resin (g)	Density (g/cm3)
10	82.26	7.54	0.75
20	89.01	14.29	0.71
30	96.58	21.86	0.73
40	104.2	29.48	0.74
50	111.9	37.18	0.74
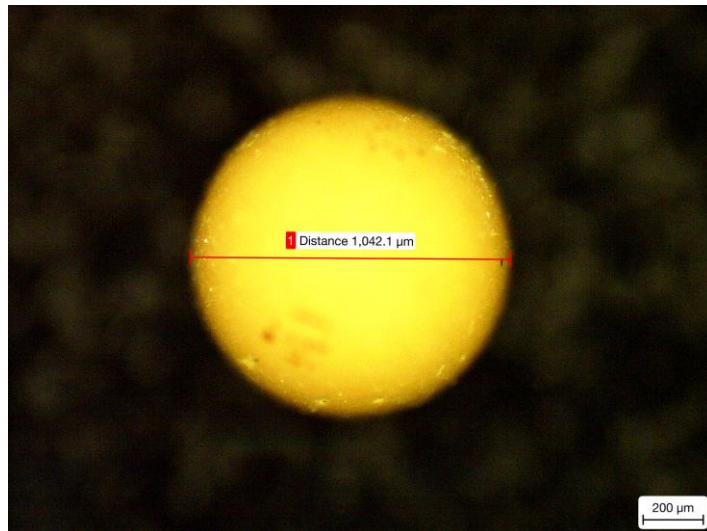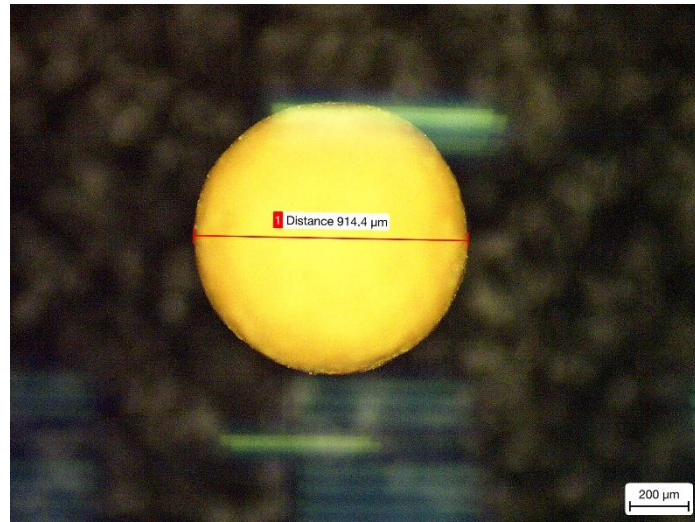
Figure B.2. Microscopic images of FerrIX A33E
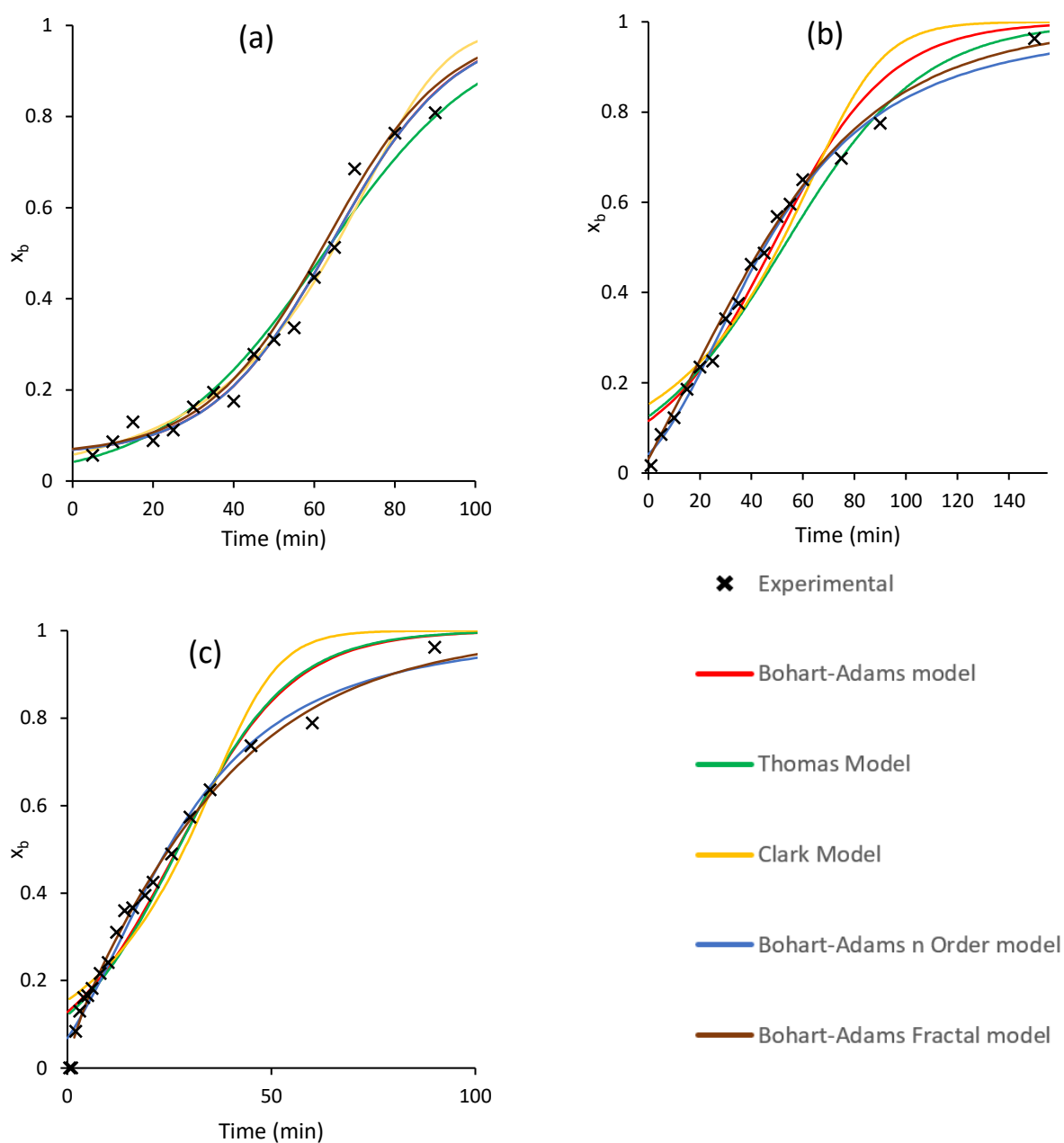
a. Phosphate breakthrough curves

Figure B.3 Breakthrough curves for varying flow rates (a) 30 mL/min (b) 60 mL/min and (c) 90 mL/min (bed height = 5cm, Cinlet = 33.3 mg P/L)
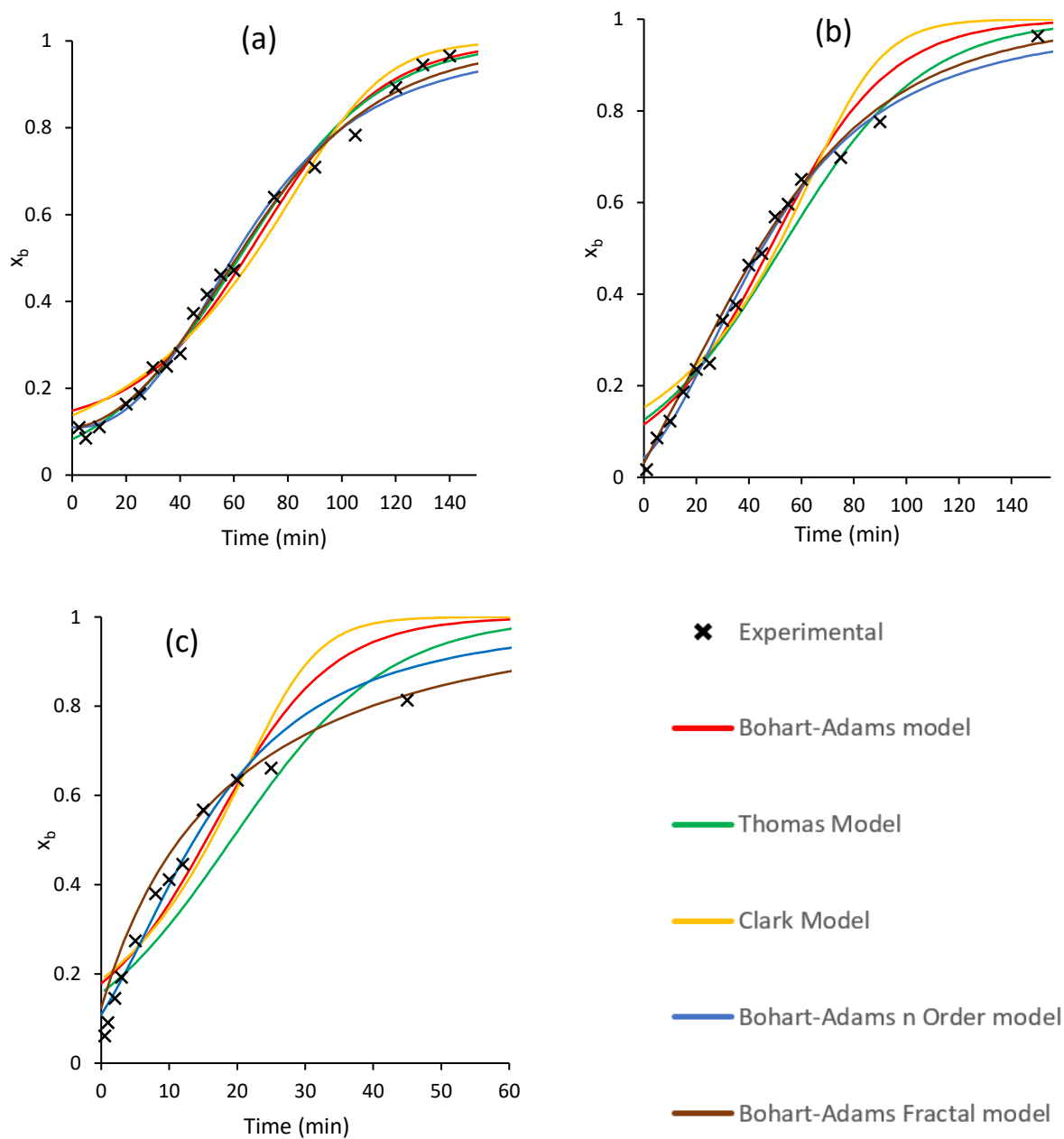
Figure B.4 Breakthrough curves at different inlet concentrations (5cm bed depth and 60 mL/min) (a) 16.7 mg P/L (b) 33.3 mg P/L and (c) 66.7 mg P/L
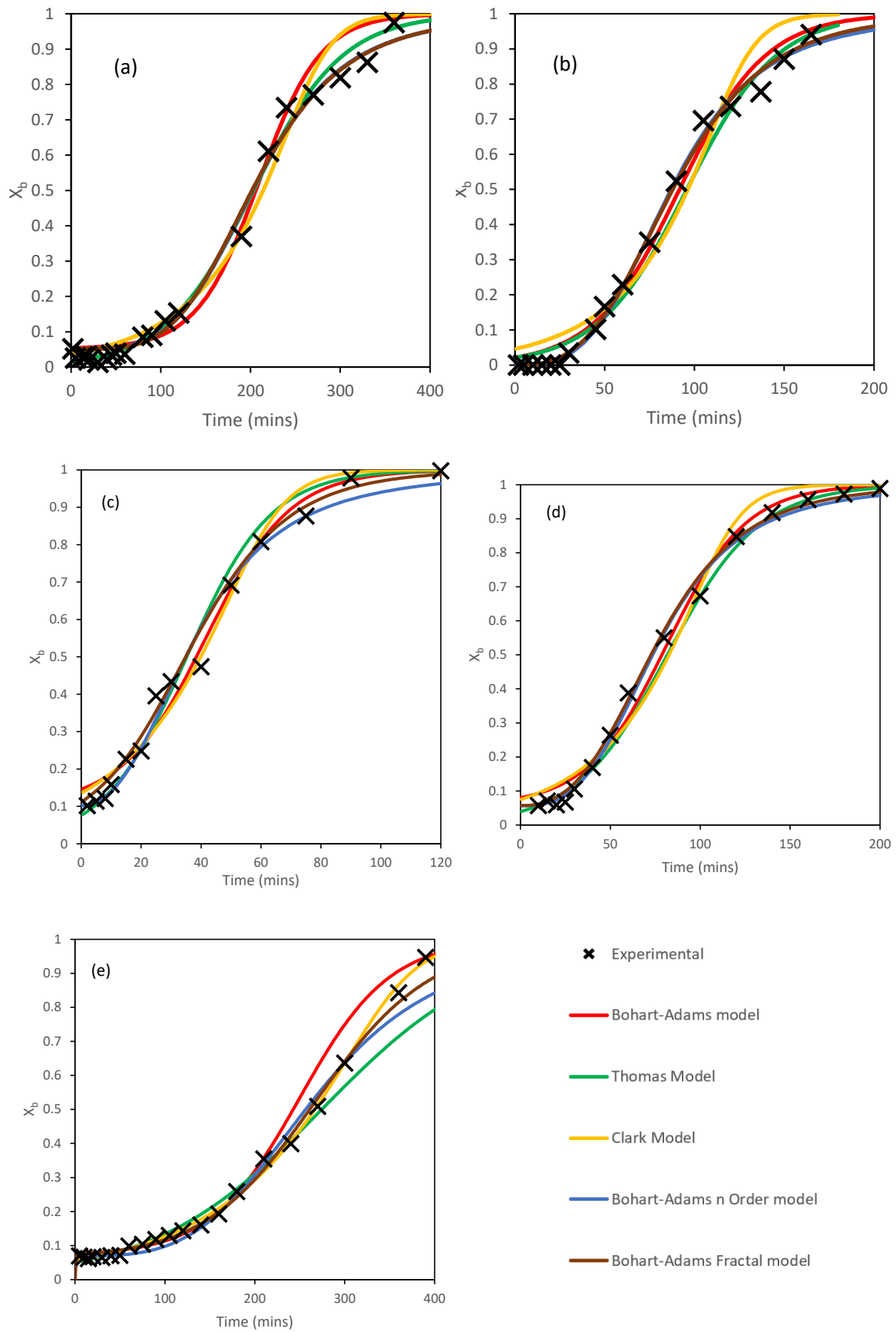
Figure B.5 Breakthrough curves at 10 cm bed hight and: (a) 30 mL/min, 33.3 mg/L (b) 60 mL/min, 33.3 mg/L (c) 120 mL/min, 33.3 mg/L, (d) 60 mL/min, 16.7 mg/L and (e) 60 mL/min, 66.7 mg/L
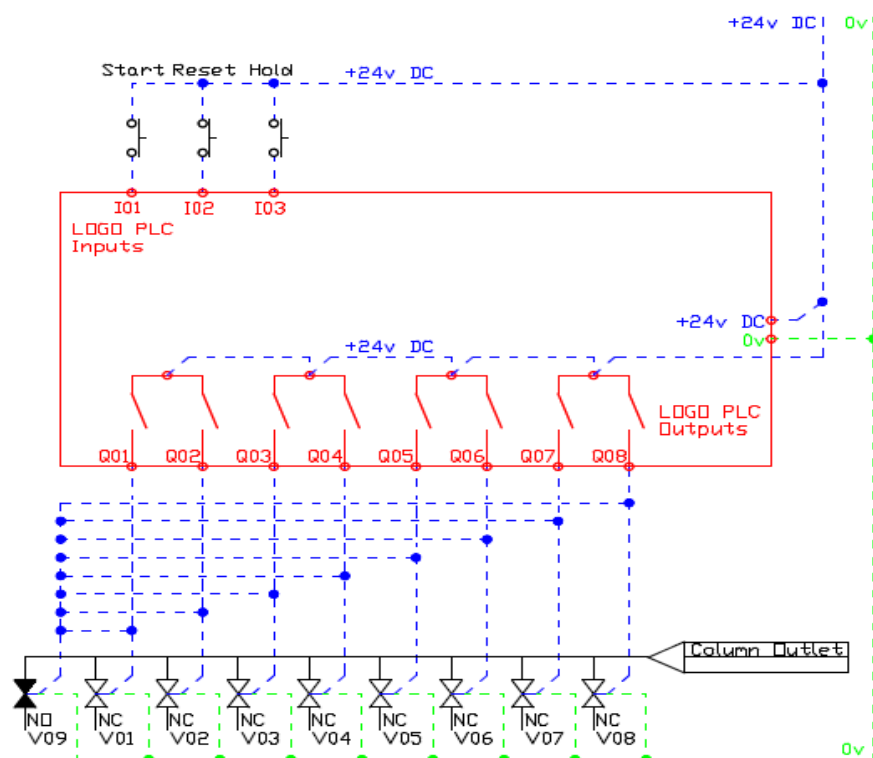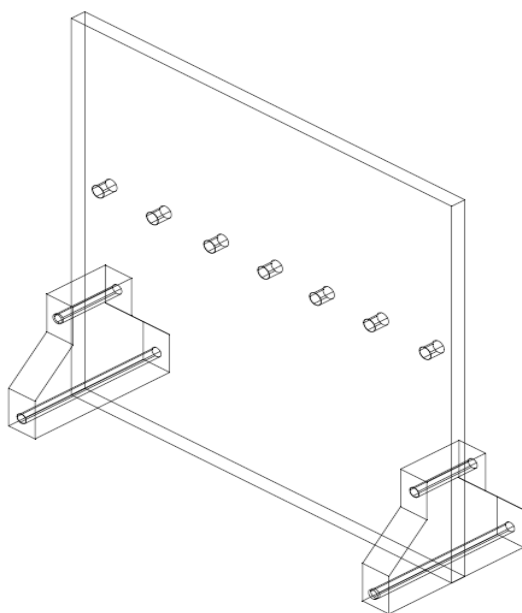
Figure B.6. Ion exchange auto sampling rig (a) frame (b) set up (c) PLC logic
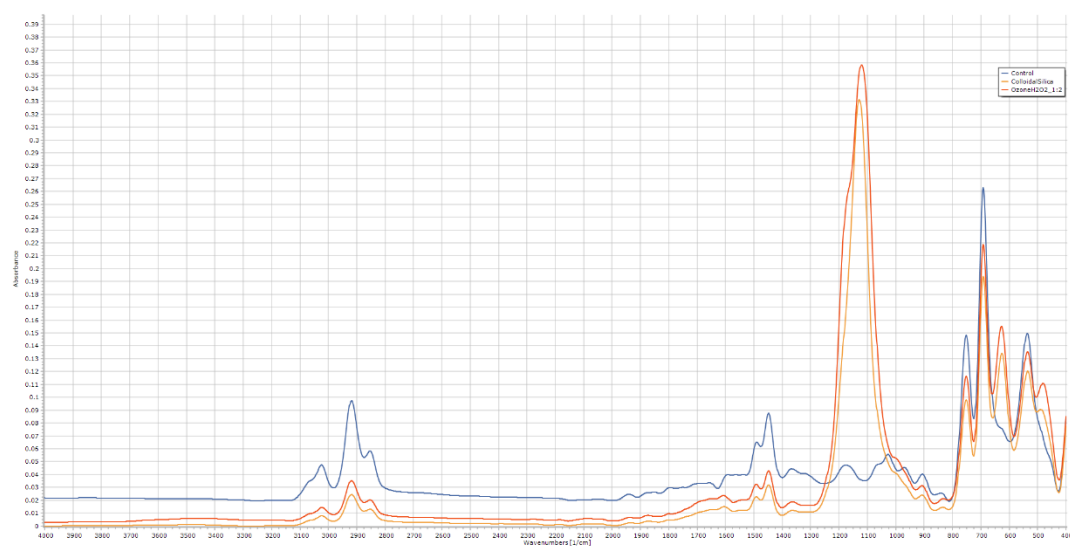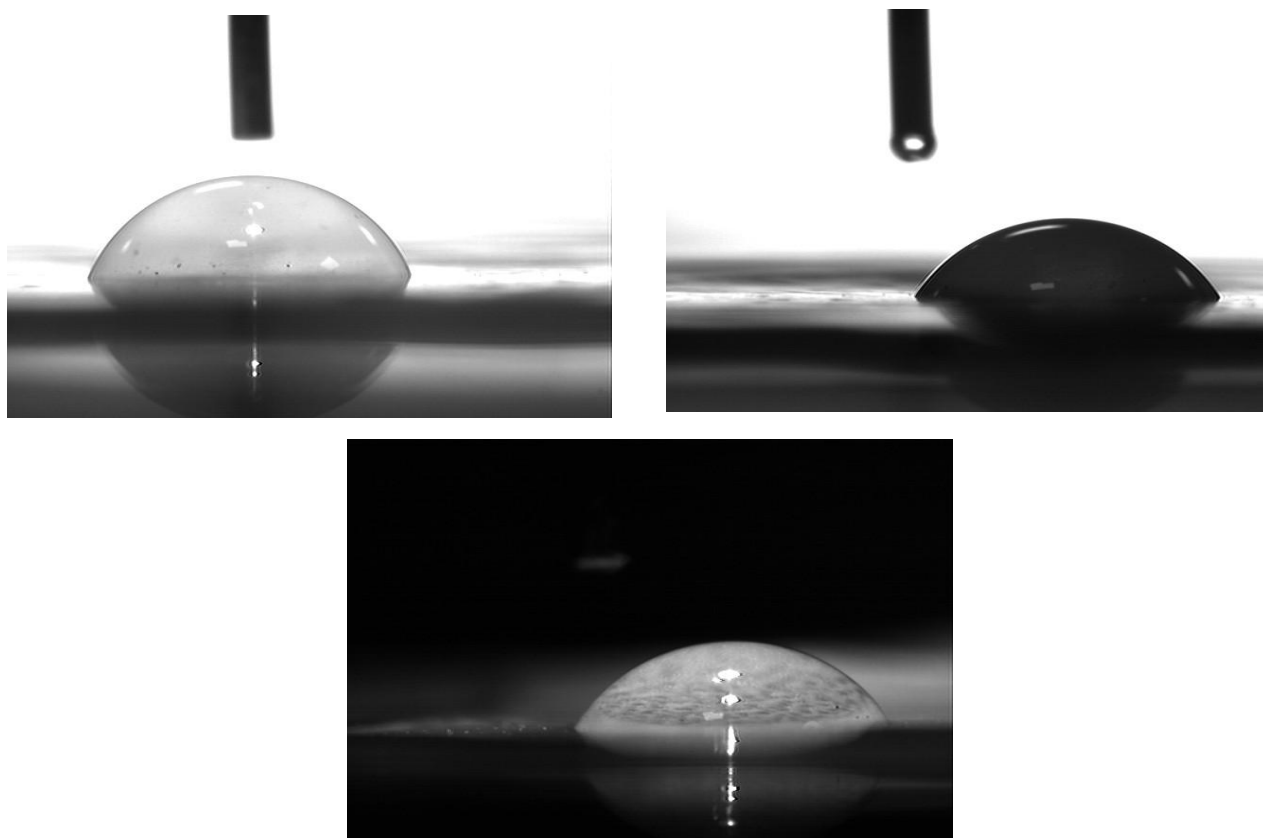
Figure B.7. Ozonated colloidal silica FTIR

Figure B.8. Membrane contact angle images

C. Appendices C

Table C.1. Tata steel Port Talbot Margam C water treatment plant sample results from 29/10/2020

29/01/2020								
	Feed water	Feed water (0.45 micron filter)	Sandfilter (unit 2)	Cation (unit 2)	Cation (unit 3)	Anion (unit 3)	Mixed bed (unit 3)	Polisher (unit 3)
SiO2 (ppm)	5.16	4.85	5.03	4.9	4.79	0.03	0.000	0.000
Fe (ppm)	0.14	-	0.1	0.03	0.02	0.004	0	0
Mn (ppm)	0.02	-	0.01	0.0009	0.0002	0	0	0
Al (ppm)	0.58	-	0.51	0.07	0.02	0.000	0.0000	0

Table C.2. HACH 8282 method for measuring soluble silica results from mixed bed and RO permeate

RO permeate and MB samples - Hach 8282 method		
Sample	Date	Dissolved SiO2 (µg/L)
Sample 2 - mRO2 permeate	28/10/2022	5
Sample 3 - mRO1 permeate	07/11/2022	3
Sample 2 - mRO1 permeate	09/11/2022	4
Sample 3 - mRO3 permeate	28/10/2022	4
Sample 2 - mRO3 permeate	07/11/2022	14
Sample 3 - mRO3 permeate	09/11/2022	5
Sample 1 - Common inlet to mROs from MB	28/10/2022	16
Sample 1 - Common inlet to mROs from MB	07/11/2022	20
Sample 1 - Common inlet to mROs from MB	09/11/2022	12
Sample 2 - Permeate from RO1	17/11/2022	11
Sample 2 - Permeate from RO1	22/11/2022	11
Sample 2 - Permeate from RO1	08/12/2022	8
Sample 3 - Permeate from RO3	17/11/2022	9
Sample 3 - Permeate from RO3	22/11/2022	7
Sample 3 - Permeate from RO3	08/12/2022	4
Sample 1 - Common inlet to ROs from MB	17/11/2022	13
Sample 1 - Common inlet to ROs from MB	22/11/2022	24
Sample 1 - Common inlet to ROs from MB	08/12/2022	38

Table C.3. MP-AES results for silica from Margam C RO concentrate samples

RO cocentrate samples - MP-AES			
Sample	Date	SiO2 (mg/L)	SiO2 (µg/L)
mRO2 concentrate	28/10/2022	0.03	30
mRO1 concentrate	07/11/2022	0.11	110
mRO1 concentrate	09/11/2022	0.18	180
mRO3 concentrate	28/10/2022	0.04	40
mRO3 concentrate	07/11/2022	0.11	110
mRO3 concentrate	09/11/2022	0.18	180
mRO1 concentrate	17/11/2022	0.02	20
mRO1 concentrate	22/11/2022	0.19	190
mRO1 concentrate	08/12/2022	0.25	250
mRO1 concentrate	17/11/2022	0.02	20
mRO1 concentrate	22/11/2022	0.22	220
mRO1 concentrate	08/12/2022	0.26	260